A Computational Fluid Dynamics based model that predicts wall shear stress in CANDU outlet feeder pipes

By

Uditha Wijayaratne

A Thesis Submitted in Partial Fulfillment of the Requirements for the

Degree of Master of Applied Science in Nuclear Engineering

in

The Faculty of Energy Systems and Nuclear Science

Nuclear Engineering

University of Ontario Institute of Technology

January 2018

ABSTRACT

Wall thinning of carbon steel in CANDU reactor outlet feeder pipes due to Flow Accelerated Corrosion (FAC) is identified as one of the challenges for CANDU reactors since it would force them to shut down due to safety reasons. Several models have been developed over time to predict the corrosion rate (i.e. the rate of wall thinning) of CANDU outlet feeders. These models are developed based on the corrosion chemistry and the mass transfer theories on growth and removal of the protective magnetite layer on the outlet feeder pipe surface. The magnetite layer is acting as a protective layer for the carbon steel feeder pipes by avoiding further corrosion. However, due to the wall shear stress that exerts on the feeder pipe wall, this protective layer is flushed away with the primary heat transport fluid.

Wall shear stress is identified as one of the crucial factors behind FAC. Other parameters such as Fe ion concentration, fluid temperature, and pressure would remain within a certain range for a typical CANDU reactor. Still, the distribution of wall shear stress highly depends on the physical arrangement of the outlet feeder pipes. Therefore, wall shear stress would change drastically from one feeder pipe to another resulting in a higher degree of impact on the rate of wall thinning due to FAC.

The model developed in this study predicts the maximum wall shear stress on the first bend of a particular feeder pipe considering the fluid Reynolds number, the bend angle and the linear length from the grayloc hub to the first bend. The model is developed using the wall shear stress distribution results generated by Computational Fluid Dynamics (CFD) studies using Siemens NX. The wall shear stress results from the model is then compared against the rate of wall thinning data available for the reactor 01 of the Darlington Nuclear Generating Station as well as some other models available in the literature.

The model shows a good trend of predicted wall shear stress values against the rate of wall thinning data available. At this stage, the model can be used to identify the feeder pipe with the highest rate of wall thinning due to FAC among a set of given feeder pipes with 2” or 2.5” nominal diameters. This model can be used to identify the optimum feeder pipes for wall thickness measurements during routine maintenance and hence replace the required feeder pipes to avoid any unplanned shut down due to safety reasons.

ACKNOWLEDGEMENT

Firstly, I would like to convey my gratitude to my thesis supervisor, Dr. George Bereznai and supervisory committee member Dr. Markus Piro. Their input and knowledge made a tremendous success in my research. I learned a lot from their experience and grateful to them for the opportunity they provided to me.

I am always grateful to Mr. Sharman Perera for sharing his knowledge and experience in Computational Fluid Dynamics. His dedication and guidance throughout the research are highly appreciated.

Dr. Ming Li and Dr. Paul Fabian from the Major Component Engineering Department, Ontario Power Generation were more than helpful in providing required engineering drawings, design and operational details of unit 1 at Darlington Nuclear Generating Station.

I am also thankful to Dr. Mahesh Pandey, Professor – Department of Civil and Environmental Engineering, University of Waterloo, for sharing his valuable experience and guidance.

The kindness and the help from the staff and students of the Faculty of Energy Systems and Nuclear Science have made my experience at the University of Ontario Institute of Technology so pleasant.

I would like to take this opportunity to convey my gratitude to my wife and parents for their unconditional love and support throughout the years moving me in a forward direction. I feel extremely grateful for all the support and great encouragement from my aunty and cousins throughout the years.

TABLE OF CONTENTS

LIST OF TABLES

LIST OF FIGURES

NOMENCLATURE

FAC	Flow Accelerated Corrosion
CFD	Computational Fluid Dynamics
PHWR	Pressurized Heavy Water Reactors
PHT	Primary Hear Transport
LWR	Light Water Reactors
HWR	Heavy Water Reactors
NPPs	Nuclear Power Plants
ABTR	Advanced Burner Test Reactor
SST	Shear Stress Transport
RANS	Reynolds Averaged Navier–Stokes
LOCA	Loss of Coolant Accident
DNS	Direct Numerical Simulation
LES	Large Eddy Simulation
RMS	Root Mean Square
ASME	American Society of Mechanical Engineers
GCI	Grid Conversion Index
$\dot{m}$	Rate of mass loss at wall (mol/s),
k_m	Mass transfer coefficient (m/s),
k_d	Magnetite dissolution kinetic constant (m^2/s),
C_{sat}	Iron saturation concentration (mol/m^3),
C_b	Iron concentration in bulk coolant (mol/m^3).
u_*	Friction velocity at the nearest wall (m/s)
y	Distance to the nearest wall (m)
υ	Local kinematic viscosity of the fluid (m^2/s)
El	Entrance length number
l_e	Length to fully developed velocity profile (mm)
d	Pipe diameter (mm)
ρ	Fluid density (kg/m^3)

U	Fluid velocity (m/s)
μ	Dynamic viscosity of the fluid (Pa.s)
τ_{Max}	Maximum wall shear stress (kPa)

1 INTRODUCTION

The majority of nuclear power reactors operating worldwide in 2016 are more than 25 years old and it has become challenging to continue their operations due to the effect of 'Ageing' [1] [2]. Ageing related to nuclear power plants can be expressed as the continuous degradation of material with time, resulting in reduced performance and/or safety margins of the power plant. Dedicated researchers across the world are now working on developing models that are capable of predicting various ageing effects in nuclear power reactors.

CANada Deuterium Uranium reactors, in short form CANDU reactors, belong to the category of Pressurized Heavy Water Reactors (PHWR) that use heavy water at elevated pressure (~10 MPa) as the reactor coolant [3]. The Primary Hear Transport (PHT) system of a CANDU reactor serves as the main heat sink for the reactor consists of pressure tubes, reactor coolant, steam generators, heat transport pumps, reactor inlet headers and reactor outlet headers (Figure 1) [4].

Unlike most other nuclear reactors, CANDU reactors are capable of online refueling through the fueling machines. Therefore, CANDU has a specific reactor core design where the fuel bundles rest inside the pressure tube, which is then covered by a calandria tube. The CANDU 6 reactor core contains 380 such fuel channels with 12 fuel bundles in each while the Darlington reactors contain 480 such fuel channels [5] [6]. The heavy water coolant that is flowing through the pressure tubes is used to remove heat liberated due to the fission chain reactions inside the fuel bundles. Therefore, the proper functionality of the PHT system, as well as the effective utilization of heavy water coolant, is important in CANDU reactors in order to operate safely.

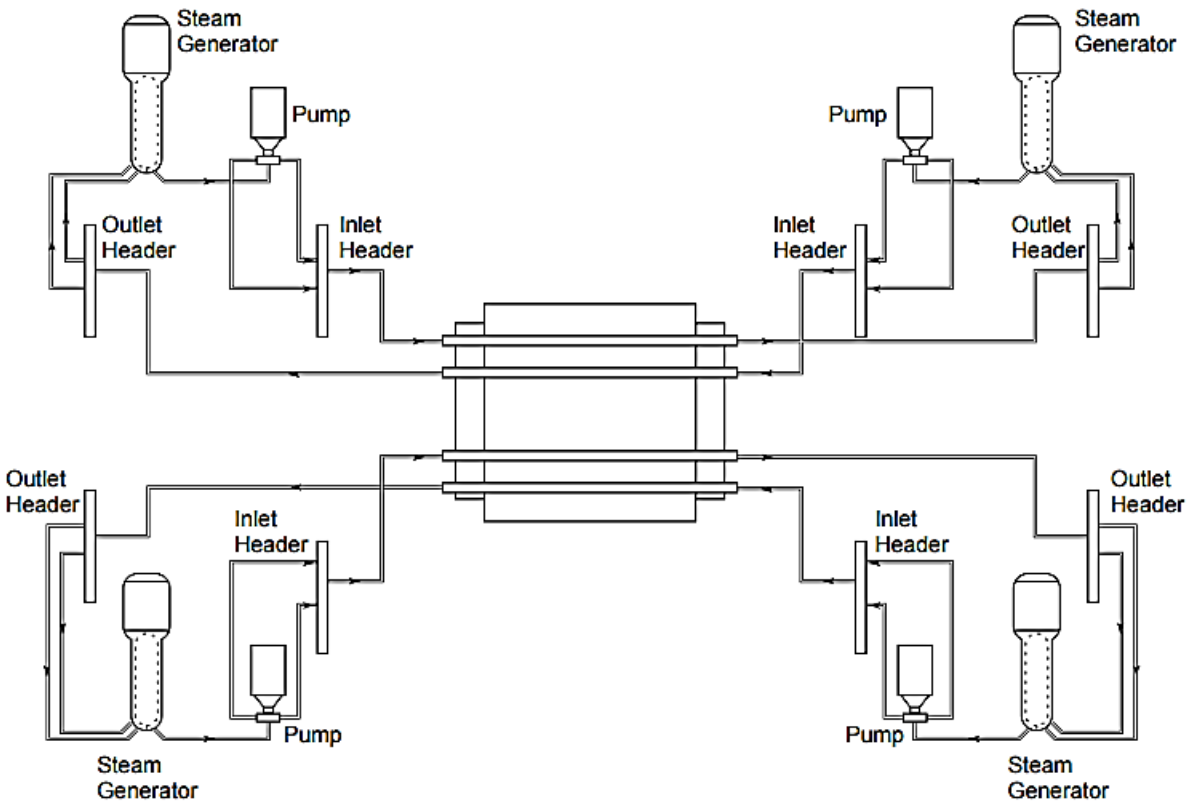

Figure 1: CANDU Primary Heat Transport System [3]

Figure 2 explains the CANDU reactor core arrangement. The heavy water coolant from the pressure tube is then passed through the lattice tube and the end fitting before transferring to the feeder pipe. The end fitting is coupled with the feeder pipe through the grayloc hub.

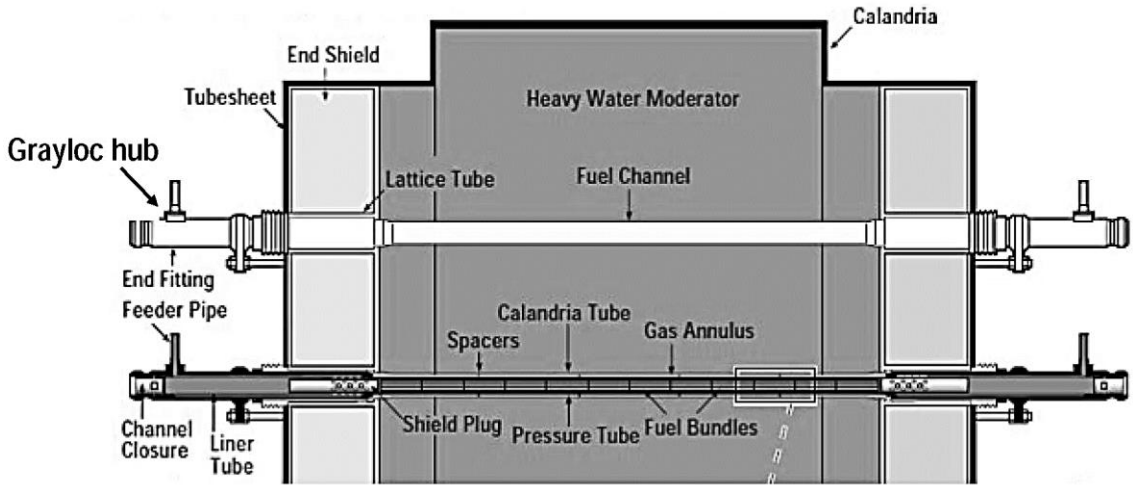

Figure 2: Calandria showing the end fittings and feeder pipe connections [56]

According to the previous studies, wall thinning at the outlet feeder pipes of the CANDU reactors is explained as a series of processes within the pipe geometry [7]. The corrosion of carbon steel in the CANDU PHT system is controlled by the behaviour of the magnetite layer [7]. This magnetite layer develops on the internal surface of the pipe and acts as a layer to protect the carbon steel pipe from further corrosion. The thickness of the magnetite layer is affected by many variables, including the fluid velocity, mass transfer, magnetite solubility, flow disturbances, wall shear stress distribution etc. At a pH of approximately 10 or greater, the magnetite solubility increases with temperature. Therefore, under normal operating conditions, the coolant is unsaturated with respect to iron as it exits the reactor core. This will enhance the dissolution of the protective oxide layer in the outlet feeder region.

A CFD model has been developed at the University of Ontario Institute of Technology to predict the shear stress distribution in various carbon steel outlet feeders of the primary coolant circuit in a CANDU reactor. Each channel of the reactor, as well as the corresponding feeder pipes, have been investigated with a slightly different heavy water coolant flowrate depending on the channel position. The coolant inlet temperature is approximately 266 °C while the outlet temperature is approximately 310 °C under a hydrostatic pressure of 10-12 MPa [4].

During this study, a CFD analysis is performed for a set of different outlet feeder pipe geometries corresponding to the unit 1 of the Darlington Nuclear Generating Station using Siemens NX 9.0 software package. Fluid flow rate, feeder pipe diameter, length of the pipe between grayloc hub and the first bend and the bend angle are considered as important parameters for the study. According to the results of the CFD analysis, the maximum wall shear stress is observed at the first bend that is downstream from the grayloc hub. The previous studies have determined the maximum rate of wall thinning at the first bend that is downstream from the grayloc hub for similar arrangements [8], [9]. The shear stress has a direct effect on the erosion of the magnetite layer, and therefore the rate of particle removal from magnetite layer is higher when the shear stress is high.

The shear stress distribution is expressed as an empirical expression of fluid Reynolds number, the length between the grayloc hub & the first bend and the bend angle. This empirical expression is benchmarked against the wall shear stress data available for a similar system in the literature. Moreover, the variation of wall shear stress and the rate of wall thinning was compared corresponding to different feeder pipes of Unit 1 at the Darlington Nuclear Generating Station.

2 LITERATURE REVIEW

2.1 Nuclear Power

With the rising global electricity consumption, there is an increasing demand for nuclear power plants across the world. Being a non-renewable source of energy, nuclear power has a lower unit cost with a reduced effect on the environment compared to other non-renewable energy sources. The energy density of nuclear resources is significantly higher compared to fossil fuels [1], given that the fission of 1 kg of uranium (U-235) liberates about 24 GWh of energy while combusting 1 kg of coal release only 2.7 to 7.5 kWh of energy [10] [11]. On the other hand, since nuclear power is independent of climatic changes such as variations of local wind patterns, unavailability of solar radiation; nuclear reactors can produce electricity throughout the year. With the high capacity factor around 90%, nuclear power has become a reliable source to satisfy the demand for baseload electricity and this has made nuclear power popular in the field of electricity generation. The growing demand for nuclear-electricity generation is well defined by the fact that there are 60 new nuclear plants under construction in 15 countries on top of the 449 nuclear reactors that were operating worldwide in April 2017 [2].

Nuclear energy in power reactors is produced by the splitting of certain heavy radio-active nuclei using a controlled chain reaction. UO_2 is the most widely used nuclear fuel to power nuclear plants. Uranium is extracted from the earth through traditional mining techniques and chemical leaching.

Different types of nuclear reactors, including Light Water Reactors (LWR), Heavy Water Reactors (HWR) and Breeder Reactors, have been meeting the global electric power demand for several decades.

2.2 Ageing in Nuclear Power Plants

While the global nuclear community is working on developing new technologies for nuclear power generation, more than 450 nuclear power reactors all over the world are getting older in the other hand. Throughout their operating lifespan of 25 to 30 year [12], the Nuclear Power Plants (NPPs) undergo the phenomenon of ageing.

In simple terms, ageing related to nuclear power plants can be expressed as the continuous degradation of material with time, resulting in reduced performance and/or safety margins of the power plant. Therefore, it is very important to consider this phenomenon, in NPPs compared to any other reactors, due to the risk of failure, and the high cost of building new ones.

According to the European Nuclear Society, by 2016, the majority of the nuclear reactors operating worldwide are older than 25 years (Figure 3) [13]. This fact has attracted global interest towards the importance of research into the ageing of nuclear power plants. Even though dedicated researchers all over the world are working on predicting and mitigating the ageing effects in NPPs, there have been failures in the nuclear industry caused by ageing and by inappropriate maintenance practices at some nuclear power plants.

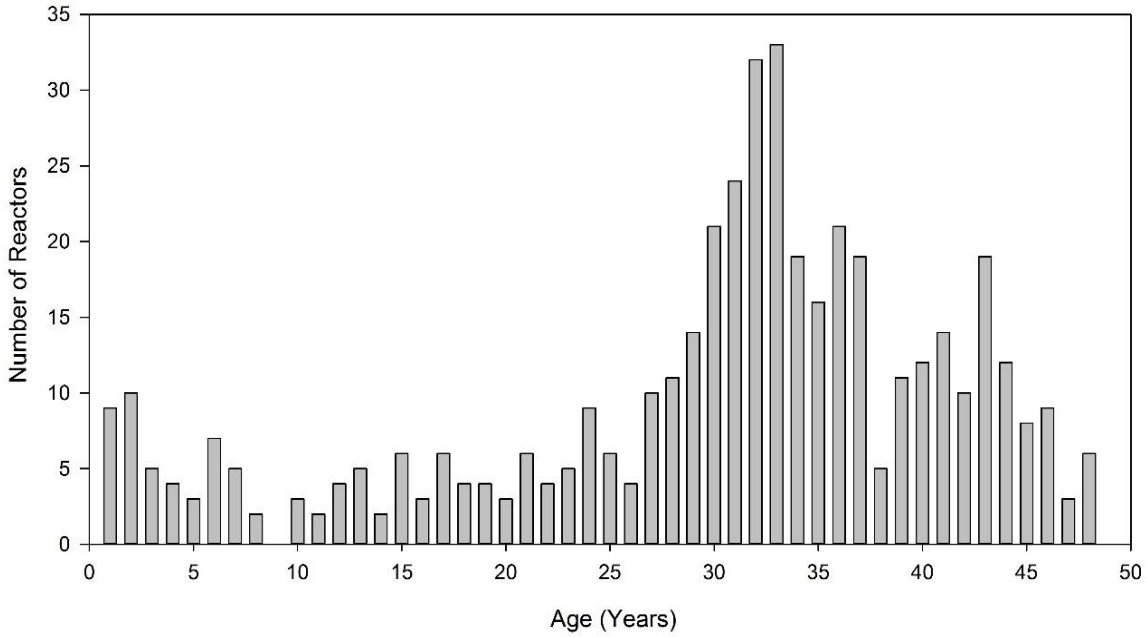

Figure 3: Number of nuclear reactors worldwide by age as of 2016 [5]

The Vermont Yankee Nuclear Generating Station began to operate in 1972 with boiling water reactors to generate 1,912 MWe of power. A series of dramatic equipment failures were recorded at this plant, which was mainly due to the ageing of the components and poor maintenance. In 2004, a failure with one of the electrical systems caused a serious fire in the turbine building resulting in an emergency plant shutdown [14]. In 2007, a cooling tower collapsed forcing the plant into an emergency shutdown [14]. After an operating life of 42 years, the reactor was permanently shut down in December 2014 [15].

In the Byron Nuclear Generating Station, one of the critical pipes that are used to cool the reactors was severely corroded. The pipe burst once the rust was removed, requiring an emergency plant shutdown (Figure 4). Corrosion of a pipe to such a degree does not happen overnight, and it is very clear that the main reason for this failure is negligence about the effects of ageing on the piping system.

Reactor pressure tubes, feeder tubes, steam generators and main condensers in CANDU reactors can be identified where the ageing effect is predominant. If the problem remains unattended, it could interrupt reactor operation or the reactor may undergo severe accidents resulting concerns in both safety and economic aspects. Constructing new nuclear plants is typically much more expensive than extending the life of the ones already in operation. As a result of these cost implications, researchers working in the field have been focusing their attention to minimize the ageing issues with nuclear power plants, and to ensure that reactors can be operated efficiently and safely with minimal interruption throughout their expected lifetime. There are different approaches that have been used to address this issue in the nuclear power industry.

Apart from the detailed inspection during the regular maintenance, lifetime prediction on different components even from the design or operation stage is another method available to deal with ageing issues. Developing predictive models based on the physics and chemistry of a component would be a good approach to predict the ageing effect on the components beforehand. Simulation is another option available to predict the

behaviour of a component and the effect of ageing towards the performance of the component in long-term operation.

Figure 4: Brushing away rust on the outer surface of a cooling water pipe at the Byron nuclear plant created a hole [55]

2.3 Importance of Numerical Simulations in Nuclear Power Plants

In general, numerical simulations are the imitation of a real-world process or system over time. Therefore, simulation can be used in many contexts, such as performance optimization, safety engineering, testing, training etc. As the first step of the simulation, it is required to develop a model representing the key characteristics of the actual system or the process [16]. Theoretical and Empirical approaches are widely used in developing models to simulate the response of a system. Once the model is developed, the simulation results should be compared with experiments to validate the accuracy of the model.

There are several advantages to using simulations, which have led to an increase in the applicability of simulations in different subject areas. One such key advantage is that simulations can be used to observe the behaviour of a process or a system under different external conditions, which may otherwise cost a large amount of money and time to observe experimentally. Finally, simulations can be used to predict the behaviour of a physical system or a process to assess its suitability even before building it.

It is not an exaggeration to mention that there is a large community of researchers all over the world, who are dedicated to nuclear engineering. They are working on developing models and simulations to predict or study the behaviour of nuclear power-related systems.

In 2009, Kurt et al. have investigated CFD Modelling & Simulation processes, which include CAD geometry development. They have done meshing, simulation, and post-processing of results using an arbitrary fuel assembly design as a benchmark. This study has focused on a 19 – pin fuel assembly, which is similar to the Advanced Burner Test Reactor (ABTR). Three turbulence models that are comprised of two-equations, including the k–ε, k–ω and Menter's Shear Stress Transport (SST) have been evaluated. Predictions for velocity, temperature, and pressure distribution have also been shown [17].

D. Chang and S. Tavoularis have used numerical techniques to solve the unsteady Reynolds Averaged Navier–Stokes (RANS) equations combined with a Reynolds stress model to determine fully developed isothermal turbulent flow around a CANDU fuel bundle. For the study, the authors have considered a 60º sector of a 37-rod fuel bundle. During the study, the authors have figured out that this flow contained large-scale coherent structures, which affected strongly the local velocity fluctuations, especially near the gaps between rods or between rods and the surrounding walls [18].

Shaohong Zhang et al. have developed a CANDU refueling optimization method. The method is comprised of two-step mathematical programming where the first step is to select the weekly refueling candidates, and the second step is to determine the detailed weekly refueling scheme with the prescribed candidates. The authors have validated their mathematical model with the operation history of 392 full power days of Qinshan CANDU 6 reactor in China and demonstrated a good regional power and core reactivity control [19].

Hangbok Choi and Do Heon Kim have developed an optimum refueling simulation method which can be applicable for a CANDU 6 reactor. The authors have developed this simulation with the objective of maintaining the operating range of the zone controller

unit water level so that the reference zone power distribution is reproduced after the refueling operation. By using a system of equations of the zone power, the authors have obtained a realistic model of the zone controller level response [20].

Araz Sarchami et al. have conducted three-dimensional numerical simulations on a full-scale CANDU moderator system to determine the transient variations of the temperature and velocity distributions inside the tank. The results have shown that the flow and temperature distributions inside the moderator tank are three dimensional and no symmetry plane has been identified. The authors have investigated that the upward moving buoyancy-driven flows and the downward moving momentum driven flows in the center region of the tank result in the formation of circulation zones. Since the moderator tank operates in the buoyancy-driven mode, any small disturbances in the flow or temperature make the system unstable and asymmetric [21].

Validation of a numerical model against experimental data is one of the main challenges that the researchers face. In most of the scenarios, unavailability of sufficient or accurate experimental data makes it difficult to validate the simulations. In such scenarios, the researchers could follow the guidelines for a numerical verification of the results to demonstrate the confidence about the model.

Apart from the validation and verification of the results, requirement of high computational power to conduct the analysis such as CFD modeling is also a significant challenge. Reasonable approximations and symmetry of the geometry could be used to reduce the computational power demand.

2.4 Incorporating the Ageing Effects with the Nuclear Power Plant Simulations

The early stage development of the simulations was mainly focused on the performance of the process and safety systems of nuclear power plants. These simulators are capable of predicting the response of the nuclear reactor and its associated systems to changes in operating parameters. With the advancement of science and technology, the researchers

have started working to incorporate the ageing effects of the nuclear systems to the existing performance models.

'An accurate analysis of maintenance cost of structures experiencing stochastic degradation' by T. Cheng & M. D. Pandey discusses a finite time model that has developed to compute the expected cost for a maintenance program.

Another example is 'Predictive based monitoring of nuclear plant component degradation using a support vector regression approach' by Miltiadis Alamaniotis and Lefteri H. Tsoukalas, which discusses an online surveillance approach that can focus on critical parameter degradation of a nuclear power plant. Eventually, this system allows on-time maintenance/ replacement of components and hence minimize potential plant malfunctions.

In 2009, X. Yuan et al. have developed a model to predict pitting flaws in steam generator tubes of a nuclear power plant. The proposed model was developed based on the in-service inspection data extracted through eddy current inspections and is able to predict the actual pit number, the actual pit depth and the maximum pit depth [22]. The authors have focused their study on the steam generator tubes and stressed that if the pit growth is left unchecked, it would develop into a leakage, resulting in a Loss of Coolant Accident (LOCA).

In 2012, A. Mohan and M. Hassan developed a numerical model to predict the vibration response of a CANDU fuel bundle and the associated fretting wear in the surrounding pressure tube. For this study, the authors considered turbulence-induced excitation due to the flow of coolant inside the fuel channel and seismic excitation. [23].

Jong Chull Jo and Dong Gu Kang have focused their study on developing a CFD model to calculate the shear stress distribution in the feeder pipes which is a critical factor to be considered in predicting the local regions of feeder pipes, that are highly susceptible to flow-accelerated corrosion induced wall thinning [24].

M.D Pandey et al. developed an advanced probabilistic model to predict the feeder wall thinning by flow-accelerated corrosion. The proposed model has been calibrated against a set of wall thickness measurement data collected during various inspection outages in a CANDU 6 nuclear-electric generating station [25].

There are many more studies being conducted to develop simulations that can predict changes in the physical structure as well as with the operating parameters in critical components of a nuclear power plant over the operating time. When analyzing these studies, it is evident that both probabilistic and deterministic approaches are being used to develop the predictive models.

2.5 CANDU Primary Heat Transport System

The CANDU PHT system consists of two loops where each loop has two inlet headers and two outlet headers that are covering half of the reactor core each [3]. The PHT main circulating pumps deliver the coolant from the outlet of the steam generators to the reactor inlet headers. Feeder pipes are used to transfer cooling water from the inlet header to the fuel channels in the reactor. This heavy water coolant absorbs the thermal energy liberated due to the fission reaction in the fuel bundles and transfers it to the reactor outlet header through the outlet feeder pipes. The hot heavy water is then passed through the primary side of the steam generator to transfer the thermal energy to the secondary side light water that is at a lower pressure.

Since the primary mode of cooling in the reactor core is through the pressurized heavy water, it is important to have a high integrity and availability of the PHT system to ensure the safe and uninterrupted operation of the reactor.

2.6 Ageing in CANDU Primary Heat Transport System - Feeder Wall Thinning

When considering the ageing effects of the PHT system, wall thinning of outlet feeder pipes is identified as one of the main issues faced by CANDU power plants. Figure 5 illustrates the feeder pipe arrangement of a typical CANDU reactor [26]. Since the heavy water that flows through the feeder pipes is at elevated temperature and pressure, feeder pipes are acting as pressure boundaries of the reactor. There is a minimum level of wall thickness defined to maintain the integrity of the pressure boundary considering the operating conditions and factor of safety. Therefore, a higher rate of wall thinning at CANDU outlet feeder pipes creates operational and safety concerns. Even though the routine maintenance procedures are followed, failure in a feeder pipe would create numerous consequences such as loss of coolant from the reactor, difficulties of replacing the failed feeder pipe and unplanned shut down of the unit. Therefore, it is important to develop a methodology to predict the lifetime of the feeder pipes in advance, so that required replacements could be done during planned reactor outages.

Higher rates of wall loss within the feeder pipes were reported for the first time from the Point Lepreau Nuclear Generating Station in New Brunswick. This issue was eventually confirmed at all CANDU generating stations [27].

From the early 1990s, CANDU designers and engineers began to investigate the reasons behind the feeder wall thinning that was occurring at a higher than expected rate. During the early stage of the investigation, much of the effort was focused on developing a technical understanding of the mechanisms responsible for feeder degradation and the FAC was identified as the main reason behind the unexpected wall loss of carbon steel piping [28].

2.6.1 Materials of Construction

Carbon steel is used as the material of fabrication for the inlet and outlet feeder pipes of CANDU reactors. During the fabrication process, pipes are bent to meet the desired bend angle and radius. As a result of this process, pipe wall at the intrados of the bend is getting thicker compared to the extrados of the bend. The alkalinity of heavy water that is passing through the feeder pipes is maintained such that 10.2 <pH< 10.8 [27].

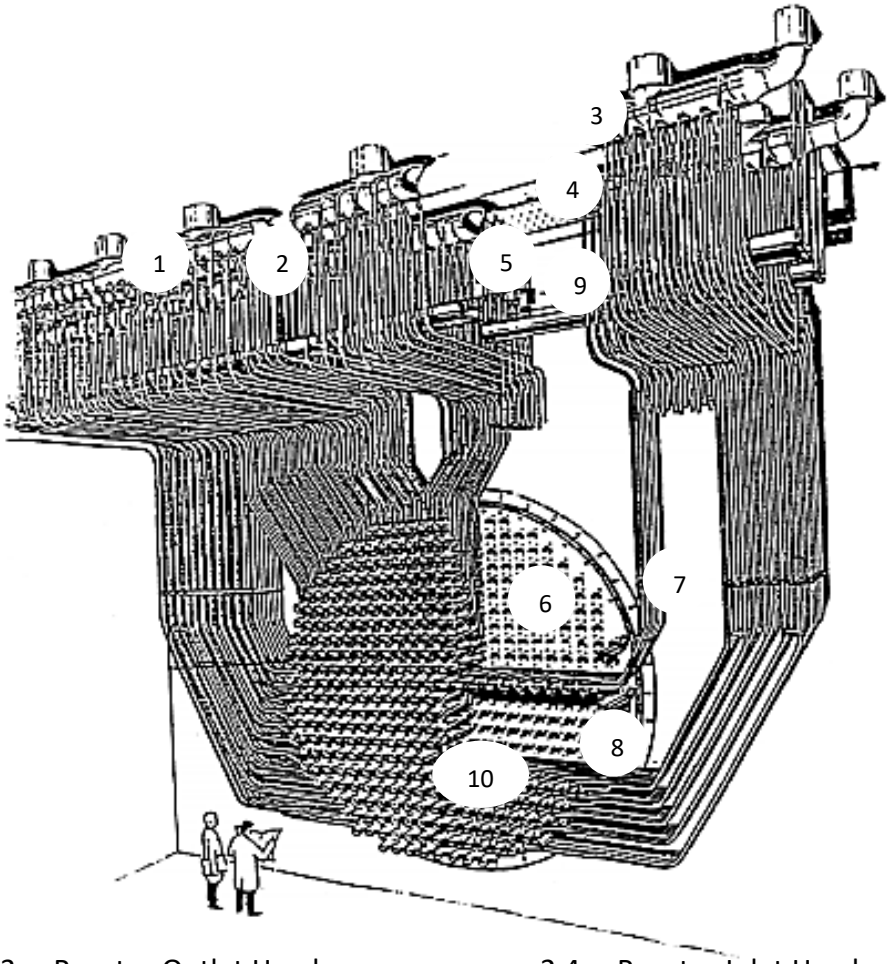

1,3	Reactor Outlet Header	2,4	Reactor Inlet Header
5	Feeder Tuber Upper Support	6	Calandria End Shield Face
7	Tube Spacers	8	Support Brackets
9	Walkway	10	End Fittings

Figure 5: Feeder arrangement of a typical CANDU reactor [21]

2.6.2 Flow Accelerated Corrosion

Upon identifying FAC as the main reason behind the feeder wall thinning, further investigations determined that the wall thinning at higher rates was observed at the outlet feeder pipes of CANDU reactors and at the first bend from the grayloc hub [29]. With these findings, researchers were more curious to study the reasons that caused considerable wall thinning only at the outlet feeders, and to develop a mechanism to understand the scenario. As a result of continuous effort and experiments, researchers were able to identify several factors that increase the FAC rate. Corrosion chemistry and mass transfer theories along with the concept of FAC explain the reasons for having a higher rate of wall thinning at the outlet feeders compared to the inlet feeders.

Dissolved Oxygen reacts with carbon steel to form a layer of magnetite, Fe_3O_4, which is comprised of one ferrous species (Fe^{2+}) and two ferric species (Fe^{3+}) on the internal surface of a feeder pipe. This layer acts as a protective layer against further corrosion. In the turbulent boundary layer, there is a thin region near the surface where the flow remains laminar, and this is known as the laminar sub-layer [30]. The Fe ions tend to diffuse from the oxide layer to the laminar sub-layer of the fluid (heavy water) which flows inside the feeder pipe. Depending on the concentration difference of Fe ions in the laminar sublayer and the bulk fluid, the Fe ions get transferred across the laminar sublayer to the turbulent layer (bulk fluid) in the feeder pipe. D.H. Lister et al. has derived the following expression to represent the rate of wall loss in outlet feeder pipes [29].

$$\dot{m} = \frac{k_m \cdot k_d}{(0.5k_m + k_d)} (C_{sat} - C_b) \quad (1)$$

Where;

- $\dot{m}$ Rate of mass loss at wall (mol/s),
- k_m Mass transfer coefficient (m/s),
- k_d Magnetite dissolution kinetic constant (m^2/s),
- C_{sat} Iron saturation concentration (mol/m^3),
- C_b Iron concentration in bulk coolant (mol/m^3).

In a typical CANDU reactor, the reactor inlet header operates at around 266 °C and 11.25 MPa while the reactor outlet header is around 310 °C and 10 MPa [4]. The pH level of the PHT coolant is generally maintained in the range of 10.2 to 10.8 in order to minimize the corrosion rate of carbon steel [27]. According to Figure 6, the solubility of Fe ions increases significantly through the temperature range of 200 °C to 300 °C with a solution pH of 10.2. This implies that the ability of the coolant to absorb more Fe ions increases as it passes through the pressure tube, due to the fact that the fluid gets heated up by absorbing the energy liberated from the fuel bundles (point A in Figure 6). Bulk fluid is at a higher temperature and is still not saturated in terms of Fe ions when it passes through the outlet header. Therefore, it has the capacity to absorb more Fe ions from the magnetite layer at the outlet feeder walls resulting in a considerable rate of wall thinning. When the coolant passes through a bend of the feeder pipe, shear forces acting on the tube wall initiate the wall thinning. Since the coolant is unsaturated with respect to Fe ions, it enhances the wall thinning process resulting in a significant rate of wall loss compared to the inlet feeder pipes.

However, the heavy water cools back to a lower temperature at the steam generator due to the fact that heat is transferred to the light water at the secondary side to generate steam. Therefore, the solubility factor reduces (point B in Figure 6) with the temperature of the cooling water and the heavy water becomes saturated with Fe ions resulting in the deposition of Fe on the steam generator tube walls. As a result, the heavy water coolant passing through the inlet feeder pipe becomes a solution which is saturated with Fe ions. Hence, it will not be able to capture any more Fe from the inlet feeder wall. Although the flow velocities are essentially the same in both inlet and outlet feeders, the feeder wall thinning only occurs to a significant level at the outlet feeder pipes.

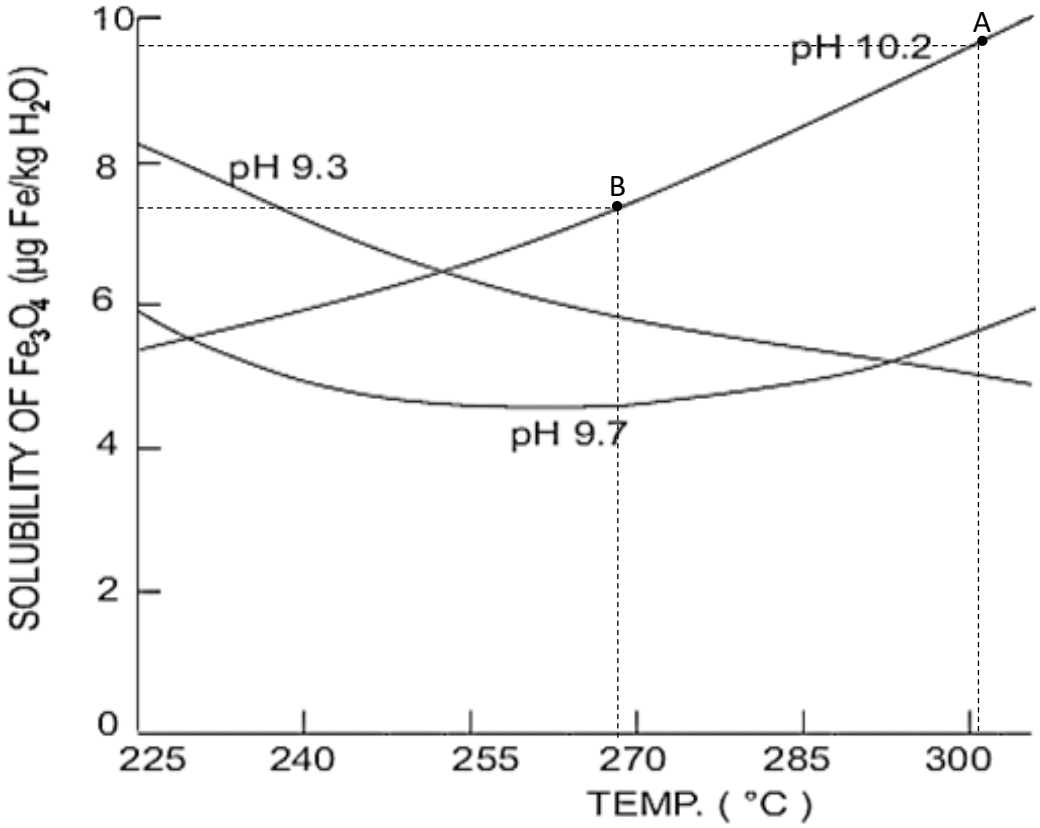

Figure 6: Solubility of magnetite as a function of temperature at different pH [53]

3 MODEL DEVELOPMENT

The Faculty of Energy Systems and Nuclear Science at UOIT is equipped with Siemens NX 9.0 that is an advanced CFD software package. NX 9.0 was used to model the outlet feeder pipe geometries of the reactor unit 1 at the Darlington Nuclear Generating Station, using the design and operational details provided by Ontario Power Generation. A comprehensive CFD analysis was performed to analyze the fluid flow profile inside the outlet feeder pipes and the shear stress distribution at pipe walls.

The CFD approach is identified to be safe, cost-effective and less time consuming compared to an experimental approach. If an experimental approach is used towards this study, an experimental setup to be designed and fabricated similarly to the feeder pipe arrangements in Darlington unit 1 reactor. Since there are 21 different types of feeder pipes, it would be cost a lot of money and time to fabricate those geometries. On the other hand, it will create safety concerns since the heavy water flowrate is required to be maintained under elevated pressure and temperature.

3.1 Design and Operational Details

Table 1 below summarizes the design & operational details for different types of outlet feeder pipes in unit 1 of the Darlington Nuclear Generating Station. Figure 7 illustrates the physical arrangement of the outlet feeder pipes. The detailed design drawings are available in APPENDIX - A.

Table 1: Design & operational details for different feeder pipes in Darlington unit 1

Bend Type	Nominal size (in)	Feeder pipe diameter (mm)	Length between grayloc hub and the first bend (mm)	Angle of the first bend θ_1 (°)	Heavy water flow rate (kg/s)	Typical Feeder
A	2	49.3	45.5	40.8	16.04	A12E
B	2	49.3	38.6	48	18.98	B09E
C	2.5	59	43.5	48	17.00	B08W
D	2	49.3	10.4	73	18.64	C07W
E	2.5	59	15.3	73	24.39	C12E
F	2	49.3	38.6	48	13.58	C05W
G1	2	49.3	10.4	73	17.29	D20W
H1	2.5	59	15.3	73	25.03	S05E
I	2	49.3	10.4	73	13.45	E03W
J	2.5	59	15.3	73	27.63	E10E
K1	2	49.3	10.4	73.1	16.14	F03E
K2	2	49.3	10.4	73.1	19.40	G03W
K3	2	49.3	10.4	73.1	14.21	J24E
K4	2	49.3	10.4	73.1	15.25	K24W
K5	2	49.3	10.4	73.1	16.57	L01W
L1	2.5	59	15.3	73.1	27.03	S07E
L2	2.5	59	15.3	73.1	27.97	M12W
L3	2.5	59	15.3	73.1	27.49	S09E
L4	2.5	59	15.3	73.1	27.80	M09E
L5	2.5	59	15.3	73.1	27.89	U11E
L6	2.5	59	15.3	73.1	27.61	T12E
M	2	49.3	3.1	41	16.59	O24W

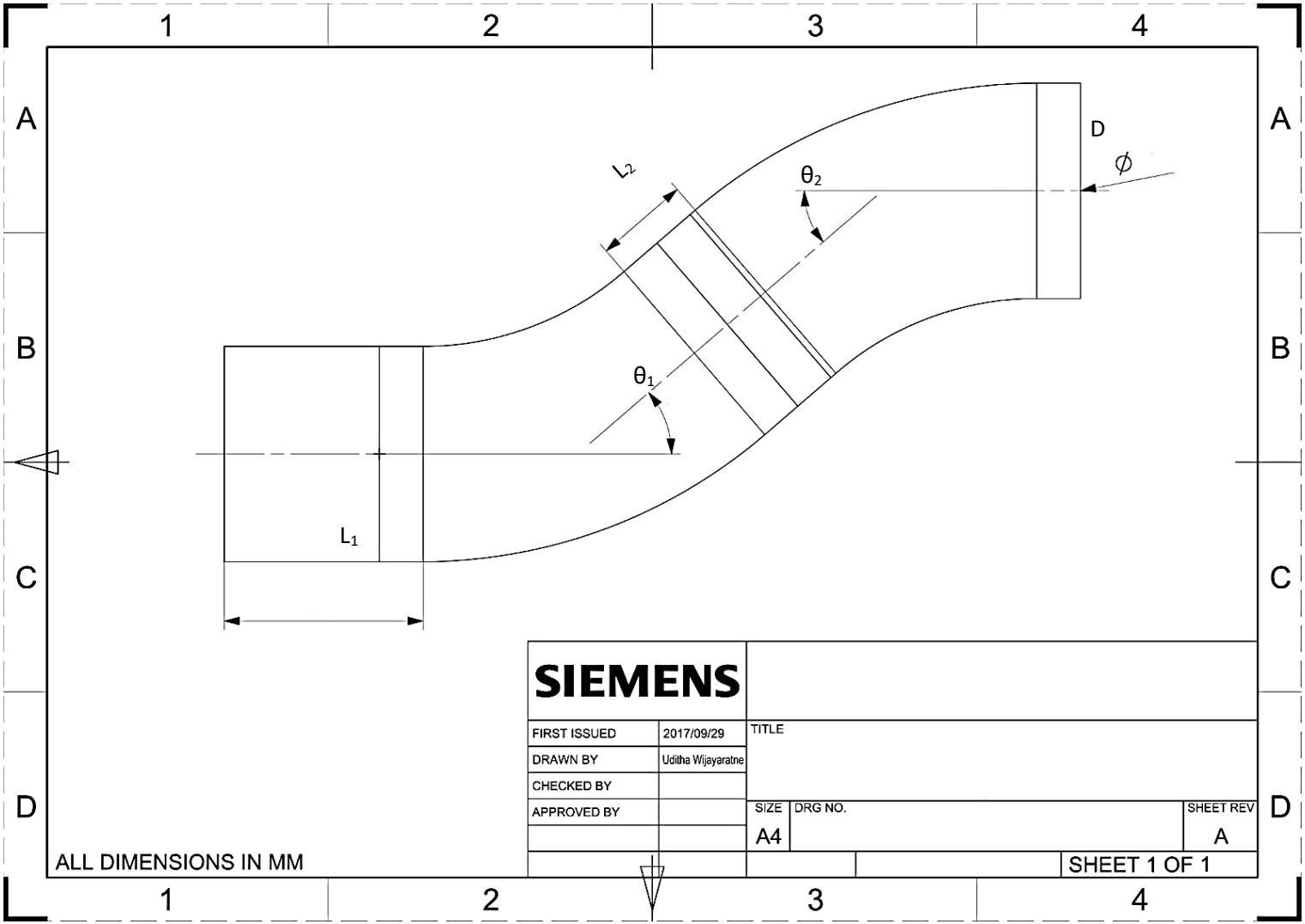

Figure 7: Design details of the outlet feeder pipe

3.2 Computer-Aided Design

The fluid body from the end fitting to the 3rd bend of the outlet feeder pipe was developed as a CAD geometry using Siemens NX 9.0 based on the design details provided by Ontario Power Generation. The overall model is comprised of several components and listed in Table 2.

Table 2: Different components of the CFD model

Component Name	**Details**
End fitting (E1 – E3)	This segment represents the fluid body in between the pressure tube and the grayloc hub
Grayloc hub (E3)	Connects end fitting to the outlet feeder pipe
L1	L1 is the straight pipe section in between grayloc hub and the 1st bend of the feeder pipe.
B1	B1 is the bend that is in between L1 and L2 of the feeder pipe
L2	L2 is the straight pipe section in between 1st and 2nd bends of the feeder pipe
B2	B2 is the bend that is in between L2 and L3 of the feeder pipe
L3	L3 is the straight pipe section after the 2nd bend

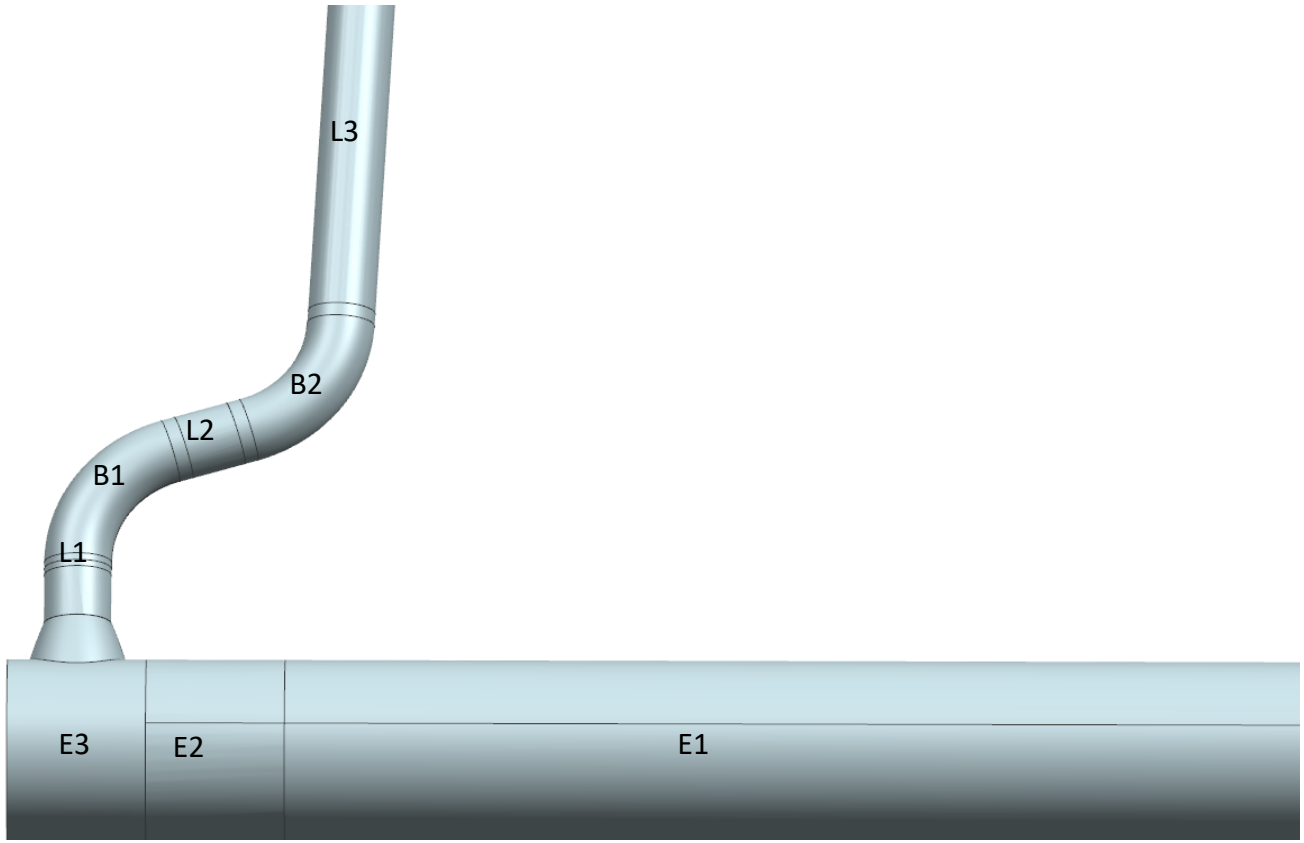

Figure 8: Feeder pipe geometry

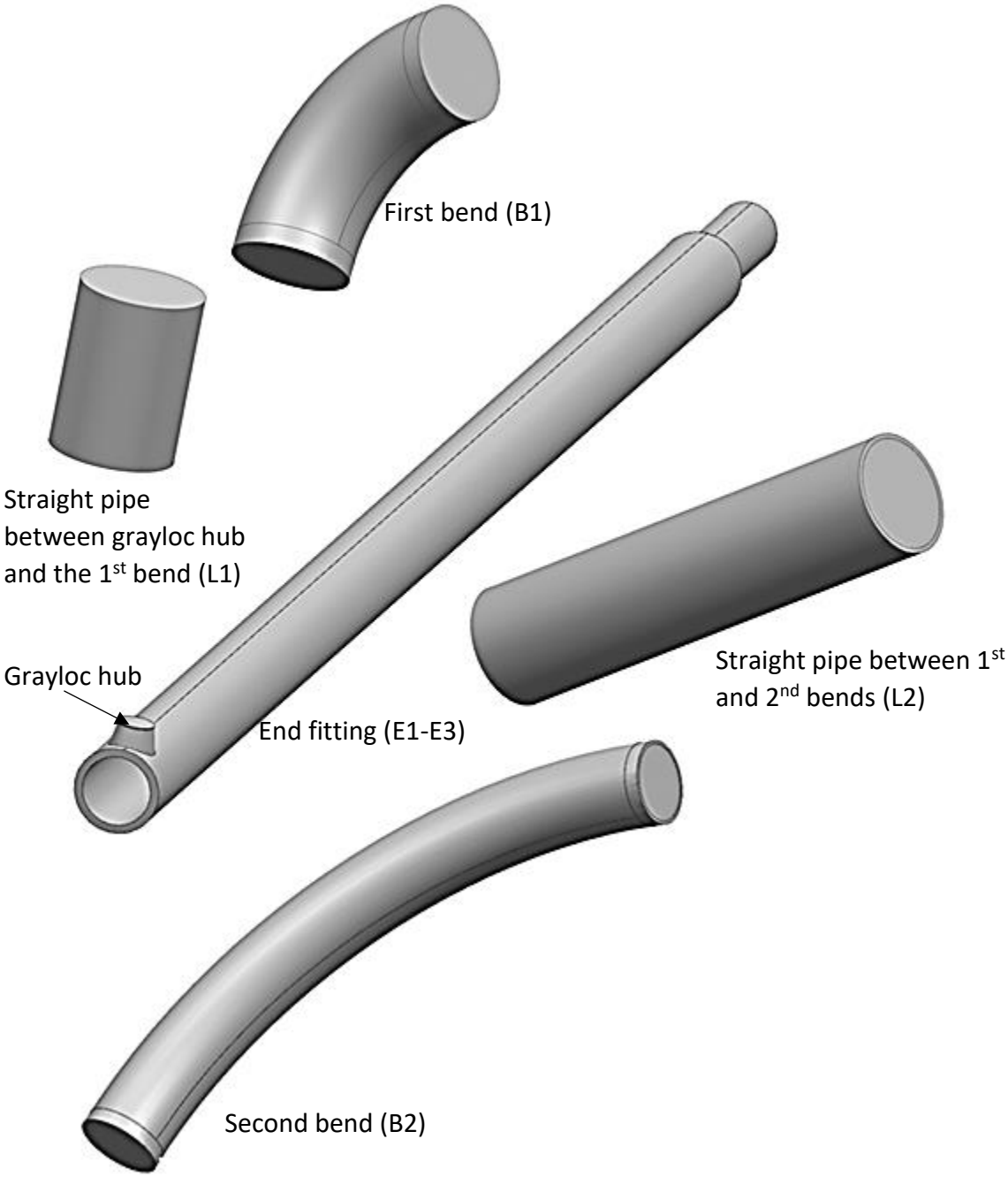

Figure 9: Different segments of the geometry

3.3 Meshing Techniques

When considering the CFD analysis, generation of a proper mesh is challenging and plays a vital role in the analysis process. The solution accuracy of the CFD analysis highly relies on the mesh resolution and quality. In the other hand, high mesh resolution demands higher computational power.

During the literature study, it was observed that the wall thinning is significant on the internal face of the pipe wall at the first bend geometry (B1). Therefore, the fluid dynamics and the related mechanical forces should be calculated more precisely in this region and a finer mesh should be used for the purpose of achieving accurate results. Even though it is possible to use a very fine mesh for the entire geometry, it would lead to an increased computational power requirement. Therefore, a comparatively large mesh size was used for the areas of the geometry that are not significantly important for the study. However, the mesh size transition was done gradually.

Developing an optimal mesh for a CFD study is not a simple task. There is no straightforward way of defining a perfect mesh for a CFD study. It all depends on the geometry, fluid dynamics involved, required level of accuracy as well as the limitations on software and available computational power. Therefore, development of an optimum mesh would be a gradual process that always comprised of trial and error methods. From the beginning of this study, different types of meshing techniques were tried and their pros and cons evaluated.

As the first approach, a coarse 3D mesh (Figure 10 - a) was developed to identify the behaviour of the system in the CFD environment. The main drawback with this mesh was that it is too coarse and cannot capture appropriate information in the laminar sub-layer. Instead, if a finer mesh size is defined for the geometry, it will generate smaller mesh cells all over the volume (Figure 10 - b) resulting an increased computational power requirement. On the other hand, it is not necessary to have a finer mesh at the center of the pipe geometry since the analysis is focused on the near wall laminar sub-layer.

As a solution to this issue, a 2D mesh was developed on the cross-sectional surface of the pipe segment that is having a smaller mesh close to the pipe wall and larger mesh size at the center of the pipe. Smaller mesh size close to the wall was defined using the 'Mesh Control' tool in NX. The only drawback of this mesh was the lack of control on mesh size transition. This 2D mesh was then swept along the pipe geometry to make a 3D swept mesh and is shown in Figure 11. Siemens NX also provides the ability to change the axial grid space by changing source element size. It is also possible to use a fixed axial grid space or a varying axial grid space depending on the geometry based mesh requirements.

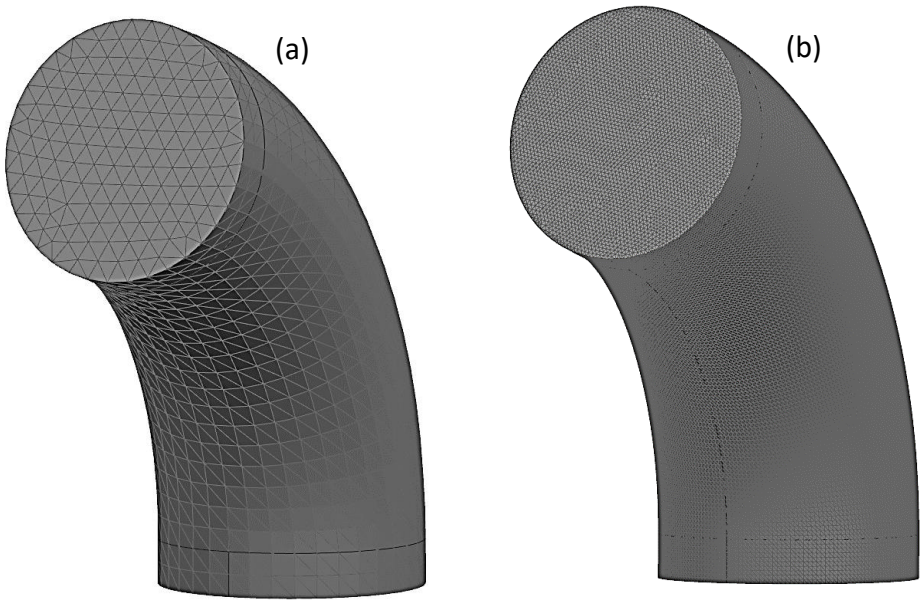

Figure 10: Coarse and finer 3D meshes

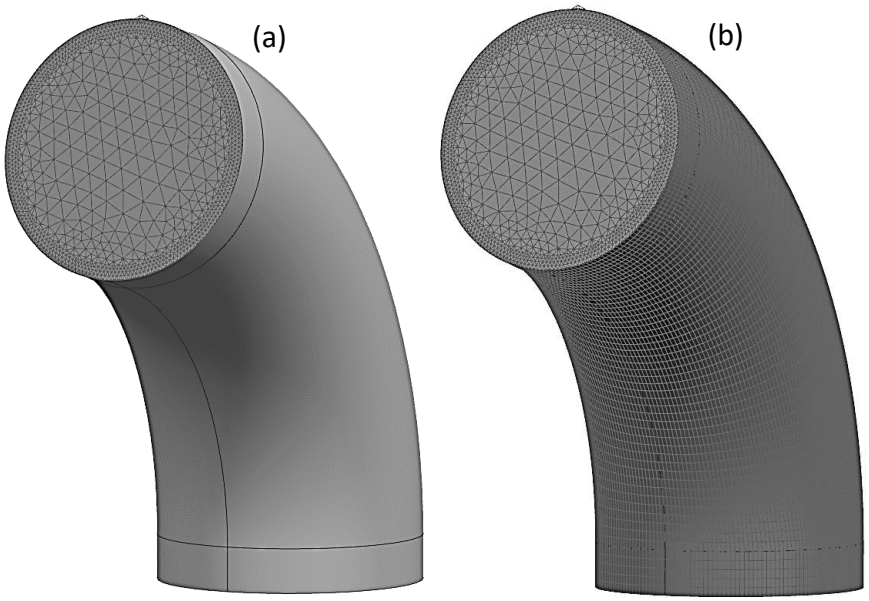

Figure 11: 3D swept mesh

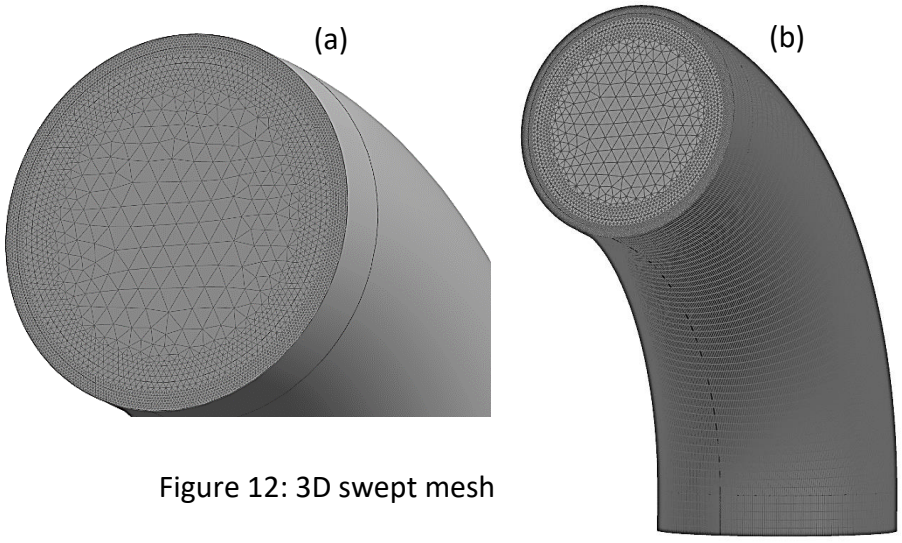

Figure 12: 3D swept mesh

Table 12 under section 1.1 summarizes the different fluid meshes that are used throughout the geometry to achieve accurate solutions while consuming optimum computational resources.

3.4 Y Plus

Y plus or y^+ is defined as a non-dimensional wall distance for a wall-bounded flow. The relationship between the y^+, u_*, y and v is given by;

$$y^+ = \frac{u_* \cdot y}{v} \qquad (2)\ [31]$$

Where u_* is the friction velocity at the nearest wall (m/s)

y is the distance to the nearest wall (m)

v is the local kinematic viscosity of the fluid (m^2/s)

Since the objective of the study is to model the behaviour of the fluid close to the pipe wall, the y^+ value plays a vital role in the analysis. Having a smaller y^+ value implies more mesh nodes inside the fluid domain that is close to the wall surface (i.e. within the laminar sub-layer).

The rule of thumb is to maintain, $y^+ \leq 1$ for K-Omega and SST models in order to get accurate results within the laminar sublayer, which is close to the pipe wall [31]. However, this should be further studied to figure out the effect of y^+ on the final solution in order to determine the near wall mesh size requirements. Seven different mesh models were compared and the results are summarized in APPENDIX - B.

3.5 Turbulent Model

The heavy water coolant that is flowing through the outlet feeder pipe is identified as a turbulent flow. This can be further verified fluid dynamically by analyzing the Reynolds number.

The Re number for a fluid flowing through a circular pipe is defined as,

$$Re = \frac{\rho U d}{\mu} \quad (3)$$

Where

ρ – Fluid density (kg/m^3) d – Pipe diameter (m)

U – Fluid velocity (m/s) μ – Dynamic viscosity of the fluid (Pa.s)

Considering the design and operational details for the M13 outlet feeder pipe as in Table 1 above along with ρ = 676 kg/m^3 and μ = 79.751x10^{-6} Pa.s [32],

$$Re = \frac{676 \times 13.47 \times (59 \times 10^{-3})}{79.751 \times 10^{-6}}$$

$$Re = 6.74 \times 10^6$$

The critical Re number for Laminar to Turbulence transition is 1200 [30]. Since the above calculated Re number is greater than the critical value, the flow is said to be fully turbulent.

There are several methods used to perform turbulent flow analysis in terms of CFD. One such method is the Direct Numerical Simulation (DNS) to obtain the exact numerical solutions to the unsteady Navier-Stokes equations. DNS is only applicable as a research tool at relatively low Reynolds numbers and it demands high computational power [33].

The widely used method of analyzing turbulent pipe flow is by solving the RANS equations, which are time-averaged equations of motion for fluid flow. Although the RANS equations are primarily used to describe steady flows, RANS equations can be used to get approximate time-averaged solutions to the Navier–Stokes equations. It should be

noticed that with these approximations, the computational power demand is drastically reduced compared to the DNS method.

There are different types of RANS models used and the following turbulent models are available with Siemens NX9.0.

- Fixed Turbulent Viscosity
- Mixing Length
- K-Epsilon
- K-Omega
- Shear Stress Transport (SST)
- Large Eddy Simulation (LES)

Since this study required to analyze the distribution of wall shear stress of the inner pipe wall at the first bend, it is important to select a turbulent model that works well on the near wall laminar sub-layer.

SST and K-Omega are widely used turbulence models with a higher level of accuracy in near-wall analysis compared to other RANS models [24], [33]. Moreover, the K-Omega model converged with a lower solution time compared to SST, with an acceptable level of tolerance in the solution.

However, the best turbulence model should be selected considering the geometry, flow conditions, required parameters and level of accuracy. For this study, K-Omega, SST and Fixed turbulent viscosity models were compared against each other to select the best turbulent model for the study. In all scenarios, similar geometry and boundary conditions were used. In order to reduce the computational time, a simplified pipe geometry along with the physical dimensions of the first bend (B1) was used for the comparison. According to the turbulent model comparison under APPENDIX - C, the k-Omega model was selected for this study.

3.6 k-Omega Model

The k-ω model solves for two variables: k, the turbulence kinetic energy; and ω (omega), the specific rate of dissipation of the turbulence kinetic energy.

The two-equation model written in conservation form is given by [34]

$$\frac{\partial(\rho k)}{\partial t} + \frac{\partial(\rho u_j k)}{\partial x_j} = P - \beta^* \rho \omega k + \frac{\partial}{\partial x_j}\left[\left(\mu + \sigma_k \frac{\rho k}{\omega}\right)\frac{\partial k}{\partial x_j}\right] \tag{4}$$

$$\frac{\partial(\rho \omega)}{\partial t} + \frac{\partial(\rho u_j \omega)}{\partial x_j} = \frac{\gamma \omega}{k} P - \beta \rho \omega^2 + \frac{\partial}{\partial x_j}\left[\left(\mu + \sigma_\omega \frac{\rho k}{\omega}\right)\frac{\partial \omega}{\partial x_j}\right] + \frac{\rho \sigma_d}{\omega}\frac{\partial k}{\partial x_j}\frac{\partial \omega}{\partial x_j} \tag{5}$$

Where

$$P = T_{ij}\frac{\partial u_i}{\partial x_j} \tag{6}$$

$$T_{ij} = \mu_t\left(2S_{ij} - \frac{2}{3}\frac{\partial u_k}{\partial x_k}\delta_{ij}\right) - \frac{2}{3}\rho k \delta_{ij} \tag{7}$$

$$S_{ij} = \frac{1}{2}\left(\frac{\partial u_i}{\partial x_j} + \frac{\partial u_j}{\partial x_i}\right) \tag{8}$$

and the turbulent eddy viscosity is computed from

$$\mu_t = \frac{\rho k}{\hat{\omega}} \tag{9}$$

Where

$$\hat{\omega} = max\left[\omega, C_{lim}\sqrt{\frac{2\bar{S}_{ij}\bar{S}_{ij}}{\beta^*}}\right] \tag{10}$$

$$\bar{S}_{ij} = S_{ij} - \frac{1}{3}\frac{\partial u_k}{\partial x_k}\delta_{ij} \tag{11}$$

The constants and auxiliary functions are

$$\sigma_k = 0.6 \qquad C_{lim} = \frac{7}{8} \qquad \beta^* = 0.09 \qquad \beta_0 = 0.0708$$

$$\sigma_\omega = 0.5 \qquad \beta = \beta_0 f_\beta \qquad \gamma = \frac{13}{25}$$

$$f_\beta = \frac{1+85X_w}{1+100X_w} \tag{12}$$

$$X_w = \left|\frac{\Omega_{ij}\Omega_{jk}\hat{S}_{ki}}{(\beta^*\omega)^3}\right| \tag{13}$$

$$\hat{S}_{ki} = S_{ki} - \frac{1}{2}\frac{\partial u_m}{\partial x_m}\delta_{ki} \tag{14}$$

$$\Omega_{ij} = \frac{1}{2}\left(\frac{\partial u_i}{\partial x_i} - \frac{\partial u_j}{\partial x_j}\right) \tag{15}$$

$\sigma_d = 0$, for $\left(\frac{\partial k}{\partial x_j}\frac{\partial \omega}{\partial x_j} \leq 0\right)$ $\quad$ $\sigma_d = \frac{1}{8}$, for $\left(\frac{\partial k}{\partial x_j}\frac{\partial \omega}{\partial x_j} > 0\right)$

$$\gamma = \frac{\beta_0}{\beta^*} - \frac{\sigma_\omega \mathcal{K}^2}{\sqrt{\beta^*}} \tag{16}$$

where $\mathcal{K} = 0.40$

The k-ω model is useful for many applications where the k-ε model is not accurate. Internal flows, flows that exhibit strong curvature and separated flows are some example scenarios where the k-ω model is more accurate over k-ε model [35].

3.7 Material Properties

CANDU PHT systems use heavy water (D_2O) as the primary coolant. Deuterium being a natural isotope of hydrogen, heavy water, and light water shows significant deviation in physical properties. Table 3 compares some of the important physical properties of light water and heavy water.

Table 3: Comparison of physical properties of H_2O and D_2O [36] [37]

Property	**Light Water (H_2O)**	**Heavy Water (D_2O)**
Density at 20 °C	0.998 g/cm^3	1.105 g/ cm^3
Viscosity at 20 °C	1.002E-03 Pa.s	1.247E-03 Pa.s
Molecular weight	18.01 g/mol	20.03 g/mol
Vapor pressure at 20 °C	2.34E-02 bar	2.73E-02 bar

Since the Siemens NX 9.0 does not contain heavy water with its built-in material library, D_2O was introduced to the material library as a custom material.

A simple pipe geometry with B1 bend was used to simulate with light water and heavy water as the fluid to compare the difference in wall shear stress distribution. Figure 13 and Figure 14 below illustrate the difference in wall shear stress distribution on the pipe bend geometry and the maximum wall shear stress was observed as 3.057 kPa and 2.955 kPa under light water and heavy water respectively.

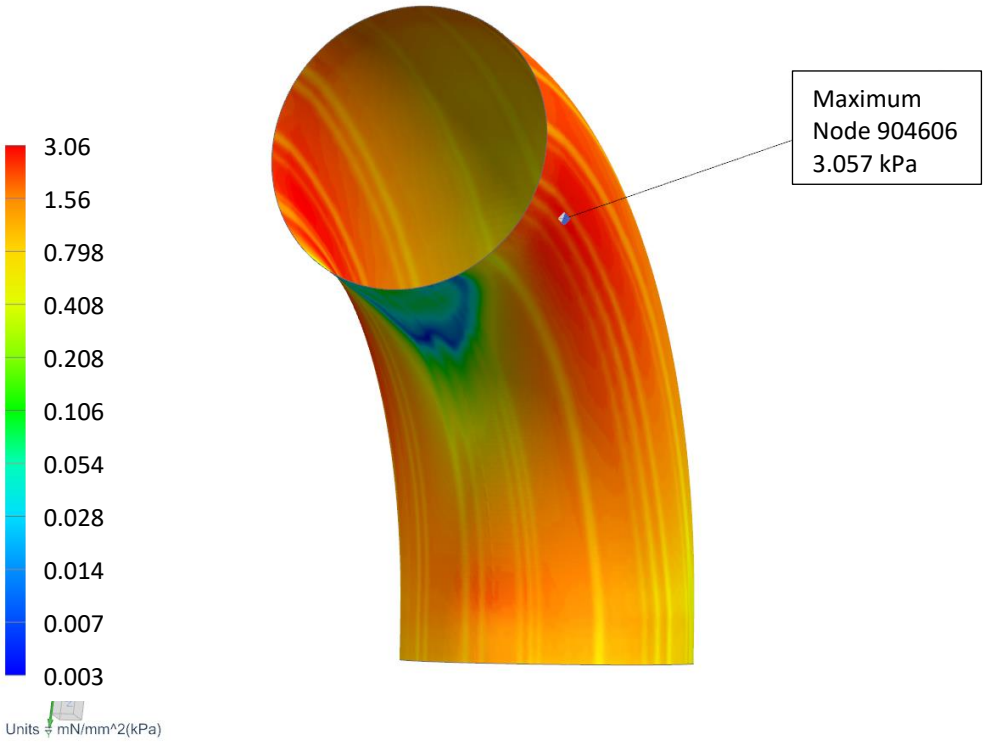

Figure 13: Shear stress distribution in a light water body that is flowing through B1

3.8 Boundary Conditions

The CFD analysis is performed only for a specific section of the PHT circuit rather than modeling the entire fluid flow. Therefore, the introduction of proper boundary conditions for the study is important towards the accurate results.

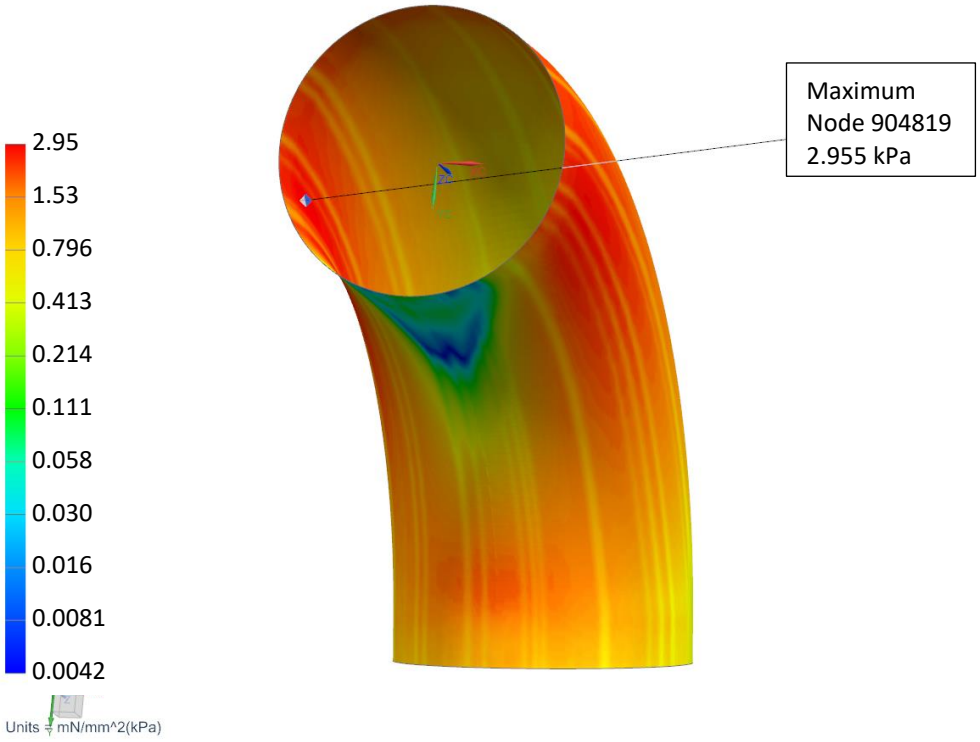

Figure 14: Shear stress distribution in a heavy water body that is flowing through B1

When the fluid enters a circular pipe with a uniform velocity, the fluid particles in the layer which is in contact with the surface of the pipe come to a complete stop. This is due to the friction incurred on the fluid from the pipe wall and this also causes the fluid particles in the adjacent layers to slow down gradually as a result of friction in between fluid particles. Since there is a reduction in the flow velocity close to the pipe wall, the flow velocity of the fluid at the middle of the pipe has to increase in order to keep the mass flow rate through the pipe as a constant. As a result of this phenomenon, a velocity gradient develops along the pipe.

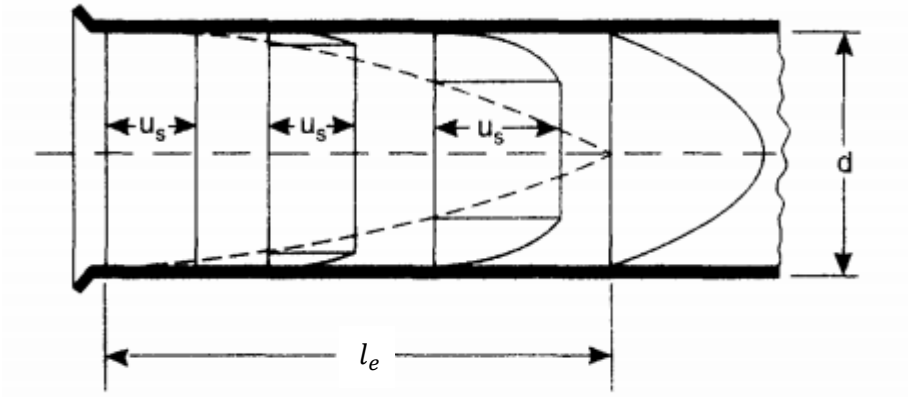

Figure 15: The development of the velocity boundary layer in a pipe [54]

The development of the velocity profile should be taken into consideration when introducing the boundary conditions to the CFD analysis. The entry length can be expressed by using the dimensionless Entrance Length Number as follows.

$$El = {}^{l_e}/_{d} \tag{17}$$

Where: El – Entrance length number

l_e – Length to fully developed velocity profile

d – Pipe diameter

The Entrance Length Number for turbulent flow is given by;

$$El_{Turbulent} = 4.4\, Re^{1/6} \tag{18}$$ [38]

Considering the study, the first bend (B1) of the outlet feeder pipe that is close to the grayloc hub is the segment of interest for the CFD analysis. Since the CAD model includes the end fitting segment (E1-E3) with a significant length upstream to the bend B1, it will mitigate the effect of the inlet flow profile due to the turbulence induced by the fuel bundles inside the pressure tube. Therefore, it is possible to introduce the inlet boundary condition as a uniform flow of heavy water with the corresponding flow rate. The straight segment of the geometry that is upstream from the grayloc hub is sufficient to let the inlet flow to become fully developed before it passes through the grayloc hub and first bend. This is further proven by changing the inlet flow profile from uniform to parabolic and

observing the same shear stress distribution. The maximum shear stress value recorded under both boundary conditions was 1.47 kPa. (Figure 16 and Figure 17 below). Similarly, the significant straight pipe segment at downstream to the second bend (L3) mitigates any effects on B1 due to the uniform outlet boundary condition.

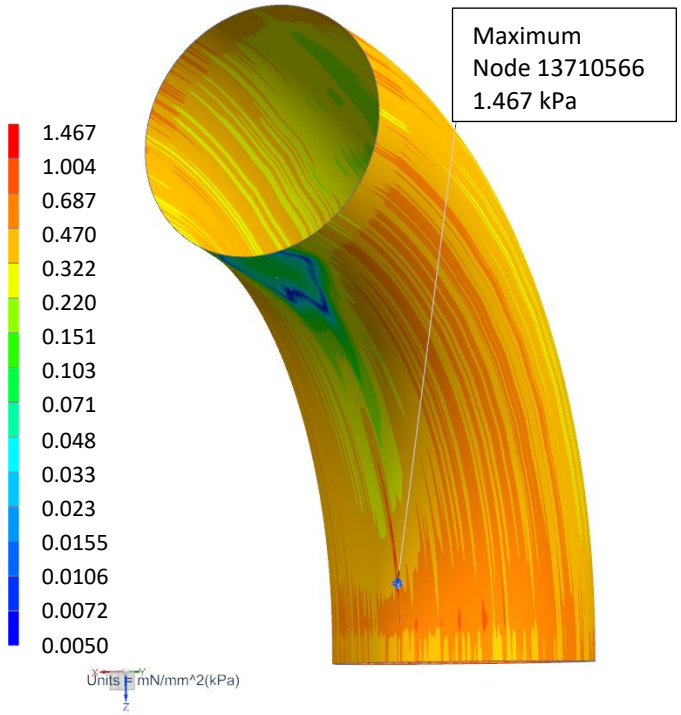

Figure 16: Wall shear stress distribution (Uniform flow inlet profile)

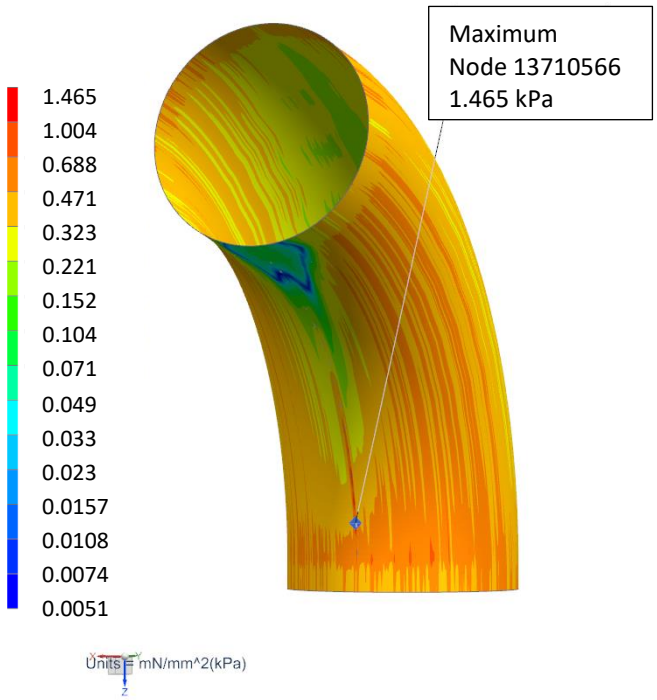

Figure 17: Wall shear stress distribution (Parabolic flow inlet profile)

3.9 Wall Roughness

Wall roughness is another parameter to be defined in order to perform an accurate CFD analysis. Even though the wall roughness is not uniform all over the pipe surface, it is assumed as uniformly distributed to reduce the complexity of the analysis. Outlet feeder pipes are made from carbon steel and the wall roughness for used and cleaned carbon steel pipes is in the range of 0.15 mm to 0.2 mm [39], [40]. Therefore, the wall roughness was assumed to be 0.15 mm for this CFD study.

3.10 Convergence and Mesh Sensitivity Analysis

Steady state simulation should ensure that the solution satisfies the following three conditions [41].

i. Residual Root Mean Square (RMS) Error values should reduce to an acceptable value (typically 10^{-4} or 10^{-5})
ii. Values of interest have reached a steady solution
iii. The domain has residual imbalances of less than 1%

The objective of the CFD analysis is to determine the maximum wall shear stress at the first bend (B1) geometry. Since it is important to generate a reliable mesh for B1, a set of 10 different mesh models were considered.

Table 4: Ten different mesh models considered for the study

	Mesh models									
	A	B	C	D	E	F	G	H	I	J
E1 – Mesh size (mm)	15	15	15	15	15	15	10	20	15	15
E2 – Mesh size (mm)	05	05	05	05	05	05	05	10	05	05
E3 – Mesh size (mm)	05	05	05	05	05	05	2.5	05	05	05
B1 – Source element size (mm)	1.5	1.0	0.75	0.1	0.5	0.25	0.25	0.25	0.25	0.25
L3 – Source element size (mm)	2.5	2.5	2.5	2.5	2.5	2.5	2.5	2.5	05	01

According to the convergence summary in Table 5, it is evident that the mesh model D – J are satisfying all three conditions concluding the convergence of the CFD analysis.

Table 5: Convergence summary for different mesh models

Mesh Model	Residual RMS Error less than 10^{-4}	Steady state solution	Domain imbalance less than 1%
A	YES	NO	NO
B	YES	NO	YES
C	YES	NO	YES
D	YES	YES	YES
E	YES	YES	YES
F	YES	YES	YES
G	YES	YES	YES
H	YES	YES	YES
I	YES	YES	YES
J	YES	YES	YES

Please refer APPENDIX - D for residual RMS error and steady state solution plots.

In order to determine the optimum mesh model, an analysis was performed to investigate the sensitivity of simulation predictions on the computational mesh according to the guidelines from The American Society of Mechanical Engineers (ASME) for numerical verifications for CFD simulations as outlined in [42]. This method has been used in support of safety analyses of fuel bundle in a nuclear reactor by M.H.A. Piro and B.W. Leitch [43].

During the mesh sensitivity analysis, all the other factors such as flow boundary conditions, material properties, and solver details remained constant. The K-Omega turbulent model was used throughout the analysis. Moreover, all three mesh models (D, E, and F) used a combination of tetrahedral and triangular prism mesh in the same regions in the domain.

Maximum wall shear stress and the maximum fluid pressure in the B1 segment were used as the parameters of interest for the analysis.

A similar analysis was performed for the mesh models F, G and H as well as mesh models F, I and J to find the optimum mesh model for the segments E1-E3 and L3 respectively. A summary of the parameters used in computing the estimated discretization errors is provided in Table 8.

Table 6 summarizes the details of mesh sizes used in different segments of the geometry as well as the number of elements.

Procedure:

Step 01: Define a representative cell size *h*

$$h = \left[\frac{1}{N}\sum_{i=1}^{N}(\Delta v_i)\right]^{1/3} \tag{19}$$

Step 02: Evaluate the grid refinement factor *r*

$$r = \frac{h_{coarse}}{h_{fine}} \tag{20}$$

Step 03: Calculate the apparent order *p*

$$p = \frac{1}{ln|r_{21}|}\left|ln\left|{\varepsilon_{32}}/{\varepsilon_{21}}\right| + q(p)\right| \tag{21}$$

where;

$$r_{21} = {h_2}/{h_1} \tag{22}$$

$$\varepsilon_{32} = (\phi_3 - \phi_2) \tag{23}$$

$$\varepsilon_{21} = (\phi_2 - \phi_1) \tag{24}$$

Step 04: Calculate the extrapolated values from

$$\phi_{ext}^{21} = ({r_{21}}^p \phi_1 - \phi_2)/({r_{21}}^p - 1) \tag{25}$$

Similarly, calculate ϕ_{ext}^{32}

Step 05:

Relative error

$$e_a^{21} = \left|\frac{\phi_1 - \phi_2}{\phi_1}\right| \quad (26)$$

Extrapolated relative error

$$e_{ext}^{21} = \left|\frac{\phi_{ext}^{21} - \phi_1}{\phi_{ext}^{21}}\right| \quad (27)$$

Grid Convergence Index

$$GCI_{fine}^{21} = \frac{1.25 e_a^{21}}{{r_{21}}^p - 1} \quad (28)$$

A summary of the parameters used in computing the estimated discretization errors is provided in Table 7. Approximate relative error as well as the Grid Conversion Index (GCI) implies that the mesh model E is inadequate for this type of analysis. However, the results between mesh model F and mesh model D are quite comparable with low computed numerical errors concludes the mesh resolution of model F is sufficient for the study while the mesh model D provides unnecessarily high resolution.

Table 6: Summary of different mesh models for L1-B2

	Mesh models for L1-B2		
	D	E	F
E1 – Mesh size (mm)	15	15	15
E2 – Mesh size (mm)	5	5	5
E3 – Mesh size (mm)	5	5	5
B1 – Source element size (mm)	0.1	0.5	0.25
L3 – Source element size (mm)	2.5	2.5	2.5
Momentum imbalance (%)	0.0010	0.0011	0.0012
Solution time (Hours)	16.9	18.6	13.2
Number of elements (million)	12.8	11.1	12.4
Refinement Factor	1.0085	-	1.0398

Table 7: Summary of mesh sensitivity analysis for L1-B2

	ϕ = Max. wall shear stress	ϕ = Max. fluid Pressure
ϕ_D	6.53 kPa	1.16E+04 kPa
ϕ_E	4.68 kPa	1.30E+04 kPa
ϕ_F	6.29 kPa	1.18E+04 kPa
Apparent order (p)	55.83	50.11
Approximate relative error e_a^{EF}	25.6%	9.9%
Approximate relative error e_a^{FD}	3.8%	1.9%
Extrapolated relative error e_{ext}^{EF}	3.2%	1.7%
Extrapolated relative error e_{ext}^{FD}	0.7%	0.4%
Grid convergence index GCI_{EF}	4.1%	2.0%
Grid convergence index GCI_{FD}	0.9%	0.5%

Table 8: Summary of different mesh models for E1-E3

	Mesh models for E1-E3		
	F	G	H
E1 – Mesh size (mm)	15	10	20
E2 – Mesh size (mm)	5	5	10
E3 – Mesh size (mm)	5	2.5	5
B1 – Source element size (mm)	0.25	0.25	0.25
L3 – Source element size (mm)	2.5	2.5	2.5
Momentum imbalance (%)	0.0012	0.0010	0.0058
Solution time (Hrs)	13.2	18.5	11.3
Number of elements (million)	12.4	18.8	10.1
Refinement Factor	1.0709	1.1477	-

Table 9: Summary of different mesh models for L3

	Mesh models for L3		
	F	I	J
E1 – Mesh size (mm)	15	15	15
E2 – Mesh size (mm)	5	5	5
E3 – Mesh size (mm)	5	5	5
B1 – Source element size (mm)	0.25	0.25	0.25
L3 – Source element size (mm)	2.5	5	1
Momentum imbalance (%)	0.0012	0.0002	0.0018
Solution time (Hours)	13.2	12.4	15.1
Number of elements (million)	12.4	11.7	13.0
Refinement Factor	1.0206	-	1.0155

According to the results summarized in Table 10, it is evident that the approximate relative error, as well as the GCI, is higher with the mesh model H compared to mesh model F. This implies that more refinements should be done to the mesh model H for this type of a study. However, the GCI for the mesh model F compared to the mesh model G implies that the resolution of mesh model F is sufficient for this study. Therefore, mesh model F was selected over the mesh model G and mesh model H.

Table 10: Summary of mesh sensitivity analysis for E1-E3

	φ = Max. wall shear stress	φ = Max. fluid Pressure
ϕ_F	6.29 kPa	1.18E+04 kPa
ϕ_G	6.40 kPa	1.18E+04 kPa
ϕ_H	6.86 kPa	1.19E+04 kPa
Apparent order (*p*)	11.73	7.45
Approximate relative error e_a^{HF}	9.1%	0.7%
Approximate relative error e_a^{FG}	1.8%	0.2%
Extrapolated relative error e_{ext}^{HF}	7.9%	1.0%
Extrapolated relative error e_{ext}^{FG}	0.4%	0.1%
Grid convergence index GCI_{HF}	9.2%	1.3%
Grid convergence index GCI_{FG}	0.5%	0.2%

Similarly, the results summarized in

Table 11 imply that the mesh model F is more appropriate over the mesh model I for the purpose of this study. However, smaller GCI_{FJ} implies that the mesh model J has an unnecessarily high resolution. Therefore, mesh model F was selected over the mesh models I and J.

Table 11: Summary of mesh sensitivity analysis for L3

	ϕ = Max. wall shear stress	ϕ = Max. fluid Pressure
ϕ_F	6.29 kPa	1.18E+04 kPa
ϕ_I	5.13 kPa	1.07E+04 kPa
ϕ_J	6.42 kPa	1.19E+04 kPa
Apparent order (*p*)	137.99	175.24
Approximate relative error e_a^{IF}	18.3%	9.5%
Approximate relative error e_a^{FJ}	2.1%	0.6%
Extrapolated relative error e_{ext}^{IF}	1.2%	0.3%
Extrapolated relative error e_{ext}^{FJ}	0.3%	0.0%
Grid convergence index GCI_{IF}	1.5%	0.3%
Grid convergence index GCI_{FJ}	0.4%	0.1%

Table 12 below summarizes the mesh types and sizes used in different segments of the geometry that were concluded after performing the mesh sensitivity analysis.

Table 12: Different mesh types and Sizes used

Section	**Mesh Type**
E1	5 mm TRI3 surface mesh with 15 mm Tetrahedral mesh
E2	5 mm TRI3 surface mesh with 5 mm Tetrahedral mesh
E3	5 mm TRI3 surface mesh with 5 mm Tetrahedral mesh
L1	2D mesh (Figure 18) swept with 1 mm source element size
B1	2D mesh (Figure 18) swept with 0.25 mm source element size
L2	2D mesh (Figure 18) swept with 1 mm source element size
B2	2D mesh (Figure 18) swept with 1 mm source element size
L3	2D mesh (Figure 18) swept with 2.5 mm source element size

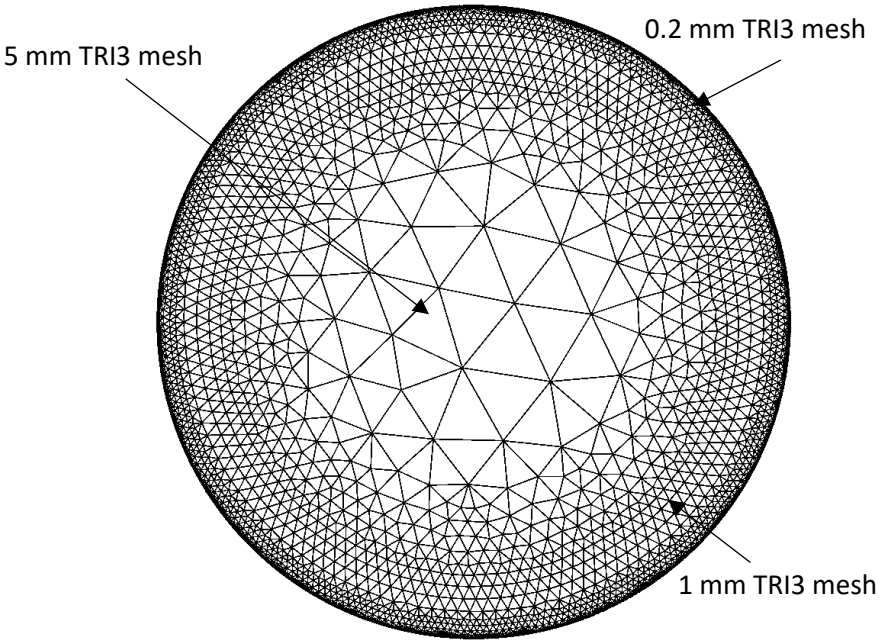

Figure 18: Defined mesh arrangement

4 RESULTS & DISCUSSION

It is evident that a lot of previous studies have been performed relating the fluid flow velocity with mass transfer coefficient and rate of wall thinning in CANDU outlet feeder pipes [7], [29]. This study is focused on developing a model that can predict the maximum wall shear stress at bend B1 and then observe the behaviour of wall shear stress against the rate of wall thinning. Fluid flow velocity is closely related to the wall shear stress and therefore, the distribution of both velocity and the wall shear stress are important.

4.1 Wall Shear Stress and Velocity Distribution

Different types of feeder pipes that belong to the unit 1 of the Darlington Nuclear Generating Station were modeled using Siemens NX9.0. Figure 19 and Figure 20 below show the CFD results on the distribution of the wall shear stress and the fluid flow velocity at B1 for the feeder type L3 that is corresponding to channel S09E of unit 1.

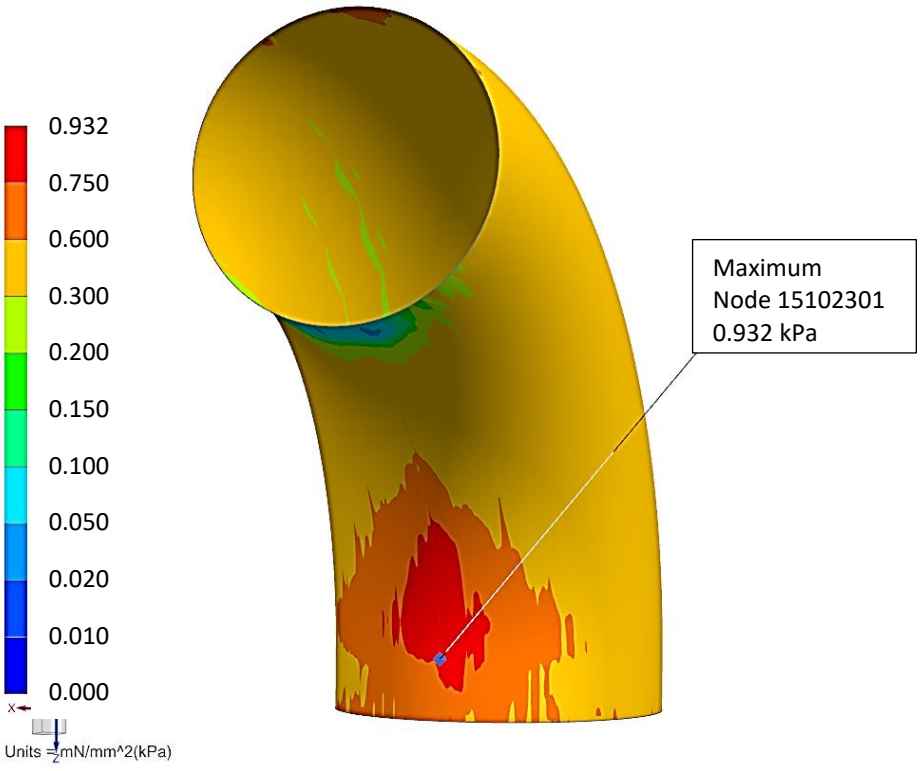

Figure 19: CFD results on distribution of wall shear stress

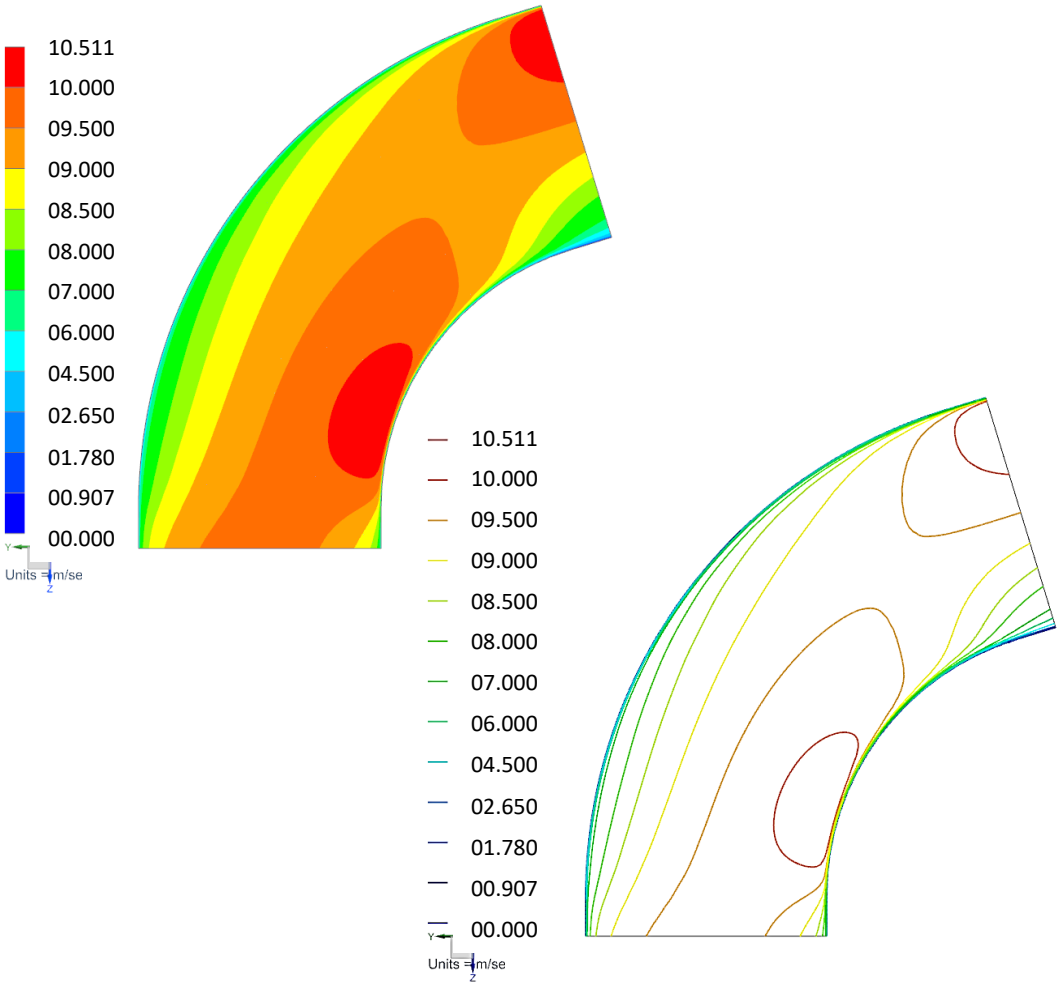

Figure 20: CFD results on distribution of fluid velocity (m/s)

According to the Figure 19, it is possible to see that the maximum wall shear stress is recorded on the intrados of the bend (B1 geometry). Furthermore, Figure 20 proves that the wall shear stress is well related to the variation of fluid flow velocity close to the feeder pipe wall.

Similarly, the wall shear stress and fluid flow velocity distribution at B1 were observed for a set of different types of feeders covering the unit 1 of Darlington Nuclear Generating Station. Design and operating parameters along with the maximum wall shear stress recorded for the B1 segment (τ_{Max}) are summarized in Table 13.

Table 13: Design and operation parameters of different bend types and maximum wall shear stress from CFD analysis

Bend Type	Size (mm)	L_1(mm)	θ_1 (°)	L_1/θ_1	Mass F/R (kg/s)	Reynolds Number	τ_{Max} (kPa)
A	49.3	45.5	40.8	1.12	16.04	5.56E+06	0.399
B	49.3	38.6	48.0	0.80	18.98	6.08E+06	0.577
D	49.3	10.4	73.0	0.14	18.64	6.34E+06	1.058
G1	49.3	10.4	73.0	0.14	17.29	5.92E+06	0.905
I	49.3	10.4	73.0	0.14	13.45	4.96E+06	0.402
K1	49.3	10.4	73.1	0.14	16.14	5.68E+06	0.723
K2	49.3	10.4	73.1	0.14	19.40	6.34E+06	1.277
K3	49.3	10.4	73.1	0.14	14.21	6.27E+06	1.006
K4	49.3	10.4	73.1	0.14	15.25	5.28E+06	0.509
K5	49.3	10.4	73.1	0.14	16.57	5.73E+06	0.784
M	49.3	03.1	41.0	0.08	16.59	5.38E+06	0.688
C	59.0	43.5	48.0	0.91	17.00	6.83E+06	0.777
E	59.0	15.3	73.0	0.21	24.39	6.59E+06	0.814
H1	59.0	15.3	73.0	0.21	25.03	6.34E+06	0.743
J	59.0	15.3	73.0	0.21	27.63	6.91E+06	1.062
L1	59.0	15.3	73.1	0.21	27.03	6.69E+06	0.939
L2	59.0	15.3	73.1	0.21	27.97	6.95E+06	1.095
L3	59.0	15.3	73.1	0.21	27.49	7.04E+06	0.932
L4	59.0	15.3	73.1	0.21	27.80	6.95E+06	1.093
L5	59.0	15.3	73.1	0.21	27.89	6.95E+06	1.095
L6	59.0	15.3	73.1	0.21	27.61	6.96E+06	1.098

4.2 Predicting the maximum wall shear stress in B1

Figure 21 below explains the relationship between fluid Reynolds number and the maximum wall shear stress of B1 while the Figure 22 below illustrates the relationship between the ratio (L_1/θ_1) and the maximum wall shear stress of B1.

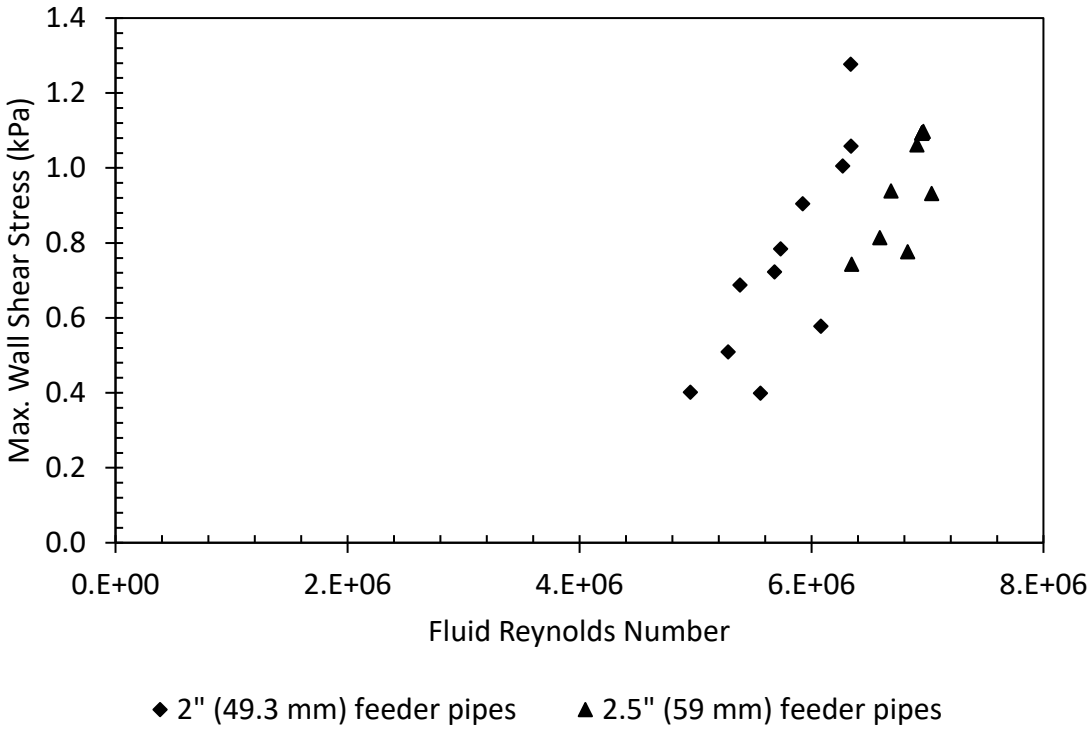

Figure 21: Variation of maximum wall shear stress with respect to fluid Reynolds number for 2" and 2.5" feeder pipes

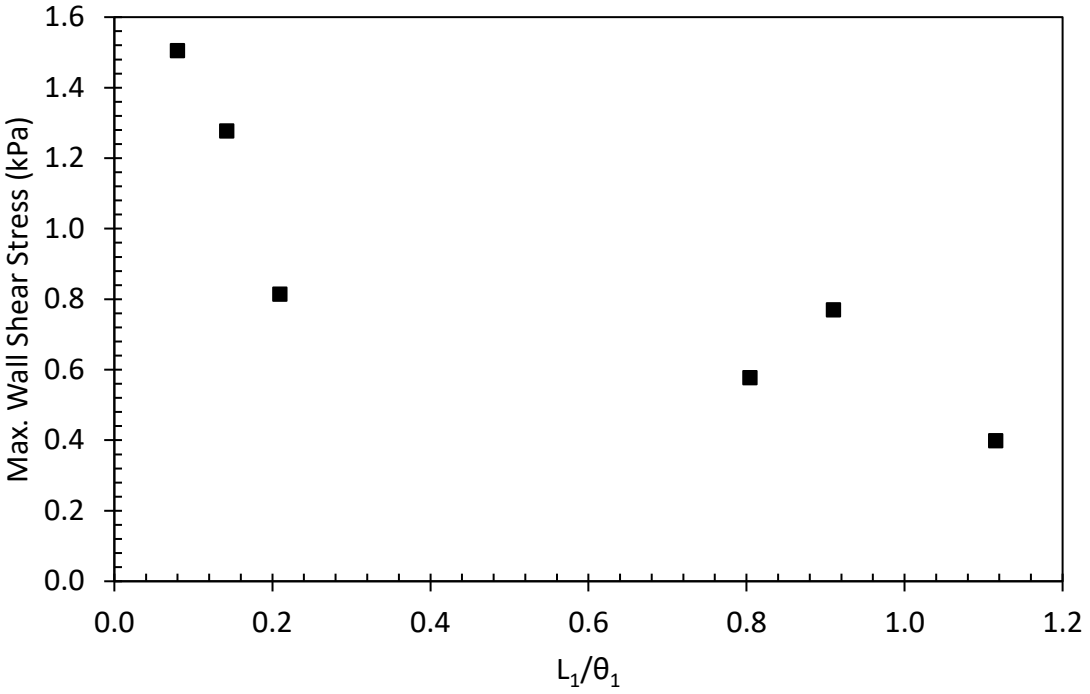

Figure 22: Variation of maximum wall shear stress with respect to the ratio of L_1/θ_1

MATLAB was used to prepare a 3D plot using the CFD data summarized Table 13 above, taking fluid Reynolds number and (L_1/θ_1) as independent variables while the maximum wall shear stress at B1 (τ_{Max}) as the dependent variable. A surface was then created such that it fits with the data points and the following relationships were achieved.

$\tau_{Max} = Re^{0.178} - 15.48 \times \left(L_1/\theta_1\right)^{0.012}$ for 2" feeder pipes

$\tau_{Max} = Re^{0.183} - 17 \times \left(L_1/\theta_1\right)^{-0.009}$ for 2.5" feeder pipes

4.3 Benchmarking the model

Jong Chull Jo et al. have performed numerical calculations to determine the shear stress distribution on the inner wall surface of CANDU reactor feeder pipes. The predictive model developed in this study was compared against the results that the authors have published in [44]. Figure 23 and Figure 24 shows that the predicted wall shear stress values under similar design and operating conditions as outlined in [44] and the literature values are aligned with a tolerance of less than 10%.

Moreover, the CFD analysis of this study shows the maximum wall shear stress value at the intrados of the B1 that is also concluded by Jong Chull Jo et al. in their study [44]. When considering the literature as outlined in [8], [9], it is evident that the maximum rate of wall thinning is also recorded at the intrados of the first bend from the grayloc hub in CANDU outlet feeder pipes. This study agrees with the literature by observing the maximum wall shear stress at the intrados of the first bend during the CFD analysis.

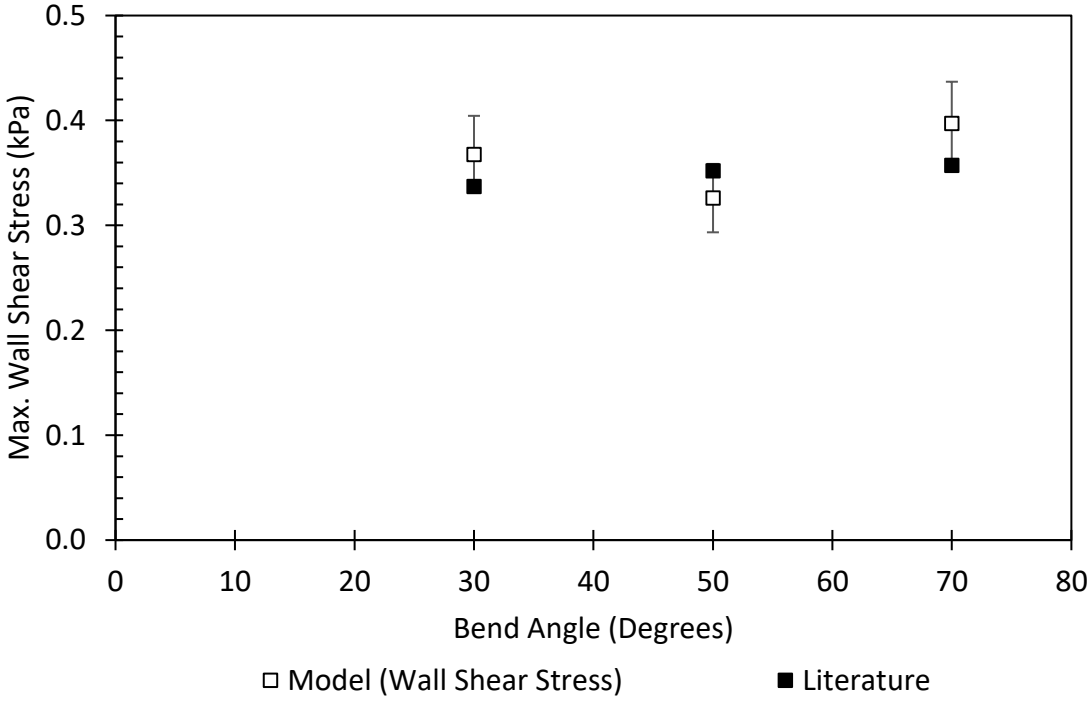

Figure 23: Comparison of Max. Wall shear stress from predictive model against the literature [43] at different bend angles

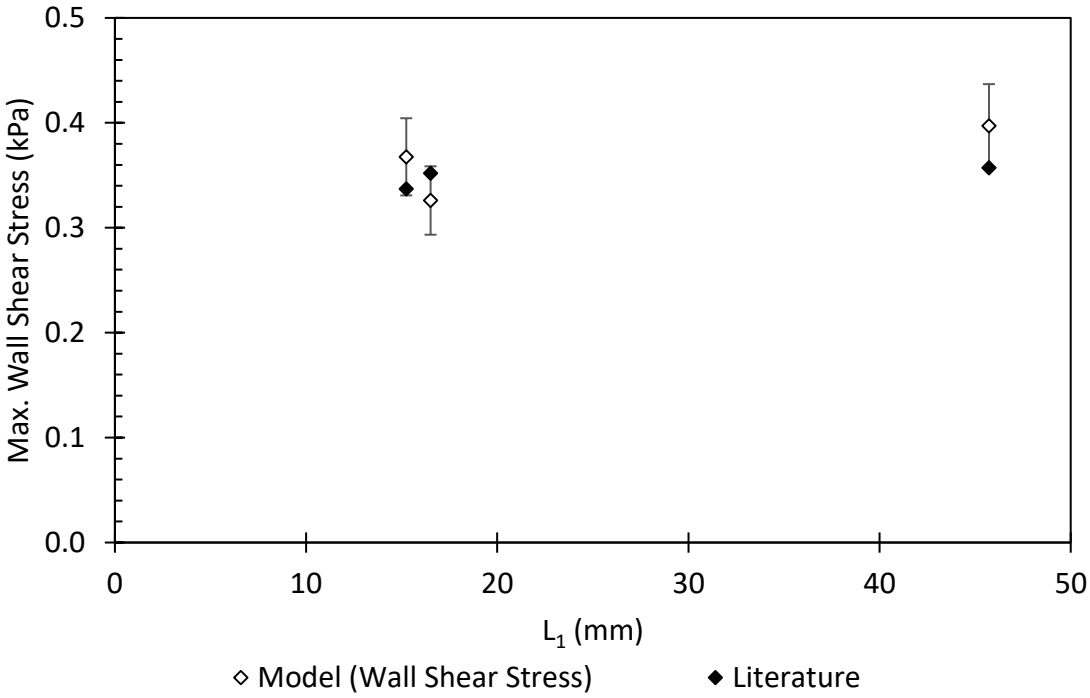

Figure 24: Comparison of Max. Wall shear stress from predictive model against the literature [43] at different lengths L_1

4.4 Limitations of the model

The predictive model developed during this study has some limitations that could not be overcome due to the restrictions on time and resources as well as considering the complexity of the study.

Since this study is basically focused on predicting the wall shear stress at Unit 1 of the Darlington Nuclear Generating Station, the predictive model was only developed for 2" and 2.5" diameter (nominal) feeder pipes. The predictive model is comprised of two different equations considering the feeder pipe diameters. The applicability of the model towards other feeder pipe diameters is to be further investigated.

The predictive model was developed considering the range of fluid Reynolds number that is applicable to unit 1 of the Darlington Nuclear Generating Station. The applicability of the model outside this region is to be further studied.

Since the maximum wall thinning rate was observed in the first bend of the outlet feeder pipe [8], [9], the study was focused on predicting the wall shear stress at the first bend (B1). Therefore, further work should be done to predict the wall shear stress distribution with the rest of the pipe geometries.

4.5 Analogy between wall shear stress and the rate of wall thinning

Wall thinning of the outlet feeder pipes is one of the major challenges in the nuclear power industry. A lot of research work is carried out in this area to figure out the potential mechanisms, and still, there are some difficulties when it comes to forecasting the rate of wall thinning.

The wall thinning process in CANDU outlet feeder pipes has resulted from a series of consecutive events [7]. The pH level of the heavy water, metal debris suspended in heavy water, wall shear stress distribution and fluid temperature are among the parameters of interest towards determining the rate of wall thinning. When considering those parameters, most of them are common in all feeder pipe geometries except the wall shear stress distribution that is changing with the physical arrangement of the feeder pipe (i.e. bend angle and pipe diameter).

When considering the lifetime estimation, the wall shear stress distribution is therefore crucial and would have a greater impact on the other parameters. Feeder pipes with a higher value of wall shear stress, would likely to have a higher rate of wall thinning. The wall shear stress distribution was compared against feeder pipe wall thinning data available for the unit 1 of the Darlington Nuclear Generating Station as well as from the literature.

The unit 1 of the Darlington Nuclear Generating Station is a 480-channel nuclear reactor that is having outlet feeder pipes with 2” and 2.5” nominal diameter. The wall shear stress model was used to predict the maximum wall shear stress in each feeder pipe and compared against the rate of wall thinning data received from Ontario Power Generation.

According to the Figure 26 and Figure 25, it is possible to observe a trend between the predicted wall shear stress values and the rate of wall thinning data available.

The rate of wall thinning (mm/FPY) data in Figure 26 and Figure 25 from Darlington Nuclear Generating Station is based on the fluid flow velocity through the feeder pipe. However, the wall shear stress model predicts based on fluid Reynolds number, bend angle as well as the distance between grayloc hub and the first bend. Therefore, it is possible to observe multiple wall shear stress values for the same fluid flow velocity (i.e. for the same Reynolds number) in Figure 26 and Figure 25.

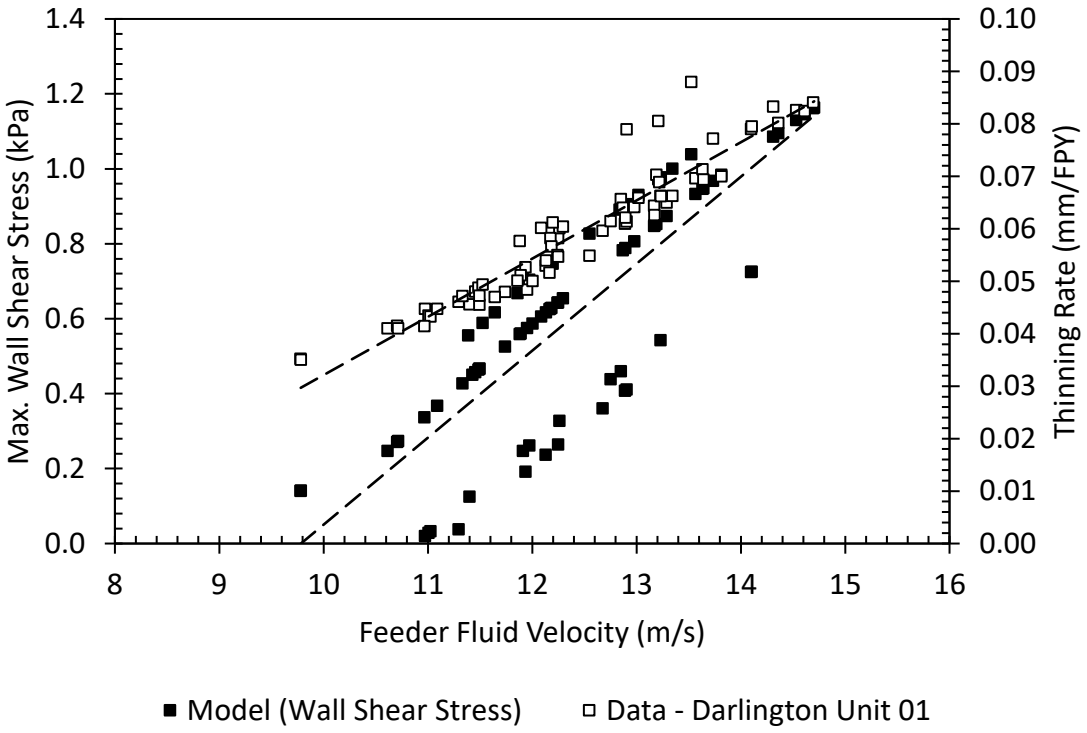

Figure 25: Comparison of wall shear stress against the rate of wall thinning data available (2" feeder pipes) from Darlington Nuclear Generating Station

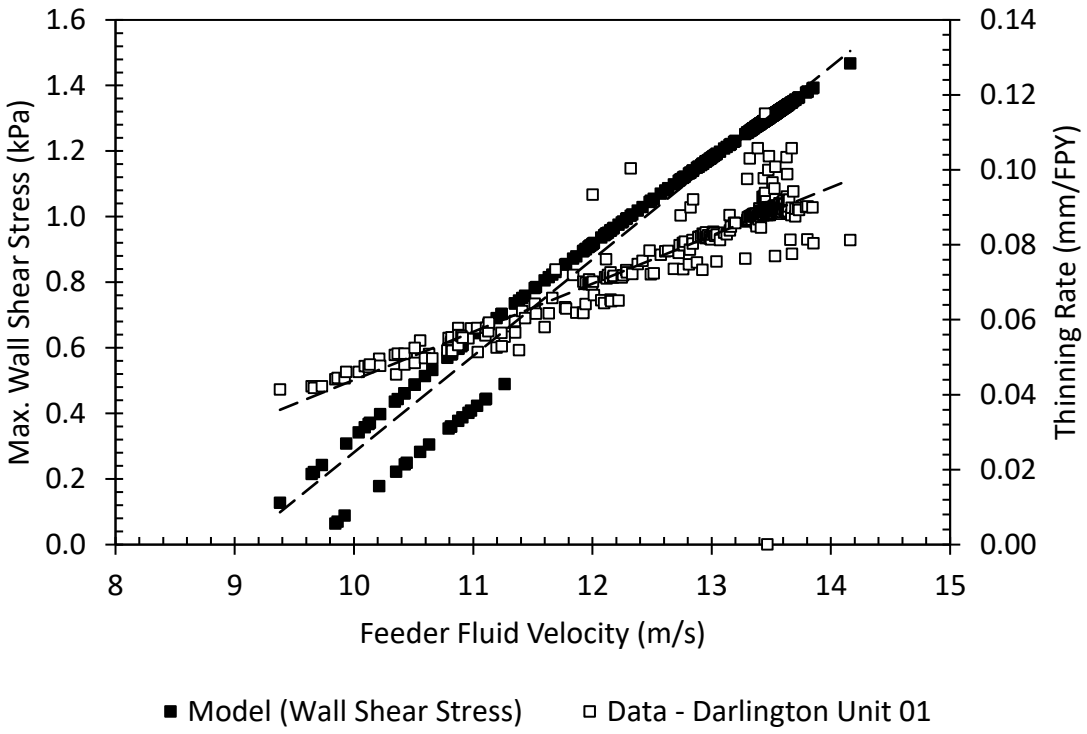

Figure 26: Comparison of wall shear stress against the rate of wall thinning data available (2.5" feeder pipes) from Darlington Nuclear Generating Station

D.H. Lister et al. from the University of New Brunswick has developed a relationship between fluid flow velocity and the rate of wall thinning (mm/FPY) at outlet feeder pipes. The relationship is further simplified to express as;

$$Thinning\ rate = (0.00174 \times Velocity^{1.52}) + 0.00559 \quad (29)\ [7]$$

Wall shear stress data generated from the developed predictive model was compared against the rate of wall thinning from the model that is developed by D.H Lister et al. considering the feeder pipe geometries in unit 1 of Darlington Nuclear Generating Station. According to the Figure 28 and Figure 27 below, it is possible to observe a trend between the variation of wall shear stress and the rate of wall thinning. However, it is not possible to simply correlate these two parameters without studying the phenomena in greater detail.

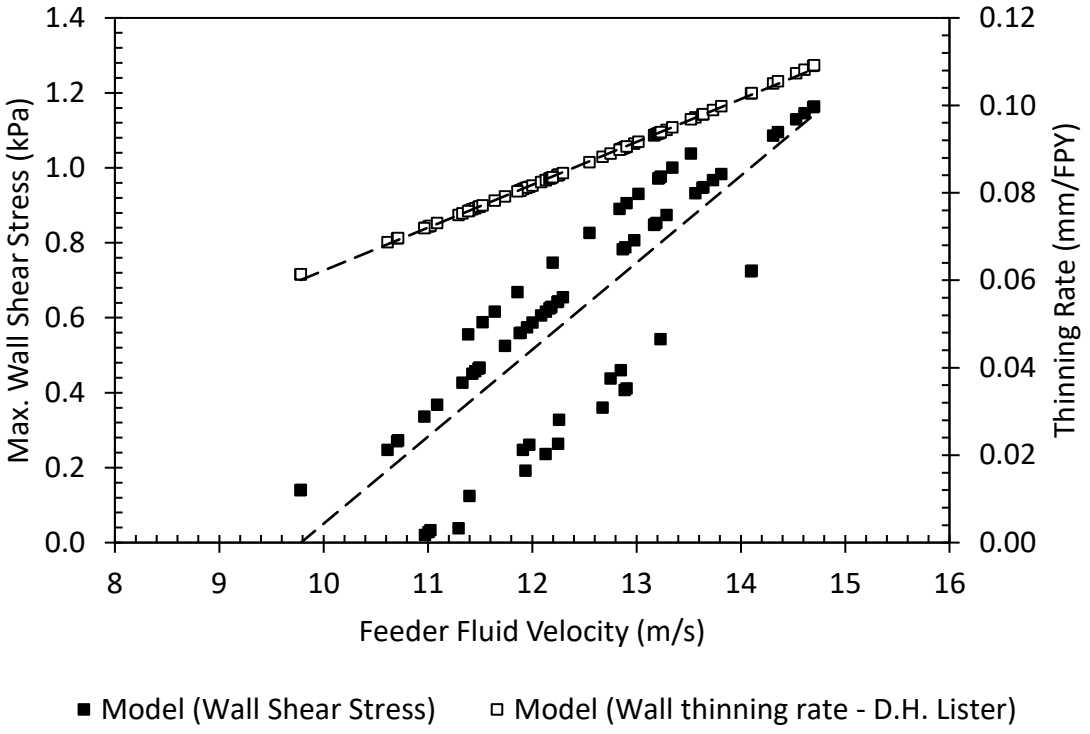

Figure 28: Comparison of wall shear stress against the rate of wall thinning from the model developed by D.H Lister et al. [7] (2" feeder pipes)

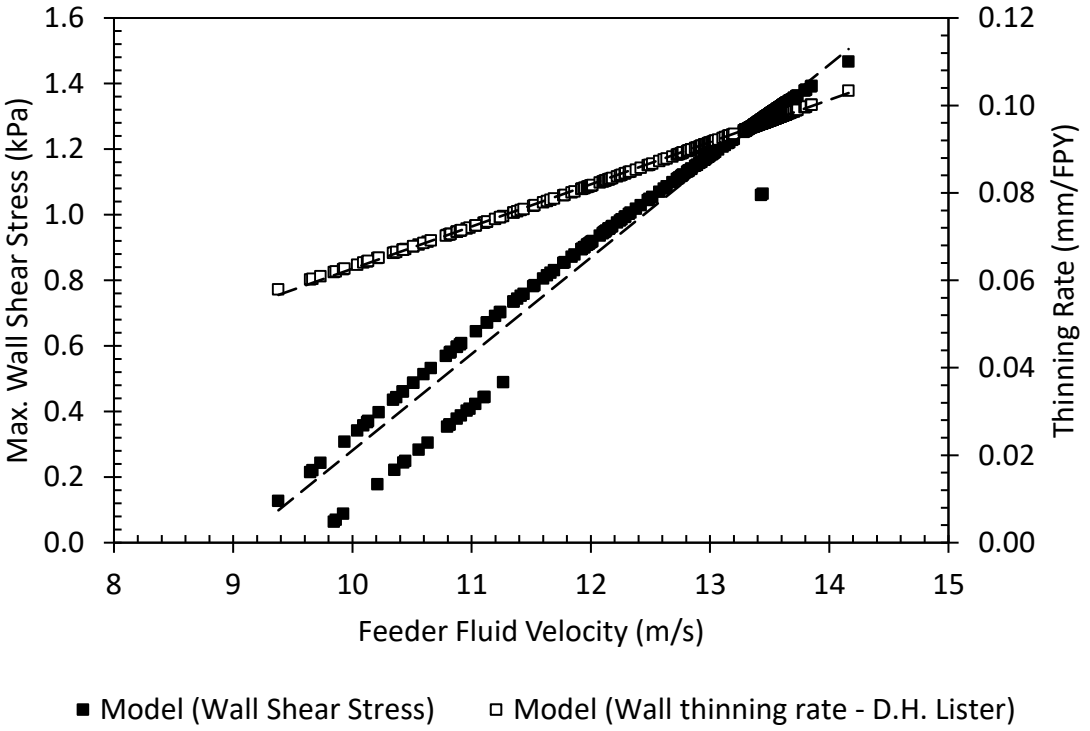

Figure 27: Comparison of wall shear stress against the rate of wall thinning from the model developed by D.H Lister et al. [7] (2.5" feeder pipes)

Moreover, D.H. Lister et al. have derived the following expression to represent the rate of wall loss in outlet feeder pipes based on a comprehensive corrosion chemistry and mass transfer theory [29].

$$\dot{m} = \frac{k_m \cdot k_d}{(0.5k_m + k_d)}(C_{sat} - C_b) \quad (30)$$

Where

$\dot{m}$	Rate of wall loss,
k_m	Mass transfer coefficient,
k_d	Magnetite dissolution kinetic constant,
C_{sat}	Iron saturation concentration,
C_b	Iron concentration in bulk coolant.

According to the Figure 6 saturation and bulk concentration for Fe ions (C_{sat} andC_b) are 9.75 and 7.5 µg/kg of heavy water respectively. Mass transfer coefficient and Magnetite dissolution kinetic constant were calculated according to the method available in [45]. Figure 29 and Figure 30 compare the wall shear stress predicted from the model against the rate of wall thinning data based on the equation above. It is also possible to observe a trend between the variation of wall shear stress and the rate of wall thinning.

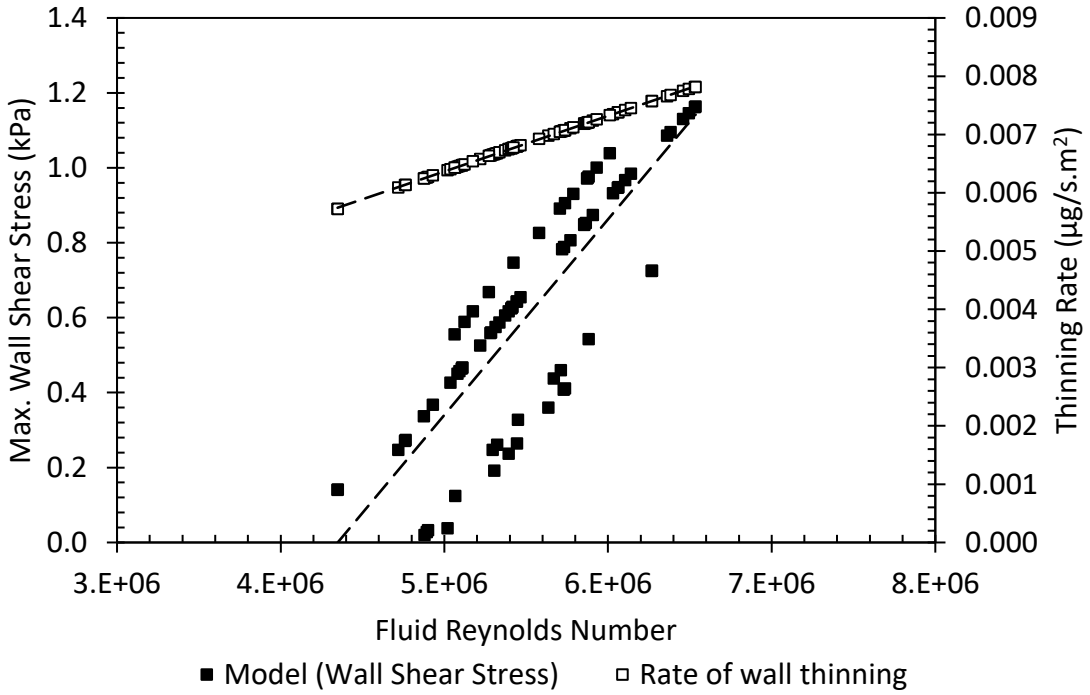

Figure 29: Comparison of wall shear stress against the rate of wall thinning from the [29] (2" feeder pipes)

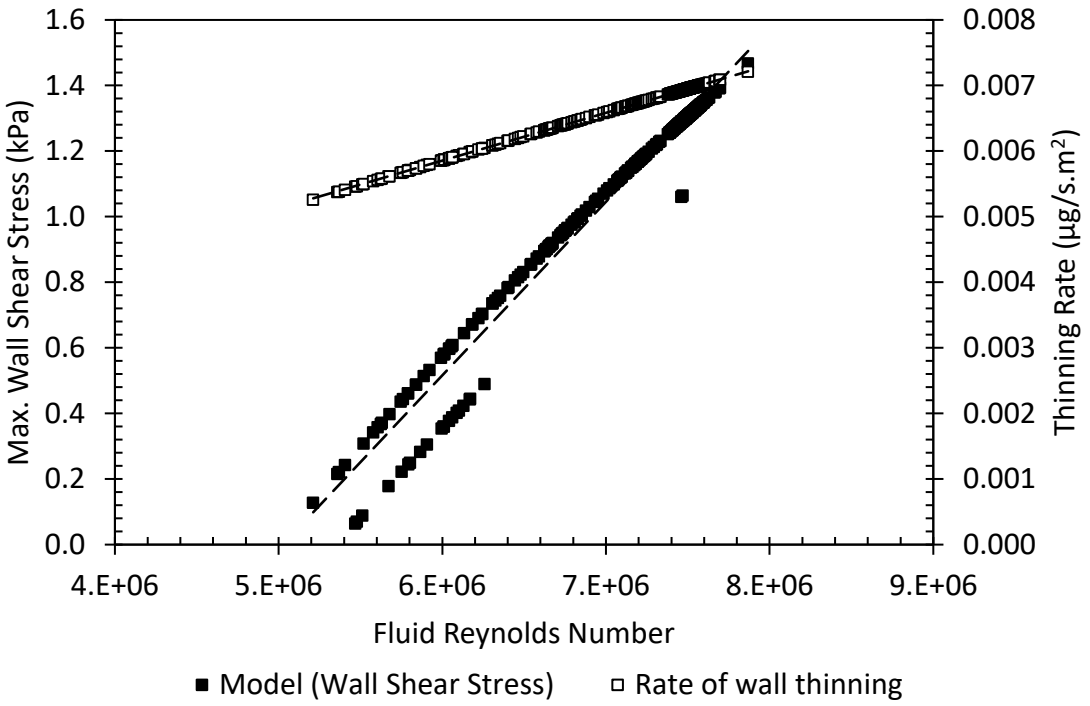

Figure 30: Comparison of wall shear stress against the rate of wall thinning from the [29] (2.5" feeder pipes)

5 CONCLUSIONS

Siemens NX was used to perform CFD analysis to determine the wall shear stress distribution at the 1st bend of the outlet feeder pipe geometry. Twenty-one different types of feeder pipes corresponding to unit 1 of the Darlington Nuclear Generating Station were modeled and analyzed to determine the wall shear stress. Based on the CFD results, a predictive model was developed to forecast the maximum wall shear stress at the 1st bend of the feeder pipe in terms of fluid Reynolds number, bend angle and the linear length between the grayloc hub and 1st bend.

$$\tau_{Max} = Re^{0.178} - 15.48 \times \left({L_1}/{\theta_1}\right)^{0.012} \qquad \text{for 2" feeder pipes}$$

$$\tau_{Max} = Re^{0.183} - 17 \times \left({L_1}/{\theta_1}\right)^{-0.009} \qquad \text{for 2.5" feeder pipes}$$

Maximum wall shear stress values predicted from the model were compared against the literature values published by Jong Chull Jo et al. The predictive model is a good fit with the literature with a tolerance of less than 10%.

The predictive model was used to calculate the maximum wall shear stress for all the outlet feeder pipes corresponding to unit 1 of the Darlington Nuclear Generating Station. The wall shear stress values were then compared against the rate of wall thinning data available from OPG. The wall shear stress values predicted by the model show a good trend with the rate of wall thinning values received from OPG. However, further studies need to be done to improve the predictive model so that it can predict the rate of wall thinning.

Moreover, the wall shear stress values predicted from the model were compared against the rate of wall thinning data generated from two different predictive models available in the literature. In both of the scenarios, predicted wall shear stress data was in a good trend with the rate of wall thinning data.

6 RECOMMENDATIONS

The current model only predicts the maximum wall shear stress value at the first bend geometry of the feeder pipe based on the fluid Reynolds number, bend angle and the linear length between the grayloc hub and the first bend. Predicting wall shear stress is crucial to estimating the life of feeder pipes, and there are several other factors affecting the rate of wall thinning under FAC. Therefore, further studies need to be done to improve the predictive model so that it can predict the rate of wall thinning of all CANDU outlet feeder pipes.

During this study, a predictive model was developed based on the design details of unit 1 of the Darlington Nuclear Generating Station. Therefore, the model can predict wall shear stress values only for feeder pipes with 2” and 2.5” in nominal diameter. Further studies need to be done to extend the applicability of the model to include different pipe diameter values. Similarly, the predictive model was developed for a certain range of fluid Reynolds number. Further studies need to be done to determine the applicability of the model outside the above range.

The study was focused on predicting the wall shear stress only at the first bend (B1) considering the complexity and limitation of the computational resources when modeling the entire outlet feeder pipe geometry. Therefore, further work should be done to predict the wall shear stress distribution for the rest of the pipe geometries.

7 REFERENCES

[1] I. Pioro and P. Kirillov, "Generation IV Nuclear Reactors as a Basis for Future Electricity Production in the World," *Materials and process for energy: communicating current research and technological developments,* pp. 818 - 830, 2013.

[2] "World Statistics, Nuclear Energy Around the World," Nuclear Energy Institute, [Online]. Available: http://www.nei.org/Knowledge-Center/Nuclear-Statistics/World-Statistics. [Accessed 18 08 2016].

[3] G. Bereznai, "Chapter 4: Heat Transport," in *CANDU Overview*.

[4] "Heat Transport System," January 1996. [Online]. Available: https://canteach.candu.org/Content%20Library/19930204.pdf. [Accessed 17 11 2016].

[5] "CANDU 6 Technical Summary," CANDU 6 Program Team - Reactor Development Business Unit, May 2005.

[6] "Darlington Nuclear," Ontario Power Generation, [Online]. Available: https://www.opg.com/generating-power/nuclear/stations/darlington-nuclear/Pages/darlington-nuclear.aspx. [Accessed 2017].

[7] D. H. Lister, J. Slade and N. Arbeau, "The accelerated corrosion of CANDU outlet feeders - observations, possible mechanisms and potential remedies," Fredericton, N.B..

[8] H.-S. Chung, "A review of candu feeder wall thinning," *Nuclear Engineering and Technology,* vol. 42, no. 5, pp. 568-575, 2010.

[9] J. Singh, U. Kumar, N. Kumawat, S. Kumar, V. Kain, S. Anantharaman and A. Sinha, "Flow accelerated corrosion of carbon steel feeder pipes from pressurized," *Journal of Nuclear Materials,* vol. 429, p. 226–232, 2012.

[10] "Fuel comparison," European Nuclear Society, [Online]. Available: https://www.euronuclear.org/info/encyclopedia/f/fuelcomparison.htm. [Accessed 18 10 2016].

[11] Johnzactruba, "Burning Coal in Power Plants – Calorific Value and Moisture," Bright Hub Engineering, 20 10 2009. [Online]. Available: http://www.brighthubengineering.com/power-plants/22202-burning-coal-in-power-plants-calorific-value-and-moisture/. [Accessed 12 01 2018].

[12] "The Economic Benefits of Refurbishing and Operating Ontario's Nuclear Reactors," Canadian Manufacturers & Exporters, July, 2010.

[13] "Nuclear power plants, world-wide," European Nuclear Society, [Online]. Available: https://www.euronuclear.org/info/encyclopedia/n/nuclear-power-plant-world-wide.htm. [Accessed 22 08 2016].

[14] *People & Power - Danger Zone: Ageing Nuclear Reactors.* [Film]. Al Jazeera English, 2012.

[15] "Vermont Yankee Nuclear Power Station," U.S. NRC, 16 06 2016. [Online]. Available: http://www.nrc.gov/info-finder/decommissioning/power-reactor/vermont-yankee.html. [Accessed 19 08 2016].

[16] J. Banks, C. John, B. Nelson and D. Nicol, Discrete-Event System Simulation, Prentice Hall, 2001.

[17] K. D. Hamman and R. A. Berry, "A CFD simulation process for fast reactor fuel assemblies," *Nuclear Engineering and Design,* p. 2304–2312, 2010.

[18] D. Chang and S. Tavoularis, "Numerical simulation of turbulent flow in a 37-rod bundle," *Nuclear Engineering and Design,* p. 575–590, 2007.

[19] S. Zhang, Wencong Wang, . L. Yuxuan, F. Jinjun and C. Mingjun , "CANDU refuelling optimization by successive two-step mathematical programming – I: MILP models for refuelling channel selection," *Annals of Nuclear Energy,* p. 1146–1159, 2010.

[20] K. Hangbok Choi and D. Heon, "Refueling Simulation Strategy of a CANDU Reactor Based on Optimum Zone Controller Water Levels," *Nuclear Science and Engineering,* p. 88–94, 2005.

[21] A. Sarchami, N. Ashgriz and M. Kwee, "Three dimensional numerical simulation of a full scale CANDU reactor moderator to study temperature fluctuations," *Nuclear Engineering and Design,* p. 148–154, 2014.

[22] X.-X. Yuan, D. Mao and M. Pandey, "A Bayesian approach to modeling and predictin g pittin g flaws in steam generator tubes," *Reliability Engineering and System Safety,* p. 1838–1847, 2009.

[23] A. Mohany and M. Hassan, "Modelling of fuel bundle vibration and the associated fretting wear in a CANDU fuel channel," *Nuclear Engineering and Design,* p. 214–222, 2013.

[24] J. C. Jo and D. G. Kang, "Prediction of the Local Areas of CANDU Feeder Pipes Highly Susceptible to Wall Thinning Due to Flow-Accelerated Corrosion," in *2007 ASME Pressure Vessels and Piping Division Conference*, San Antonio, Texas, 2007.

[25] X. X. Yuan, M. Panday and G. A. Bickel, "A probabilistic model of wall thinning in CANDU feeders due to flow-accelerated corrosion," *Nuclear Engineering and Design,* p. 16–24, 2008.

[26] G. Provost, "CANDU Course 101," 31 03 2011. [Online]. Available: http://pages.videotron.com/artscie/CANDU/articles/article%20A4.htm. [Accessed 04 12 2016].

[27] K. Burrill and E. Cheluget, "Corrosion of CANDU outlet Feeder Pipes," in *JAIF International Conference on Water Chemistry in Nuclear Power Plants*, Kahiwaszaki, Japan, 1998.

[28] W. Ruehle, H. Neder, R. Holz and V. Schneider, "Oxygen injection into reheating steam moisture separator reheaters," in *14th International Conference on he Properties of Water and Steam*, Kyoto, Japan, Aug. 29-Sept. 3, 2004.

[29] D. Lister, J. Slade and N. Arbeau, "The Accelerated Corrosion of CANDU Outlet Feeders - Observations, Possible Mechanisms and Potential Remedies," in *CNS proceedings of the 1997 CNA/CNS annual conference on powering Canada's future.*, Canada, 1997.

[30] J. M. COULSON and J. F. RICHARDSON, CHEMICAL ENGINEERING Volume 1, Jordan Hill, Oxford: Butterworth-Heinemann, 1999.

[31] "Introduction to ANSYS Fluent," ANSYS, 2014.

[32] R. H. Perry, D. W. Green and J. O. Maloney, Perry's chemical engineers' handbook, United States of America: McGraw-Hill, 1997.

[33] G. Recktenwald, "The k epsilon Turbulence Model," Portland,Oregon, 2009.

[34] C. Rumsey , "The Wilcox k-omega Turbulence Model," Langley Research Center, 08 10 2016. [Online]. Available: https://turbmodels.larc.nasa.gov/wilcox.html. [Accessed 10 01 2018].

[35] W. Frei, "Comsol blog," COMSOL, 06 07 2017. [Online]. Available: https://www.comsol.com/blogs/which-turbulence-model-should-choose-cfd-application/. [Accessed 12 01 2018].

[36] F. Cardarelli, Materials Handbook, London: Springer-Verlag, 2008.

[37] D. R. Lide, CRC Handbook of Chemistry and Physics, Boca Raton: CRC Press, 1999.

[38] "Entrance Length," Aerospace, Mechanical & Mechatronic Engg. University of Sydney, 2005. [Online]. Available: http://www-mdp.eng.cam.ac.uk/web/library/enginfo/aerothermal_dvd_only/aero/fprops/pipeflow/node9.html. [Accessed 12 08 2017].

[39] "The Engineering Page," 2017. [Online]. Available: http://www.the-engineering-page.com/forms/dp/typ_eps.html. [Accessed 09 2017].

[40] "Roughness of pipes," 2017. [Online]. Available: http://www.spray.com/calculators/Pressure_Drop_Calc/rauh.html. [Accessed 09 2017].

[41] "LEAP Australia Computational Fluid Dynamics blog," LEAP CFD Team, 17 01 2012. [Online]. Available: https://www.computationalfluiddynamics.com.au/convergence-and-mesh-independent-study/. [Accessed 22 05 2017].

[42] I. Celik, U. Ghia, P. Roache, C. Freitas, H. Coleman and P. Raad, "Procedure for Estimation and Reporting of Uncertainty Due to Discretization in CFD Applications," *Journal of Fluids Engineering,* vol. 130, no. 7, 2008.

[43] M. Piro and B. Leitch, "Conjugate heat transfer simulations of advanced research reactor fuel," *Nuclear Engineering and Design,* vol. 274, pp. 30-43, 2014.

[44] C. J. Jong, G. K. Dong and W. R. Kyung, "Numerical Calculation of Shear Stress Distribution on the Inner Wall Surface of CANDU Reactor Feeder Pipe Conveing Two-Phase Coolant," *Journal of Pressure Vessel Technology,* vol. 131, pp. 021301-1-13, 2009.

[45] J. M. C. Johari, "Modelling corrosion for corrosion-product transport in CANDU reactors and PWRs," New Brunswick, 1994.

[46] "The Economics of Nuclear Power," World Nuclear Association, 2016. [Online]. Available: http://www.world-nuclear.org/information-library/economic-aspects/economics-of-nuclear-power.aspx. [Accessed 18 10 2016].

[47] D. Ramajo, S. Corzo and N. Schiliuk, "3D modeling of the primary circuit in the reactor pressure vessel of a PHWR," *Nuclear Engineering and Design,* p. 356–365, 2013.

[48] C. Pezze, "Reactor Vessel and Internals Aging Management Technologies," *Nuclear Plant Journal,* pp. 20-24, Mar/Apr 2015.

[49] "The Economic Benefits of Refurbishing and Operating Ontario's Nuclear Reactors," Canadian Manufacturers & Exporters, July, 2010.

[50] J. Busby, R. Nanstad, R. E. Stoller, Z. Feng and D. Naus, "Materials Degradation in Light Water Reactors: Life After 60," Materials Science and Technology Division - Oak Ridge National Laboratory.

[51] P. Wu, "Erosion/Corrosion-Induced Pipe Wall Thinning," U.S. Nuclear Regulatory Commission, 1989.

[52] CNSC Technical Training Group , "Science and Reactor Fundamentals - Materials," January 2003. [Online]. Available: https://canteach.candu.org/Content%20Library/20030301.pdf. [Accessed April 2017].

[53] J. Coulson and J. F. Richardson, Chemical Engineering Volume1, Oxford: Butterworth-Heinemann, 1999.

[54] "Near-wall treatment for k-omega models," 03 11 2011. [Online]. Available: https://www.cfd-online.com/Wiki/Near-wall_treatment_for_k-omega_models. [Accessed 02 09 2017].

[55] F. H. Sweeton and C. F. BaesJr., "The solubility of magnetite and hydrolysis of ferrous ion in aqueous solutions at elevated temperatures," *The Journal of Chemical Thermodynamics,* vol. Volume 2, no. Issue 4, pp. 479-500, July 1970.

[56] "Assessment and management of ageing of major nuclear power plant," International Atomic Energy Authority, Vienna, Austria, 2001.

[57] D. Lochbaum, "Nuclear Pipe Nightmares," 27 10 2015. [Online]. Available: http://allthingsnuclear.org/dlochbaum/nuclear-pipe-nightmares. [Accessed 12 08 2016].

[58] "Outline History of Nuclear Energy," World Nuclear Association, March 2014. [Online]. Available: http://www.world-nuclear.org/information-library/current-and-future-generation/outline-history-of-nuclear-energy.aspx. [Accessed 14 December 2016].

[59] J. H. Spencer, "Results of Air Barbotage Experiments Simulating Two-Phase Flow in a CANDU End Shield During In-Vessel Retention," *Journal of Nuclear Engineering and Radiation Science,* vol. 3, no. 2, 2017.

8 APPENDIX - A

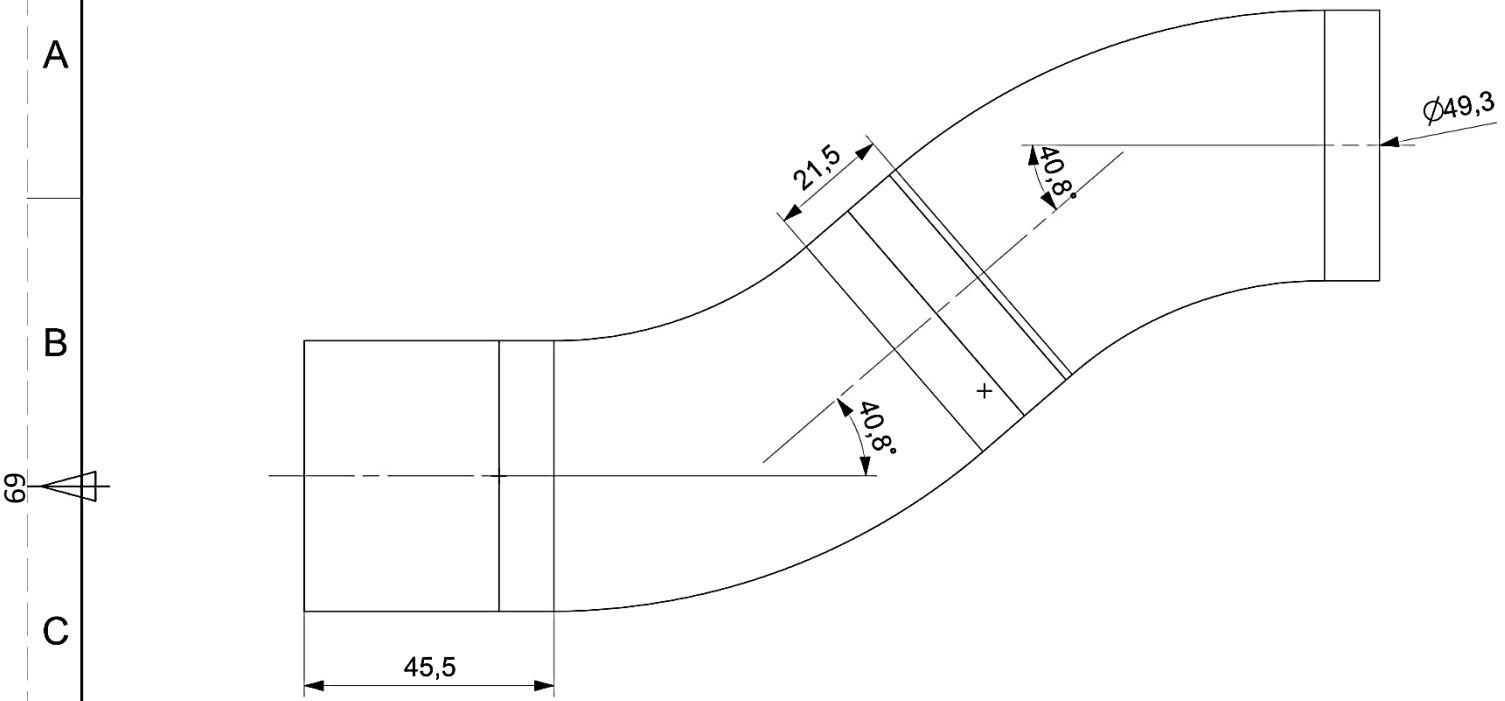

SIEMENS	
FIRST ISSUED	2017/09/29
DRAWN BY	Uditha Wijayaratne
CHECKED BY	
APPROVED BY	

TITLE: Type A

SIZE	DRG NO.	SHEET REV
A4	Type A	A

SHEET 1 OF 1

ALL DIMENSIONS IN MM

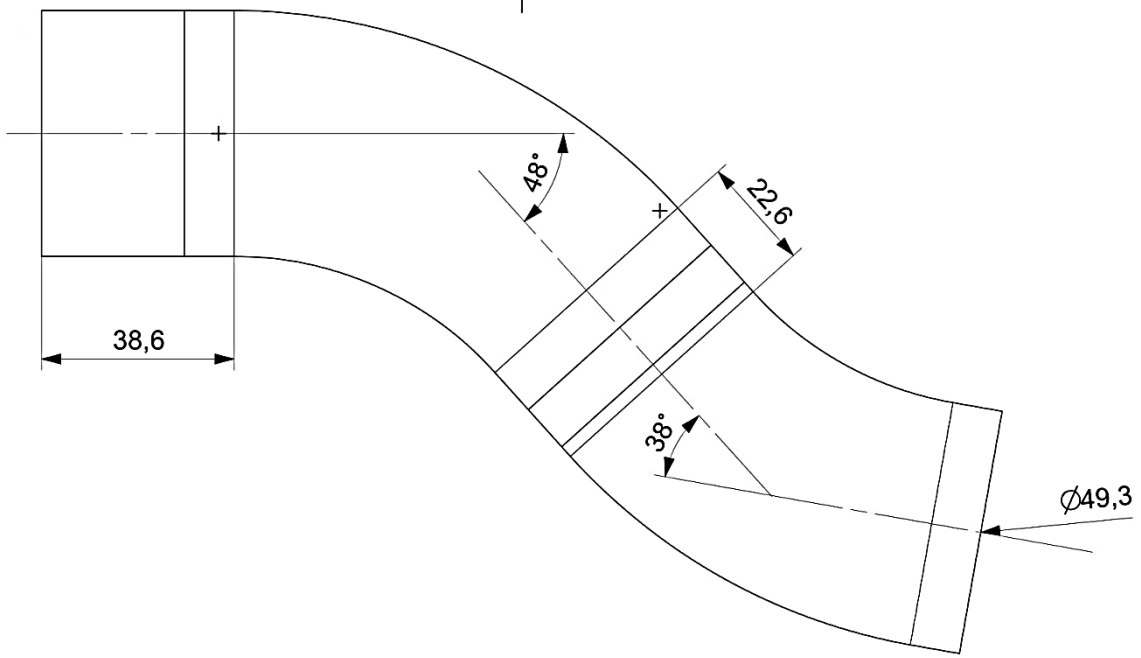

SIEMENS	
FIRST ISSUED	2017/09/29
DRAWN BY	Uditha Wijayaratne
CHECKED BY	
APPROVED BY	

TITLE: Type B

SIZE	DRG NO.	SHEET REV
A4	Type B	A

SHEET 1 OF 1

ALL DIMENSIONS IN MM

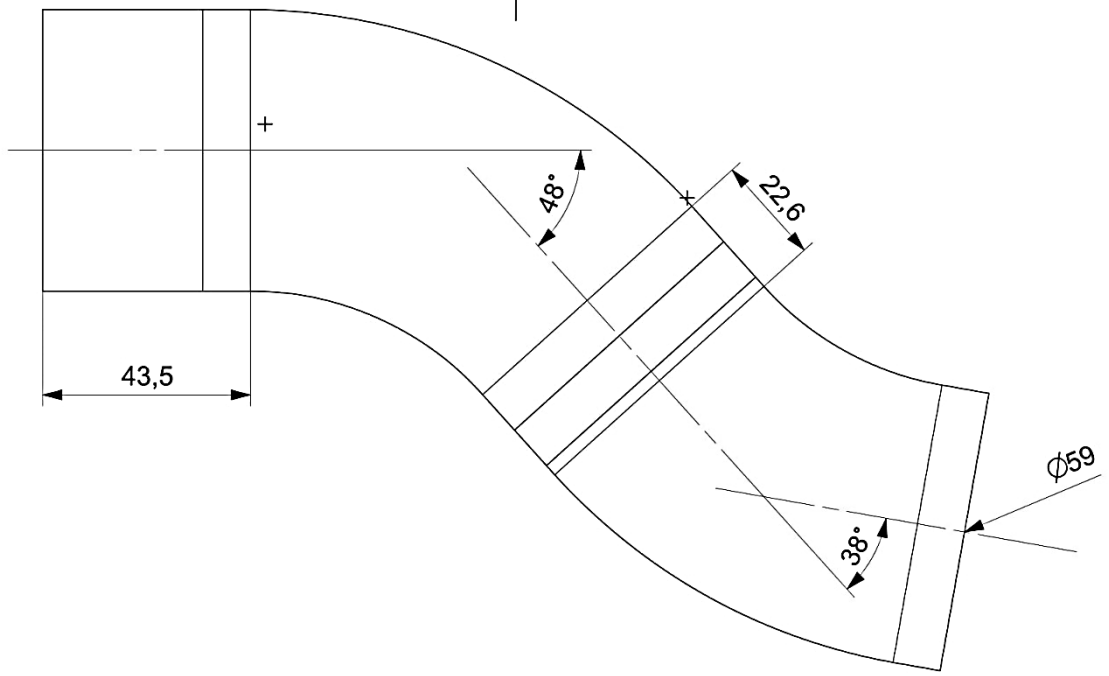

SIEMENS	
FIRST ISSUED	2017/09/29
DRAWN BY	Uditha Wijayaratne
CHECKED BY	
APPROVED BY	

TITLE: Type C

SIZE	DRG NO.	SHEET REV
A4	Type C	A

SHEET 1 OF 1

ALL DIMENSIONS IN MM

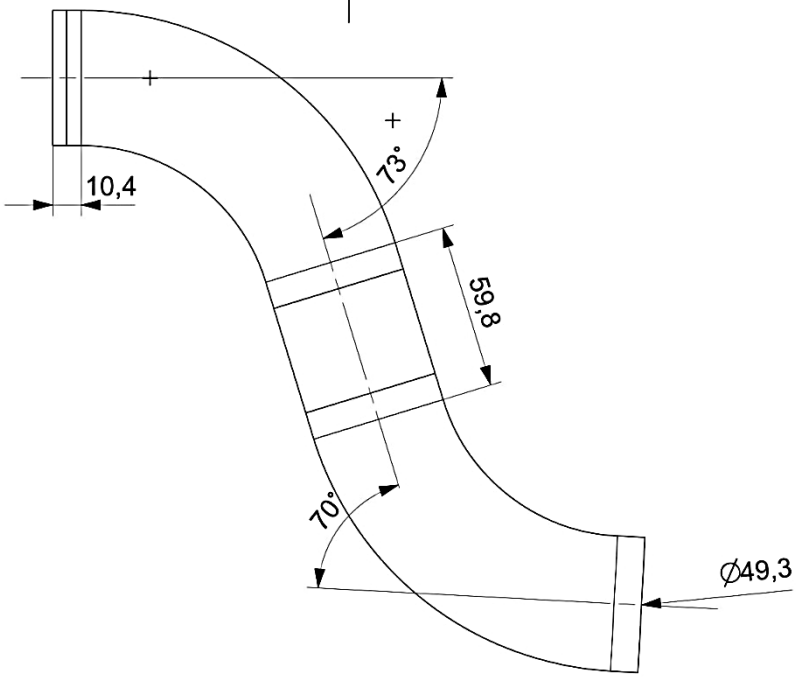

72

SIEMENS	
FIRST ISSUED	2017/09/29
DRAWN BY	Uditha Wijayaratne
CHECKED BY	
APPROVED BY	

TITLE: Type D

SIZE	DRG NO.	SHEET REV
A4	Type D	A

SHEET 1 OF 1

ALL DIMENSIONS IN MM

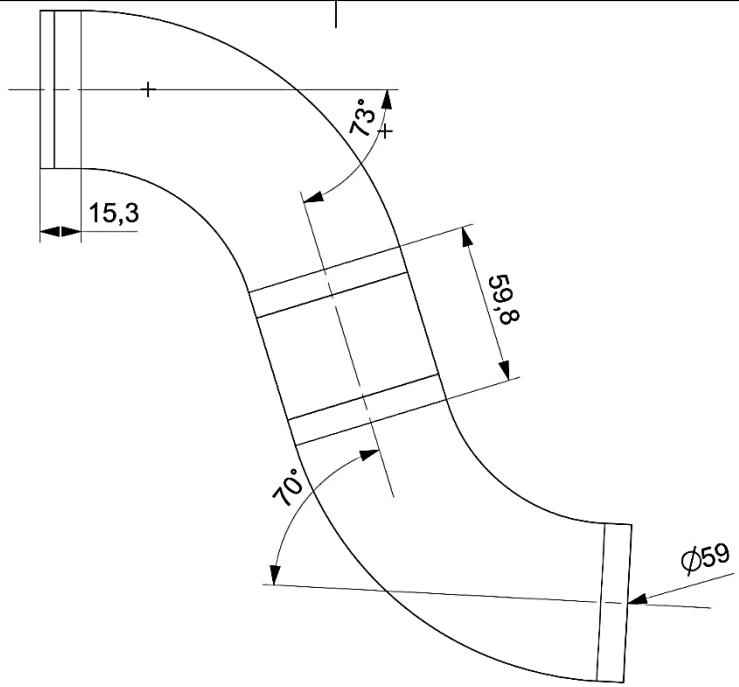

73

SIEMENS	
FIRST ISSUED	2017/09/29
DRAWN BY	Uditha Wijayaratne
CHECKED BY	
APPROVED BY	

TITLE: Type E

SIZE	DRG NO.	SHEET REV
A4	Type E	A

SHEET 1 OF 1

ALL DIMENSIONS IN MM

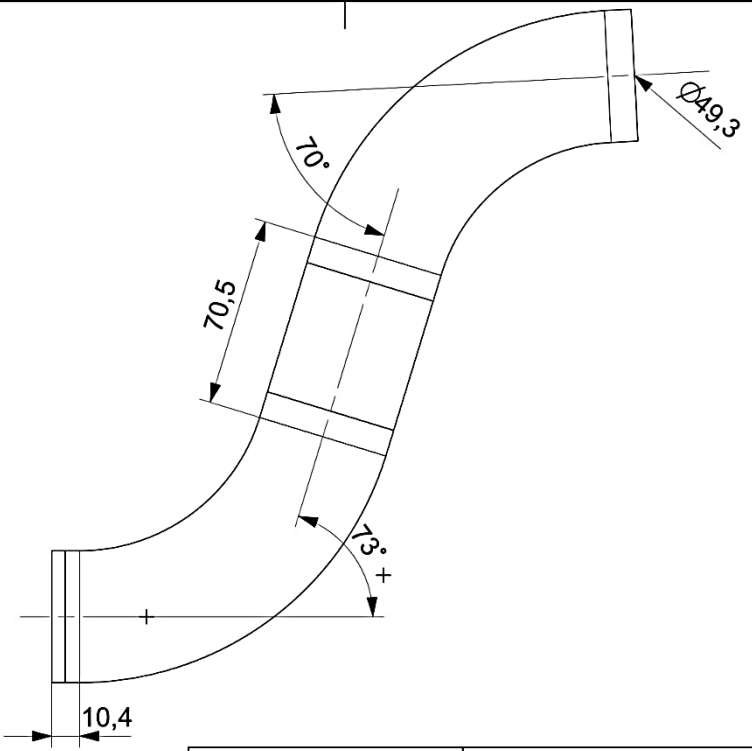

SIEMENS	
FIRST ISSUED	2017/09/29
DRAWN BY	Uditha Wijayaratne
CHECKED BY	
APPROVED BY	

TITLE: Type G1

SIZE	DRG NO.	SHEET REV
A4	Type G1	A

SHEET 1 OF 1

ALL DIMENSIONS IN MM

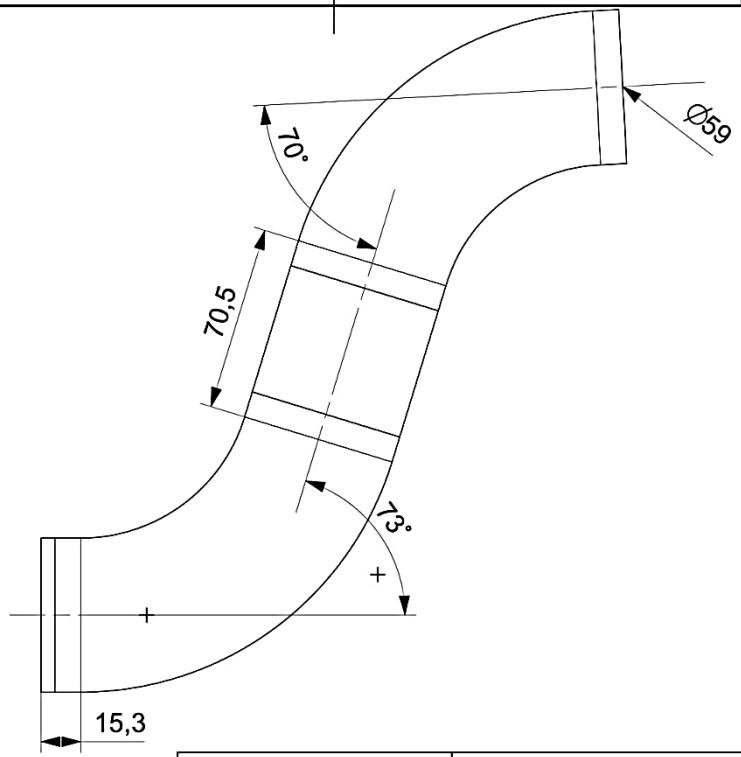

75

SIEMENS	
FIRST ISSUED	2017/09/29
DRAWN BY	Uditha Wijayaratne
CHECKED BY	
APPROVED BY	

TITLE: Type H1

SIZE	DRG NO.	SHEET REV
A4	Type H1	A

SHEET 1 OF 1

ALL DIMENSIONS IN MM

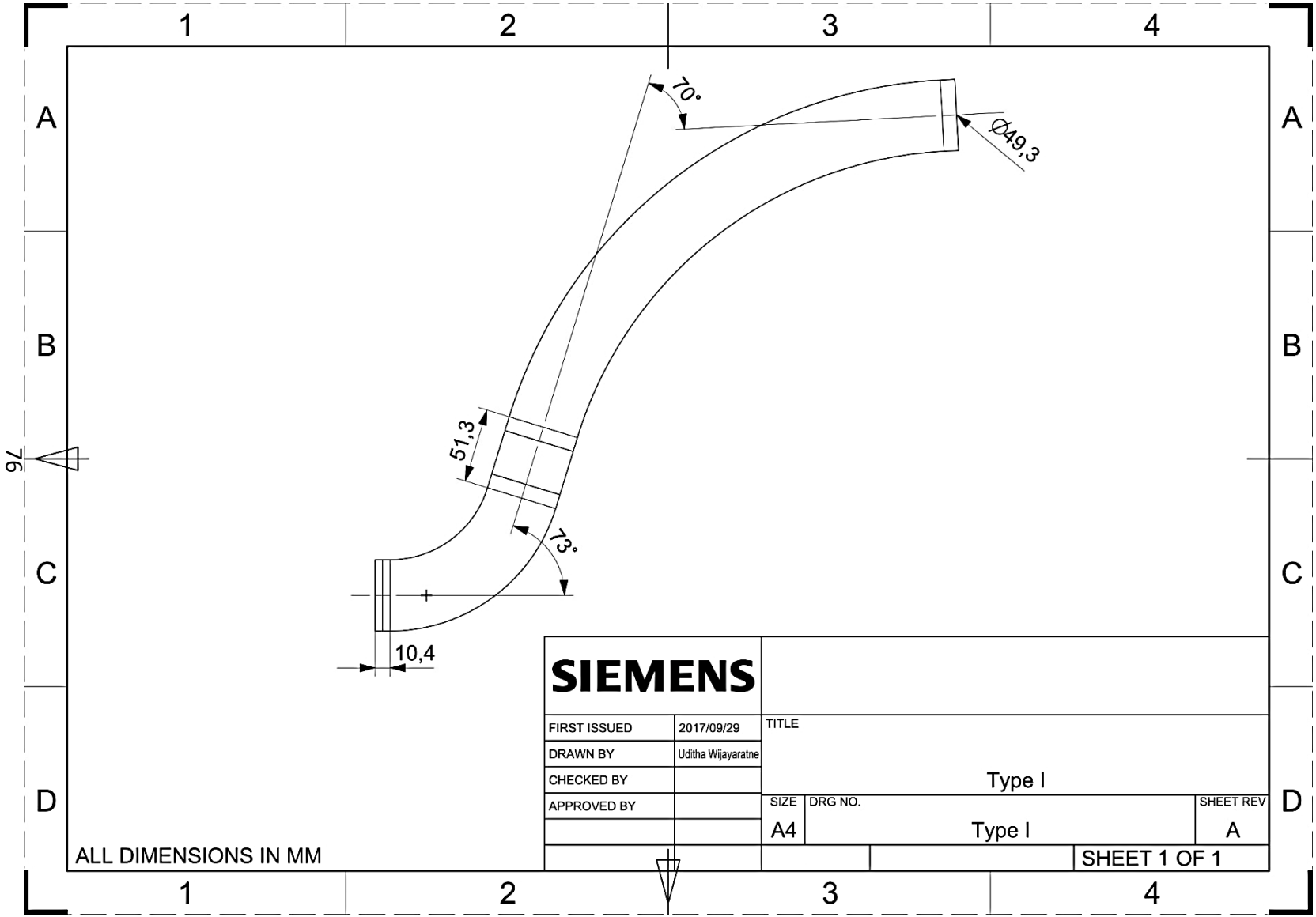

SIEMENS	
FIRST ISSUED	2017/09/29
DRAWN BY	Uditha Wijayaratne
CHECKED BY	
APPROVED BY	

TITLE: Type I

SIZE	DRG NO.	SHEET REV
A4	Type I	A

SHEET 1 OF 1

ALL DIMENSIONS IN MM

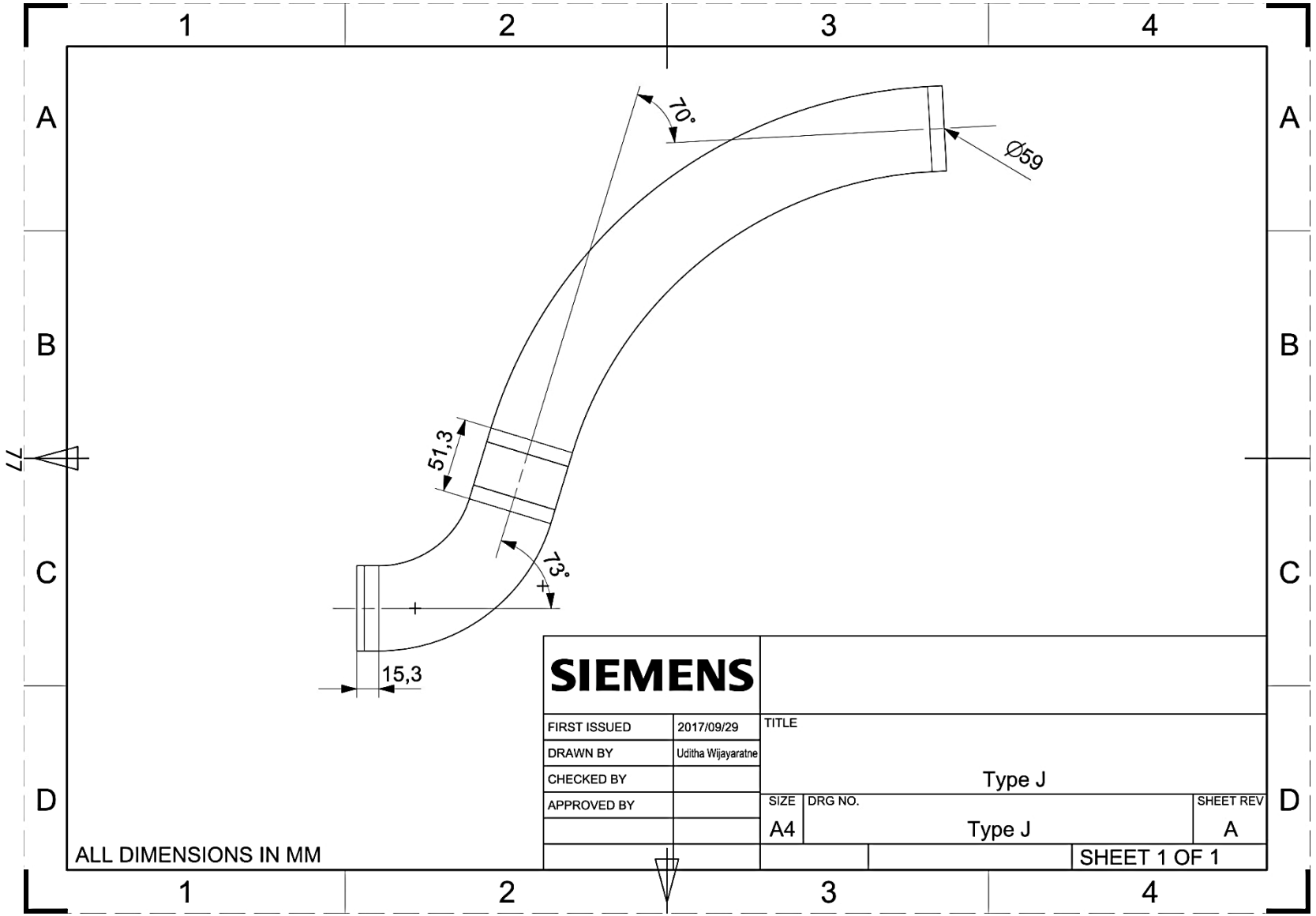
1
2
3
4
A
B
C
D
70°
Ø59
51,3
73°
15,3
77
SIEMENS
FIRST ISSUED 2017/09/29
DRAWN BY Uditha Wijayaratne
CHECKED BY
APPROVED BY
TITLE
Type J
SIZE A4
DRG NO. Type J
SHEET REV A
SHEET 1 OF 1
ALL DIMENSIONS IN MM

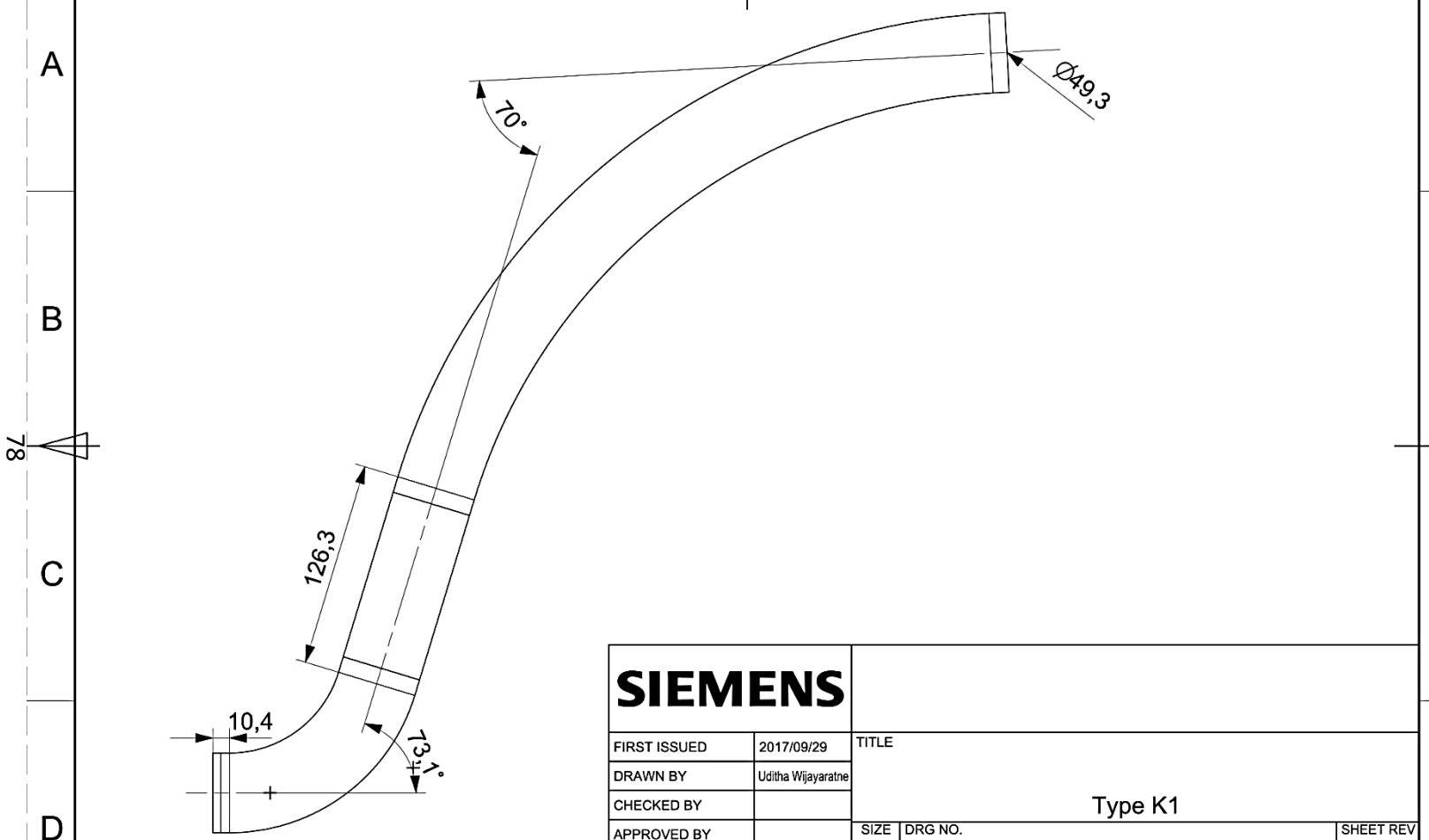

SIEMENS	
FIRST ISSUED	2017/09/29
DRAWN BY	Uditha Wijayaratne
CHECKED BY	
APPROVED BY	

TITLE: Type K1

SIZE	DRG NO.	SHEET REV
A4	Type K1	A

SHEET 1 OF 1

ALL DIMENSIONS IN MM

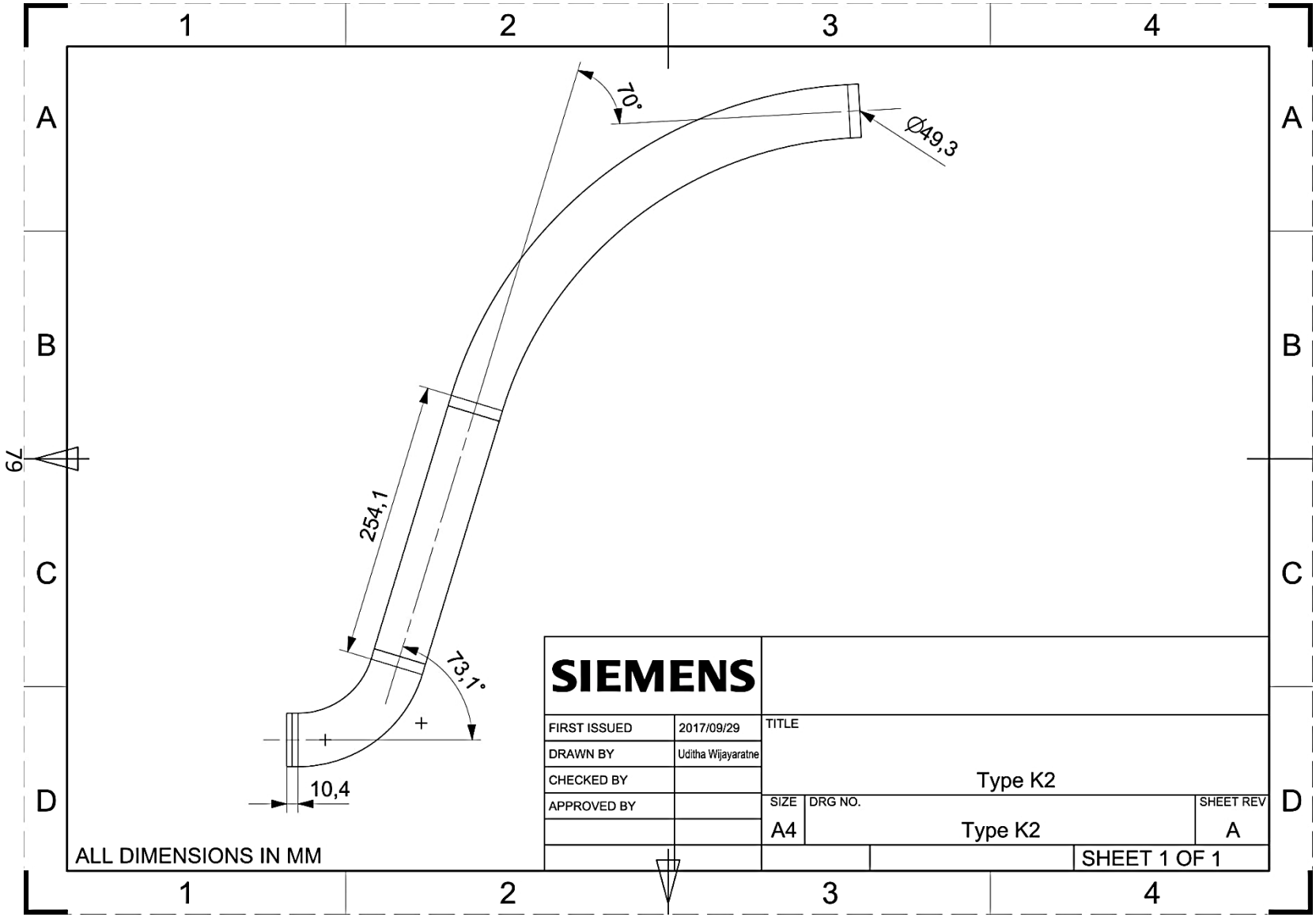

SIEMENS	
FIRST ISSUED	2017/09/29
DRAWN BY	Uditha Wijayaratne
CHECKED BY	
APPROVED BY	

TITLE: Type K2

SIZE	DRG NO.	SHEET REV
A4	Type K2	A

SHEET 1 OF 1

ALL DIMENSIONS IN MM

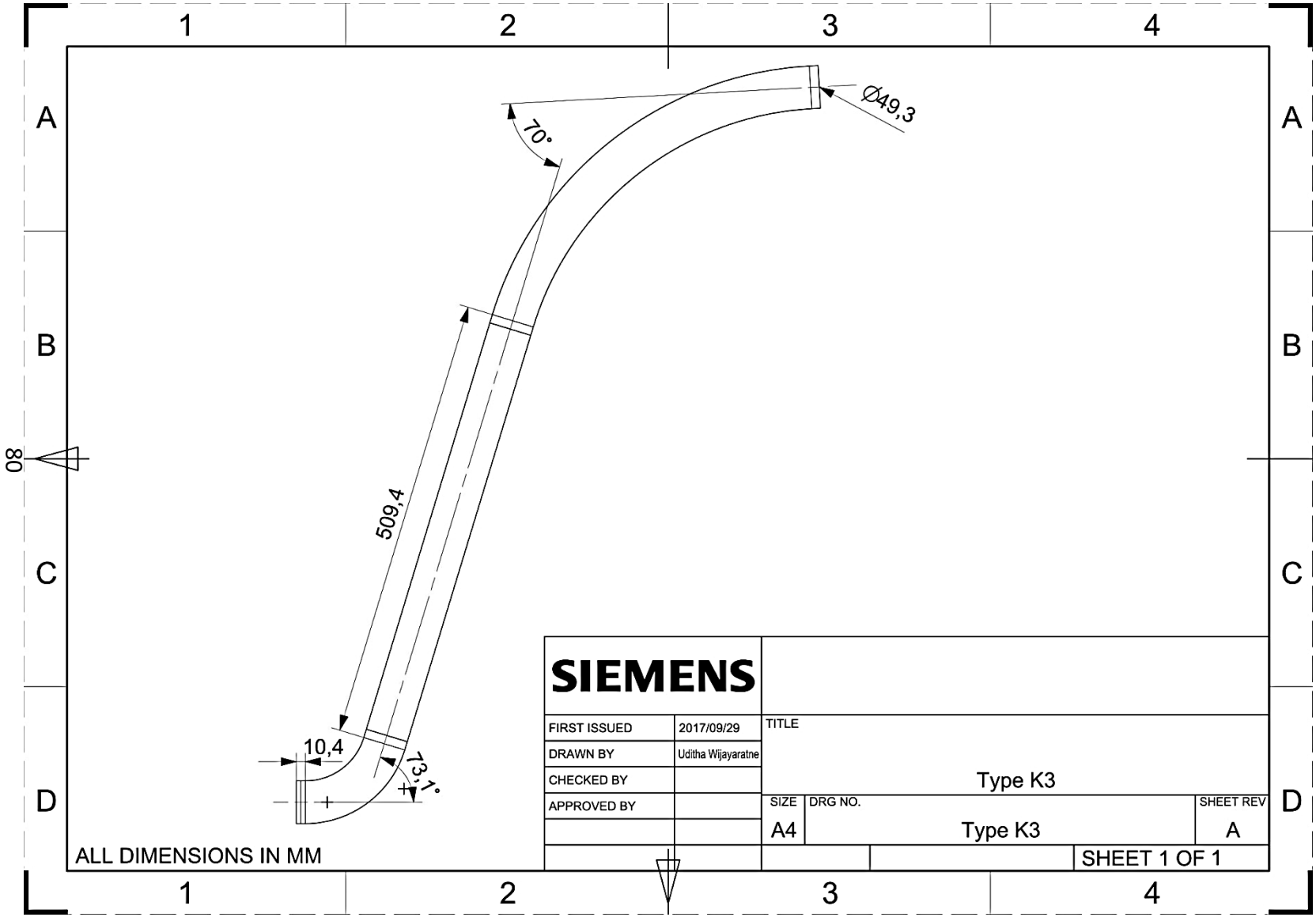
1
2
3
4
A
B
C
D
80
70°
Ø49,3
509,4
10,4
73,1°
ALL DIMENSIONS IN MM
SIEMENS
FIRST ISSUED 2017/09/29
DRAWN BY Uditha Wijayaratne
CHECKED BY
APPROVED BY
TITLE
Type K3
SIZE A4
DRG NO. Type K3
SHEET REV A
SHEET 1 OF 1

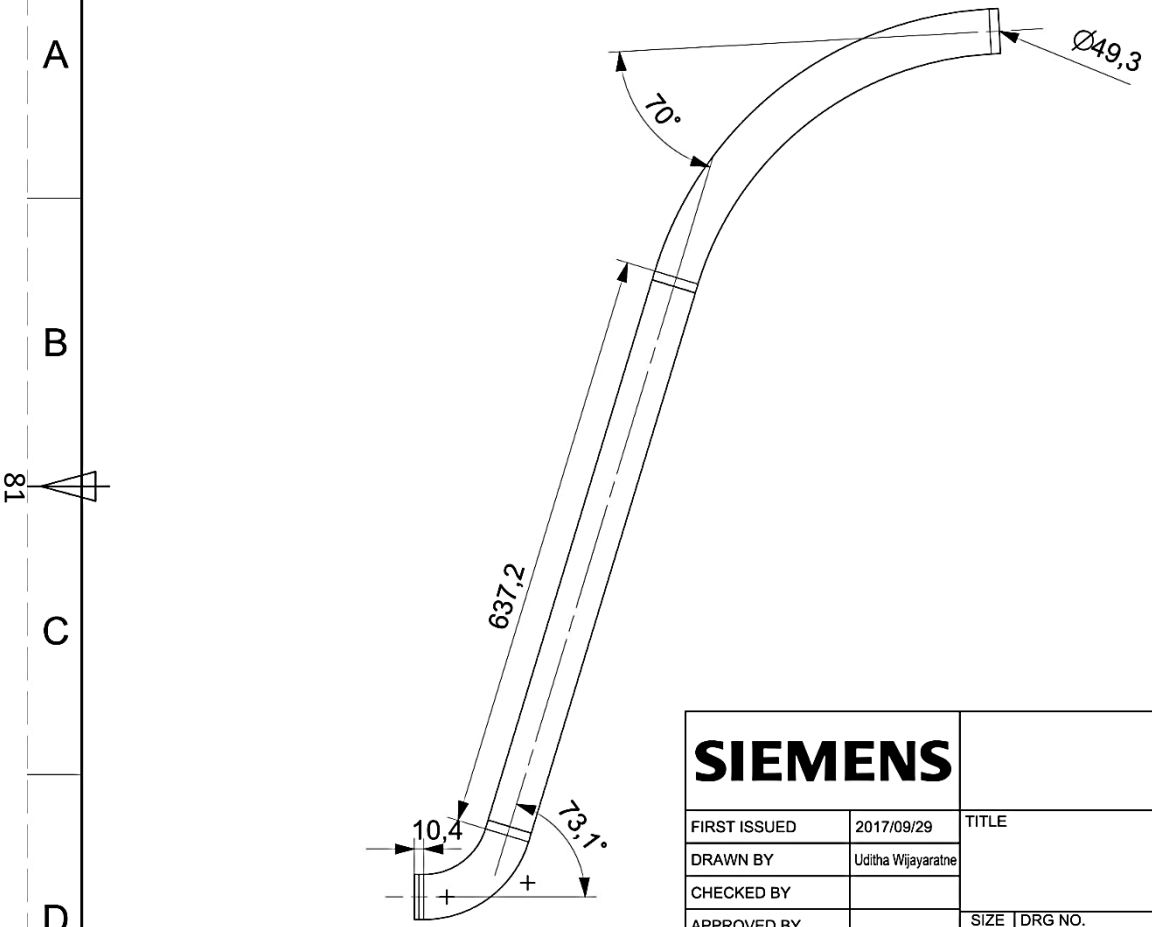

SIEMENS	
FIRST ISSUED	2017/09/29
DRAWN BY	Uditha Wijayaratne
CHECKED BY	
APPROVED BY	

TITLE: Type K4

SIZE	DRG NO.	SHEET REV
A4	Type K4	A

SHEET 1 OF 1

ALL DIMENSIONS IN MM

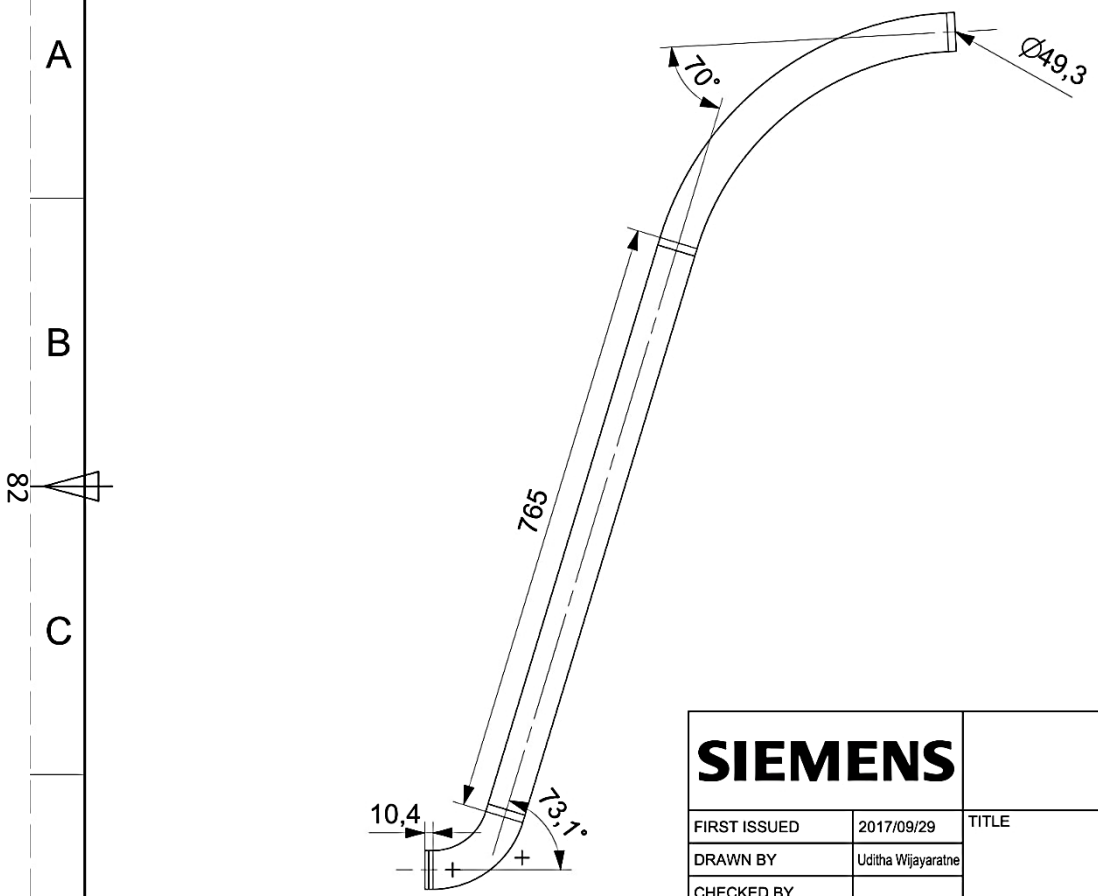

82

SIEMENS	
FIRST ISSUED	2017/09/29
DRAWN BY	Uditha Wijayaratne
CHECKED BY	
APPROVED BY	

TITLE: Type K5

SIZE	DRG NO.	SHEET REV
A4	Type K5	A

SHEET 1 OF 1

ALL DIMENSIONS IN MM

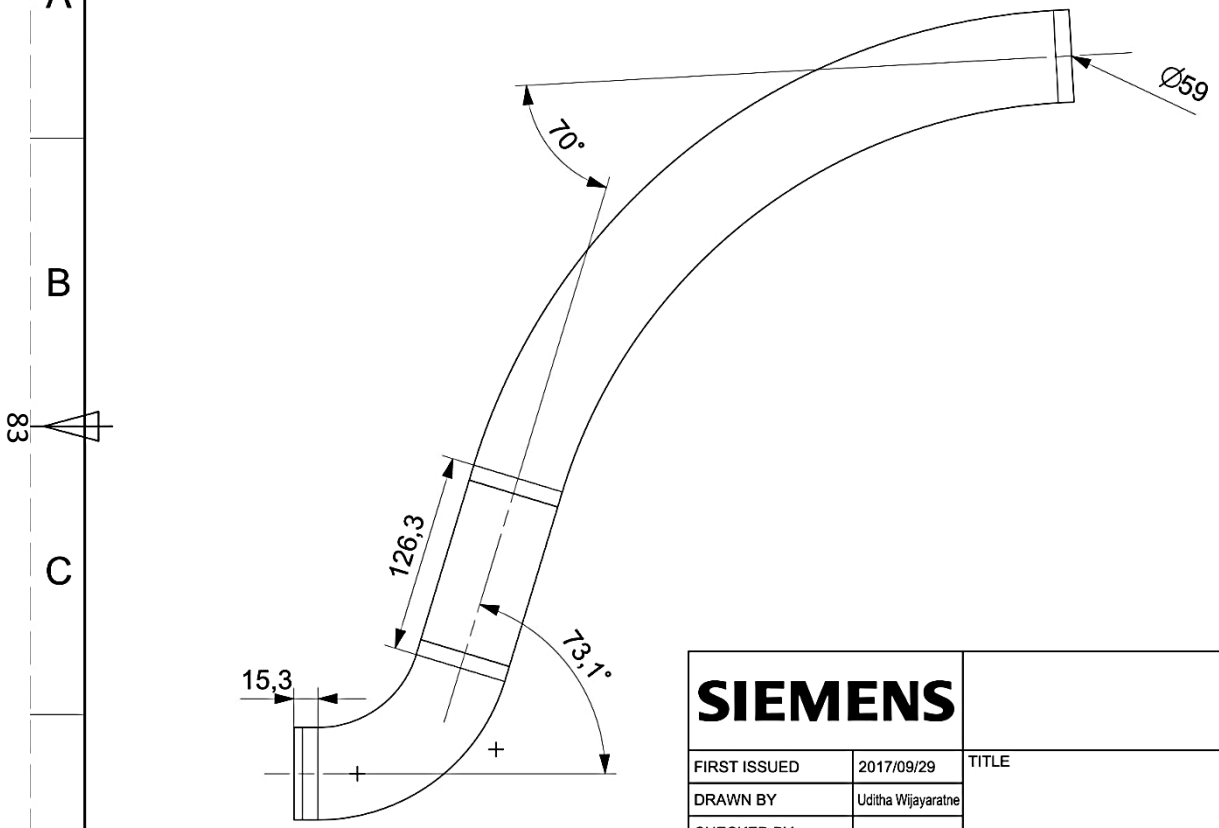

SIEMENS	
FIRST ISSUED	2017/09/29
DRAWN BY	Uditha Wijayaratne
CHECKED BY	
APPROVED BY	

TITLE: Type L1

SIZE	DRG NO.	SHEET REV
A4	Type L1	A

SHEET 1 OF 1

ALL DIMENSIONS IN MM

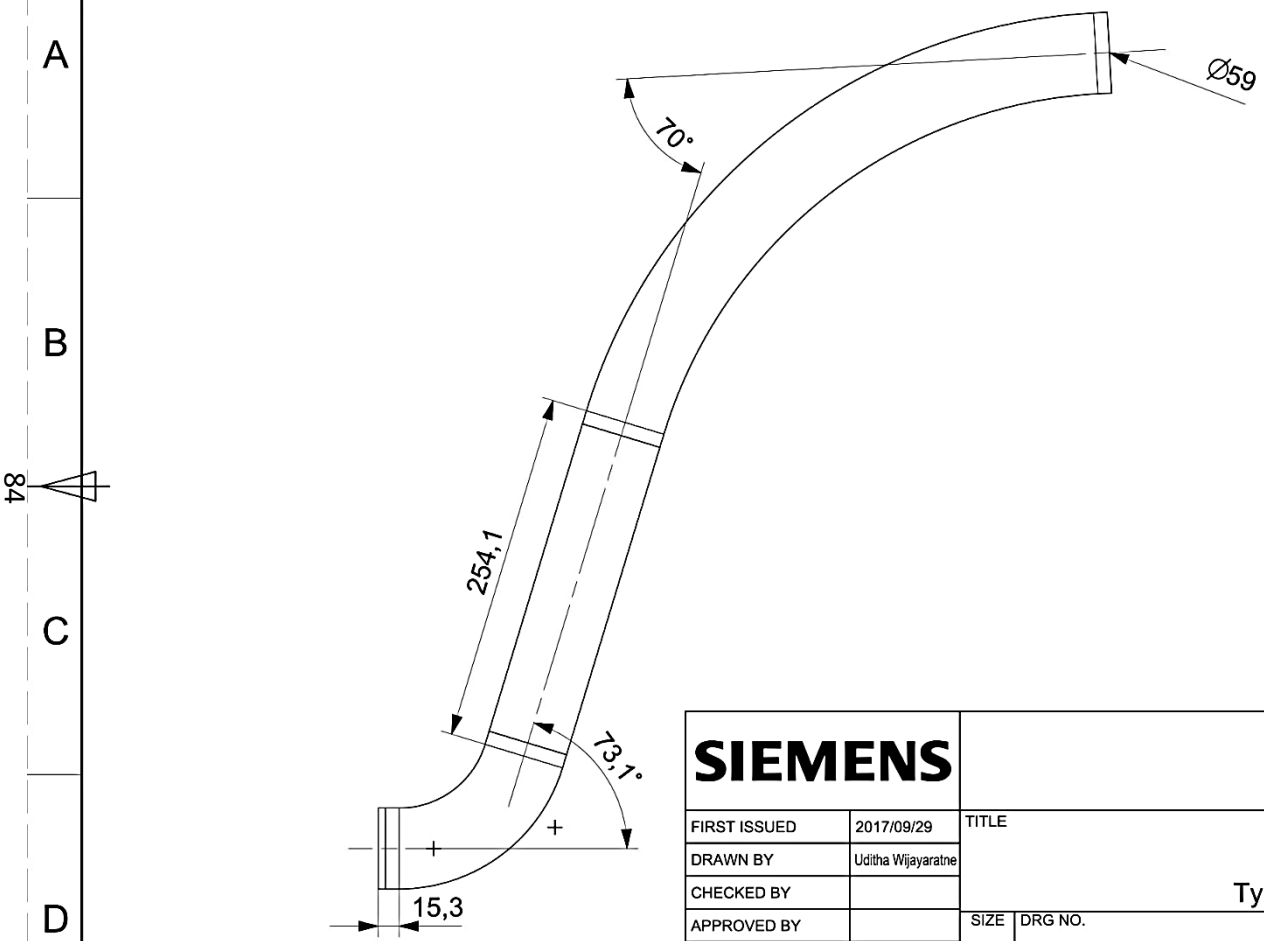

SIEMENS	
FIRST ISSUED	2017/09/29
DRAWN BY	Uditha Wijayaratne
CHECKED BY	
APPROVED BY	

TITLE: Type L2

SIZE	DRG NO.	SHEET REV
A4	Type L2	A

SHEET 1 OF 1

ALL DIMENSIONS IN MM

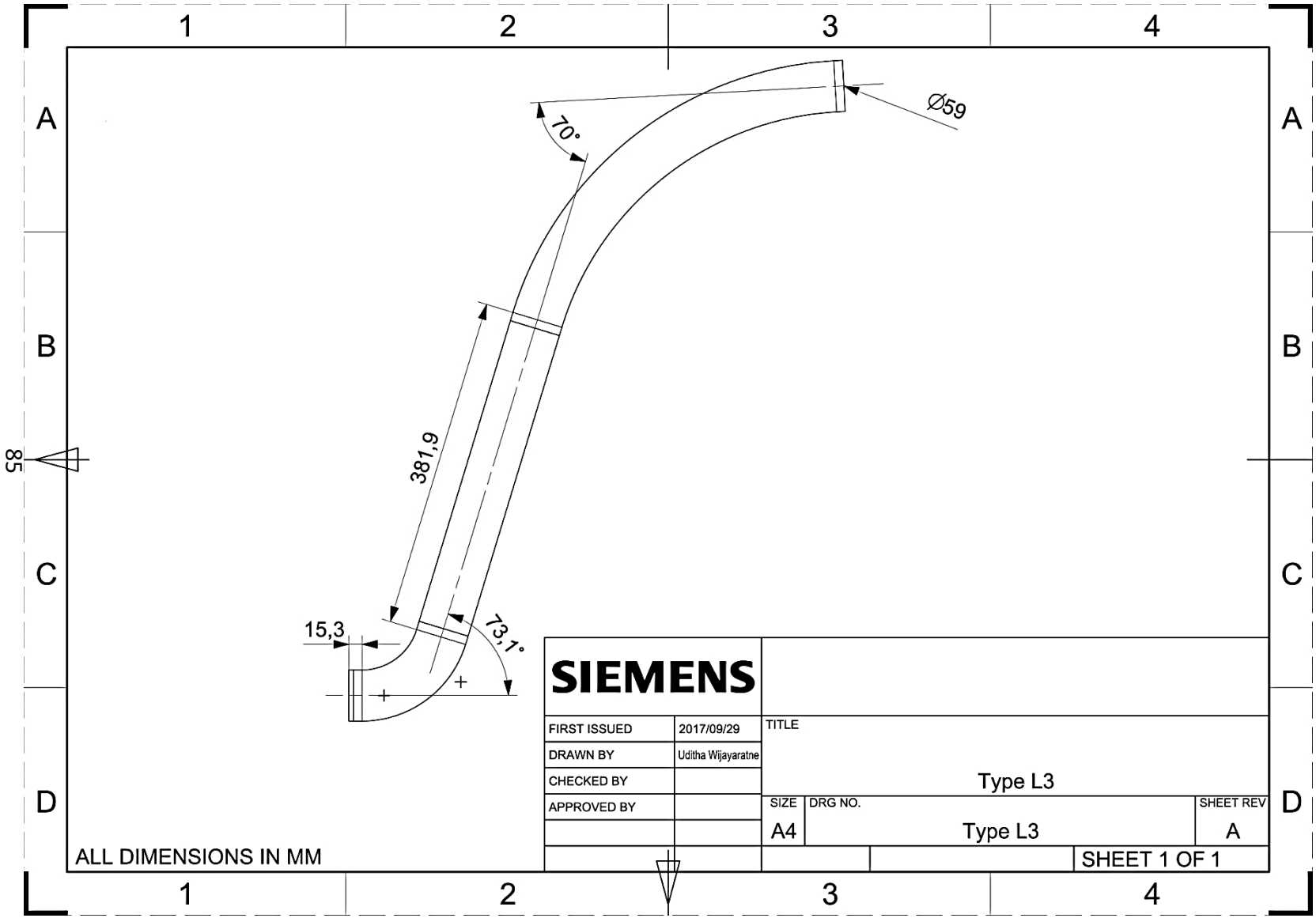
1
2
3
4
A
B
C
D
85
70°
Ø59
381,9
15,3
73,1°
SIEMENS
FIRST ISSUED 2017/09/29
DRAWN BY Uditha Wijayaratne
CHECKED BY
APPROVED BY
TITLE
Type L3
SIZE A4
DRG NO. Type L3
SHEET REV A
SHEET 1 OF 1
ALL DIMENSIONS IN MM

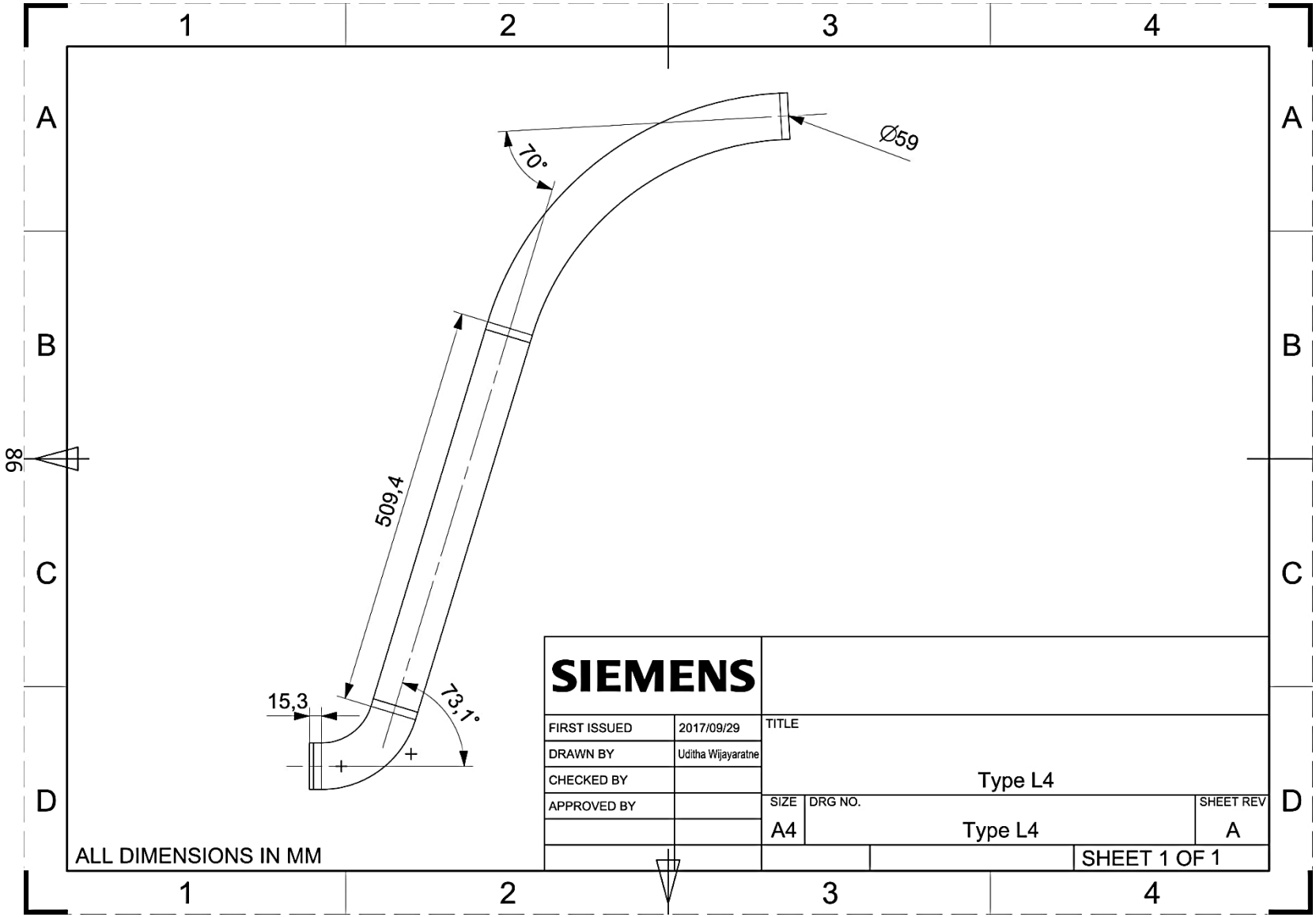
1
2
3
4
A
B
C
D
98
Ø59
70°
509,4
15,3
73,1°
ALL DIMENSIONS IN MM
SIEMENS
FIRST ISSUED 2017/09/29
DRAWN BY Uditha Wijayaratne
CHECKED BY
APPROVED BY
TITLE
Type L4
SIZE A4
DRG NO. Type L4
SHEET REV A
SHEET 1 OF 1

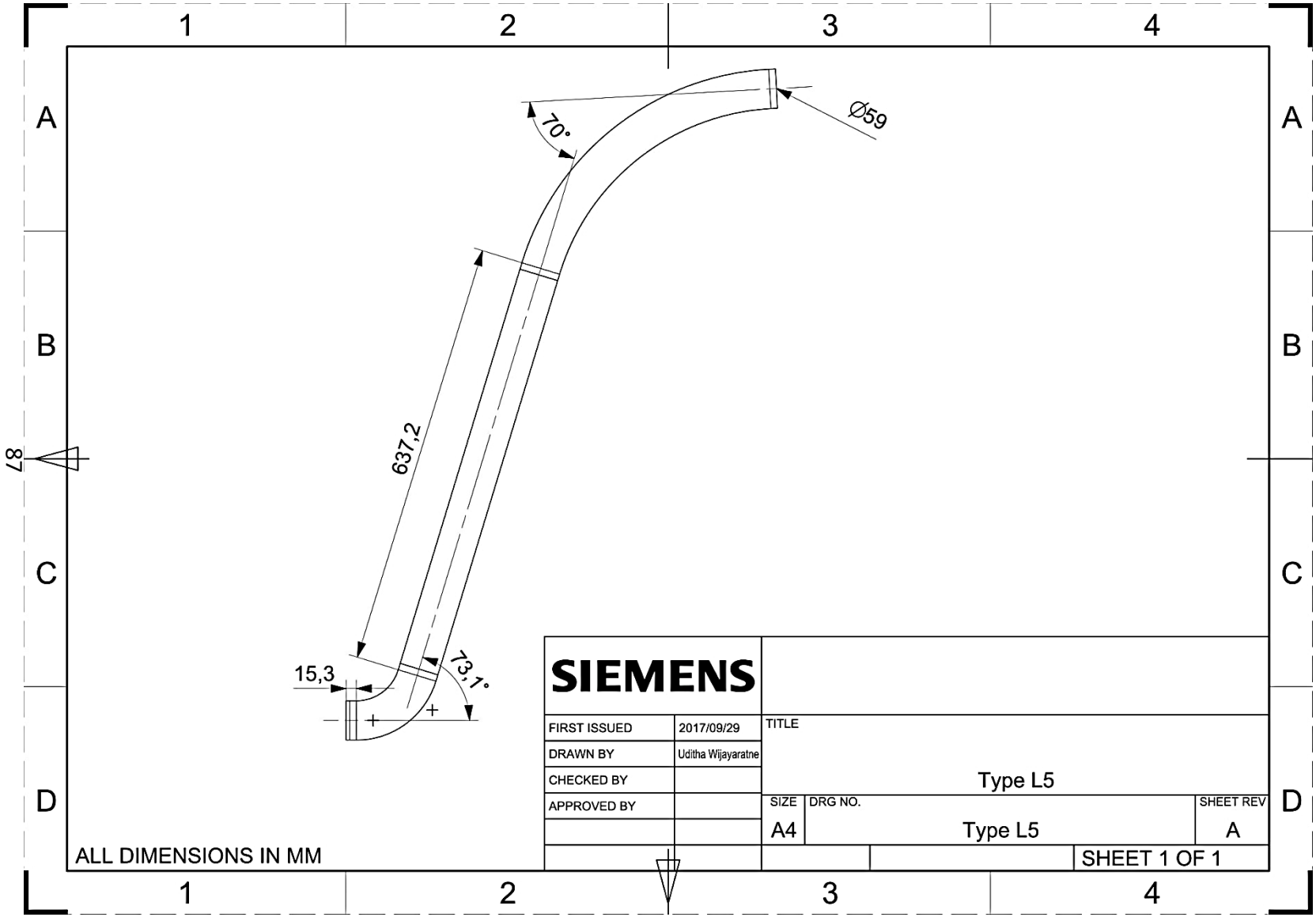
1
2
3
4
A
B
C
D
70°
Ø59
637,2
87
15,3
73,1°
SIEMENS
FIRST ISSUED
2017/09/29
DRAWN BY
Uditha Wijayaratne
CHECKED BY
APPROVED BY
TITLE
Type L5
SIZE
A4
DRG NO.
Type L5
SHEET REV
A
SHEET 1 OF 1
ALL DIMENSIONS IN MM

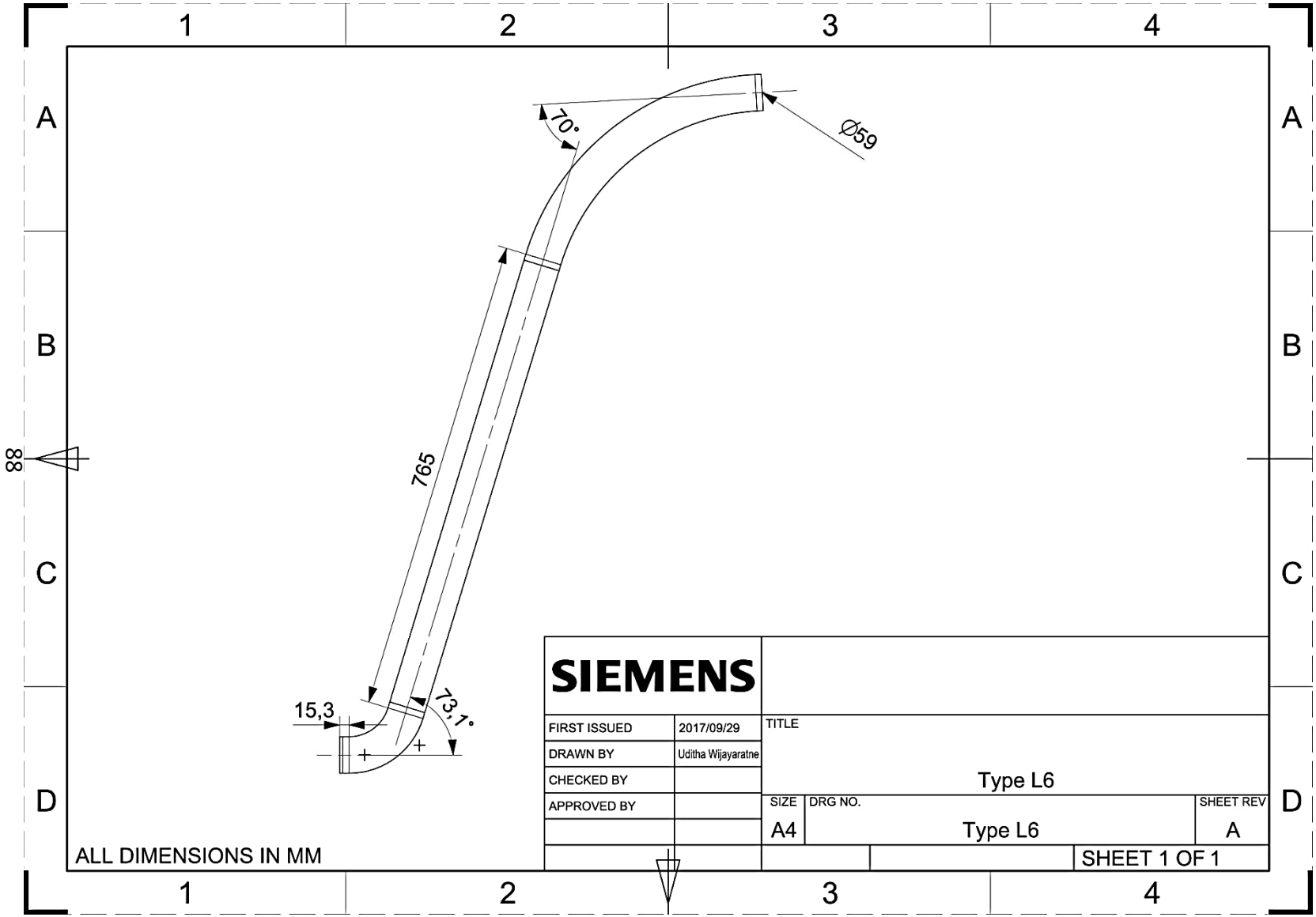
1
2
3
4
A
B
C
D
88
70°
Ø59
765
15,3
73,1°
ALL DIMENSIONS IN MM
SIEMENS
FIRST ISSUED 2017/09/29
DRAWN BY Uditha Wijayaratne
CHECKED BY
APPROVED BY
TITLE
Type L6
SIZE A4
DRG NO. Type L6
SHEET REV A
SHEET 1 OF 1

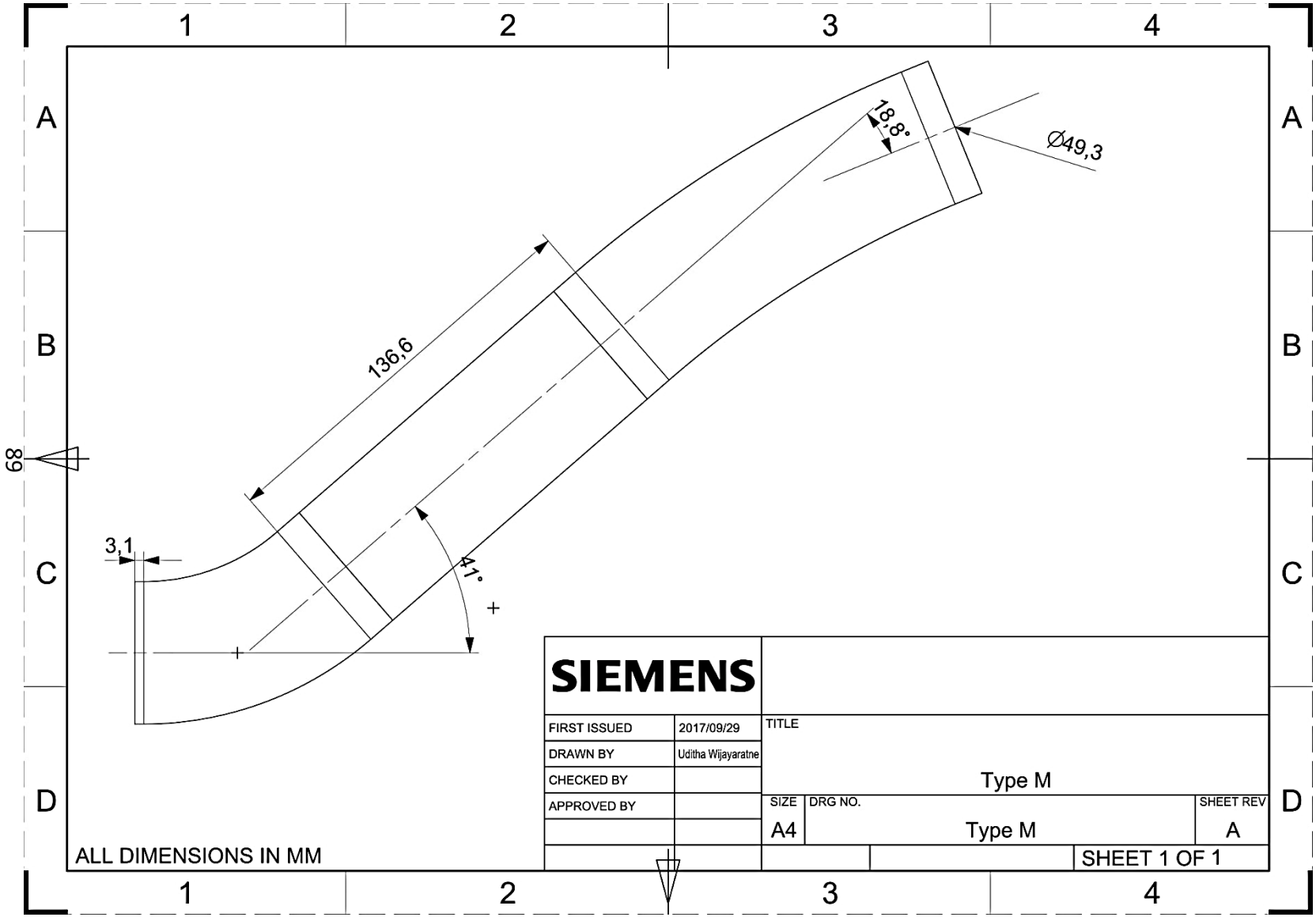
1
2
3
4
A
B
C
D
68
136,6
18,8°
Ø49,3
3,1
41°
SIEMENS
FIRST ISSUED 2017/09/29
DRAWN BY Uditha Wijayaratne
CHECKED BY
APPROVED BY
TITLE
Type M
SIZE A4
DRG NO. Type M
SHEET REV A
SHEET 1 OF 1
ALL DIMENSIONS IN MM

9 APPENDIX - B

The geometry of the first bend (B1) was meshed with seven different mesh models changing the surface mesh size to compare the variation of y^+ and wall shear stress. The surface mesh size, maximum y^+ (surface) value and the maximum wall shear stress values recorded in each mesh model are summarized in Table 14.

Table 14: Comparison of y^+ and wall shear stress

Mesh model	Surface mesh size (mm)	Maximum Y Plus (surface)	Max. wall shear stress (kPa)
1	0.1 x 0.50	24.709	2.955
2	0.1 x 0.25	09.527	1.695
3	0.1 x 0.22	07.145	1.585
4	0.1 x 0.21	06.248	1.549
5	0.1 x 0.20	05.275	1.513
6	0.1 x 0.18	04.196	1.497
7	0.1 x 0.12	01.000	1.480

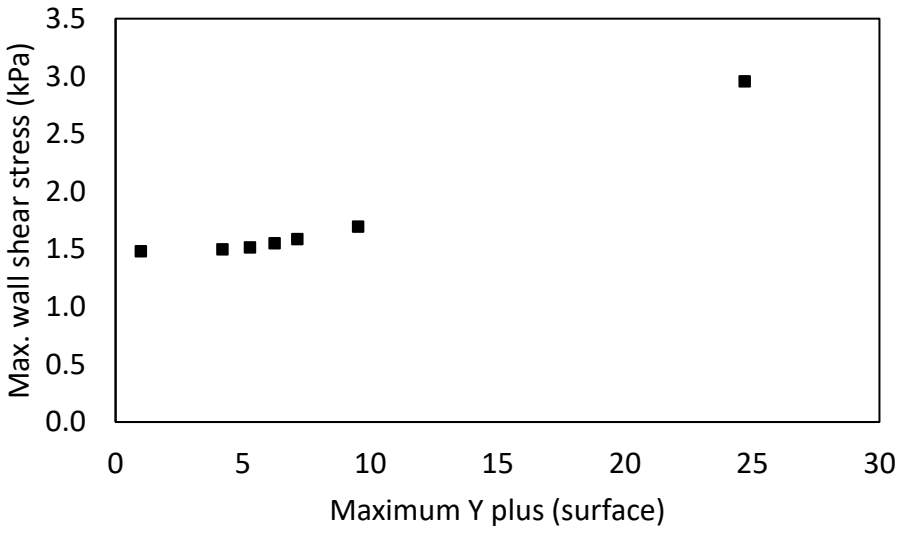

Figure 31: Variation of wall shear stress w.r.t y^+ value

According to the results in Table 14 as well as in Figure 31, it is clear that the maximum wall shear stress within the first bend (B1) geometry changes with respect to the y^+ (surface) value in mesh models 1 and 2. However, the maximum wall shear stress value does not change significantly with models 3 to 6. These models are having a maximum y^+ (surface) values in the range of 4.196 to 7.145. Moreover, the maximum y^+ (surface) is reduced to 1 and still the maximum wall shear stress value does not show any significant variation.

10 APPENDIX - C

Comparison of different turbulent models

Three different meshes were developed for the geometry of the first bend (B1) by varying the source element size as 0.2 mm, 0.25 mm and 0.5 mm (Figure 32). Then, the CFD analysis was performed with using the K-Omega turbulence model to compare the maximum wall shear stress at the first bend. According to the results in Figure 33, it is evident that the maximum wall shear stress is reduced considerably when the source element size is reduced to 0.25 mm from 0.5 mm. However, the maximum wall shear stress value has not changed significantly even though the mesh source element size is further reduced to 0.2 mm. On the other hand, solution time has significantly increased when the source element size is reduced from 0.5 mm to 0.25 mm. Moreover, the solution time has drastically increased when the source element size is further reduced to 0.2 mm. Therefore, source element size of 0.25 mm is acceptable considering the solution accuracy and the demanded computational power.

It is also important to compare the results with different turbulence models. The same analysis was performed with using K-Omega, SST, and Fixed turbulent viscosity models. In order to perform the CFD analysis using the SST and Fixed turbulent viscosity models, the same source element size (0.25 mm) and boundary conditions were used. Figure 34 shows the variation of wall shear stress and corresponding solution time under different flow solvers. K-Omega and SST models show a similar result for the maximum wall shear stress value at B1. However, the drastically different wall shear stress value for B1 under the fixed turbulent viscosity model implies the inability of applying the fixed turbulent viscosity model towards this study. Still, the higher solution time corresponding to the SST model clearly shows the higher demand for computational power. Therefore, it is reasonable to select K-Omega turbulence model for the CFD analysis during this study.

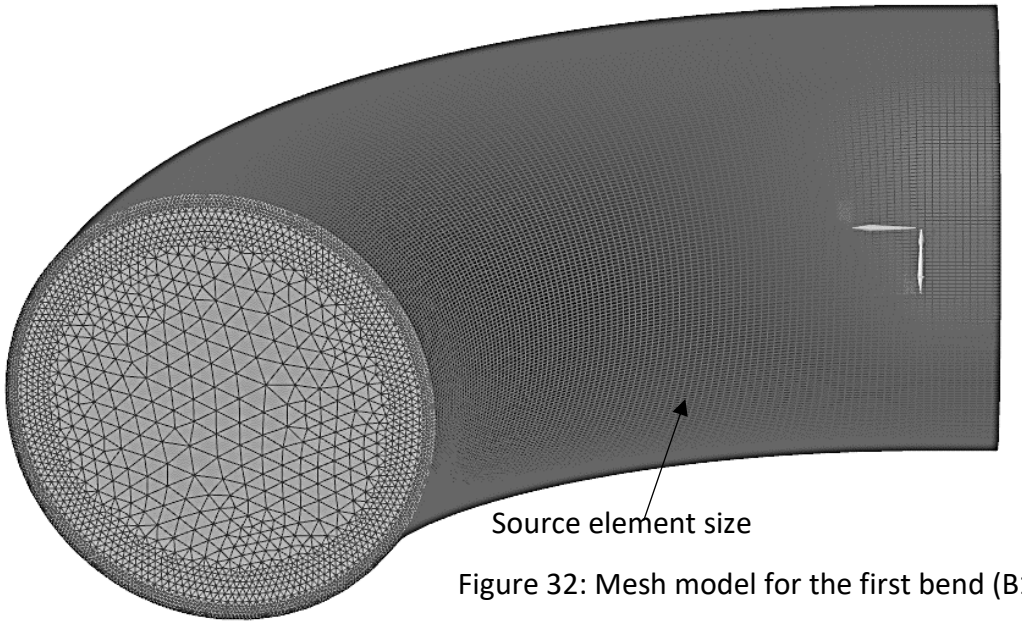

Figure 32: Mesh model for the first bend (B1)

Table 15 summarize the convergence details for different mesh models and flow solvers.

Table 15: Summary of convergence details for different turbulence models

Mesh Model	Source Element Size	Max. wall shear (kPa)	Residual imbalance			Velocity			Flow Residual Target	Solution Time (Hrs)
			Momentum	Mass	Energy	Max	Min	Average		
K-Ω 0.20 mm	0.2	1.513	5.16E-03	0.00E+00	0.00E+00	1.23E+01	4.87E-03	6.05E+00	YES	3.2
K-Ω 0.25 mm	0.25	1.695	1.11E-02	0.00E+00	0.00E+00	1.24E+01	4.35E-03	6.20E+00	YES	2.1
K-Ω 0.50 mm	0.5	2.856	9.36E-03	0.00E+00	0.00E+00	1.27E+01	1.06E-02	7.15E+00	YES	1.1
SST 0.25 mm	0.25	1.707	-1.28E-03	0.00E+00	0.00E+00	1.23E+01	2.11E-03	6.29E+00	YES	6.8
Fixed Turb. viscosity 0.25 mm	0.25	15.007	-0.14143	0.00E+00	0.00E+00	1.67E+01	3.21E-01	3.27E+00	YES	0.8

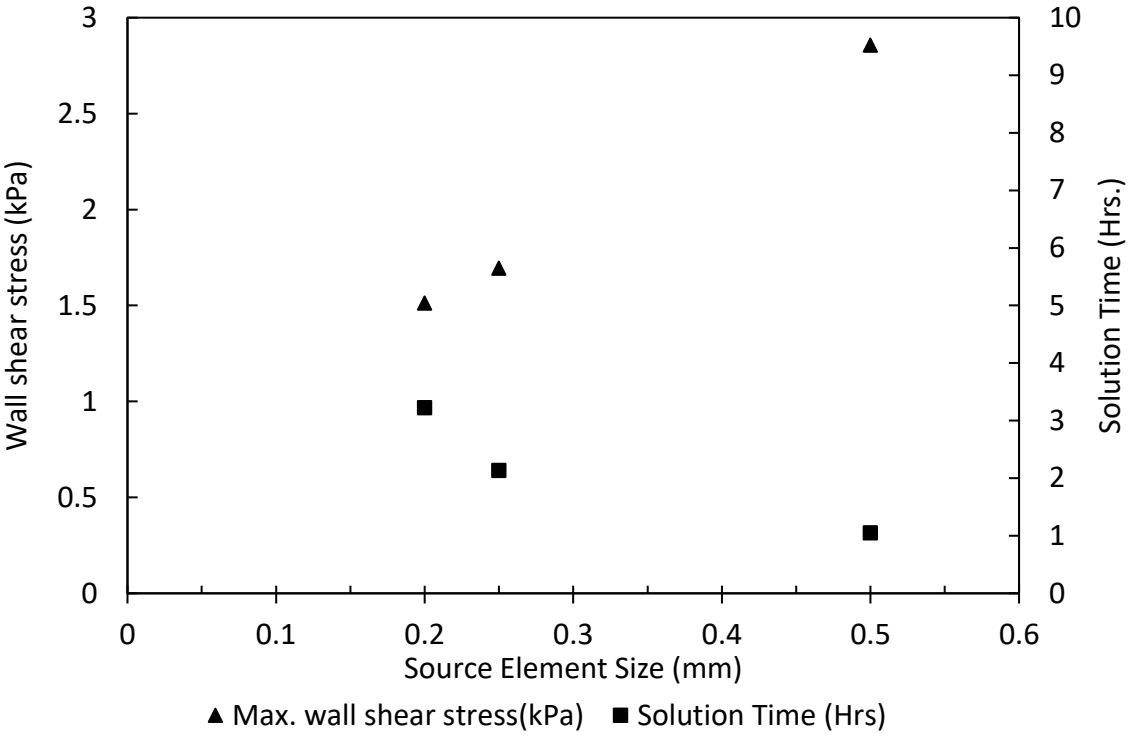

Figure 33: Variation of wall shear stress and solution time vs. Source element size

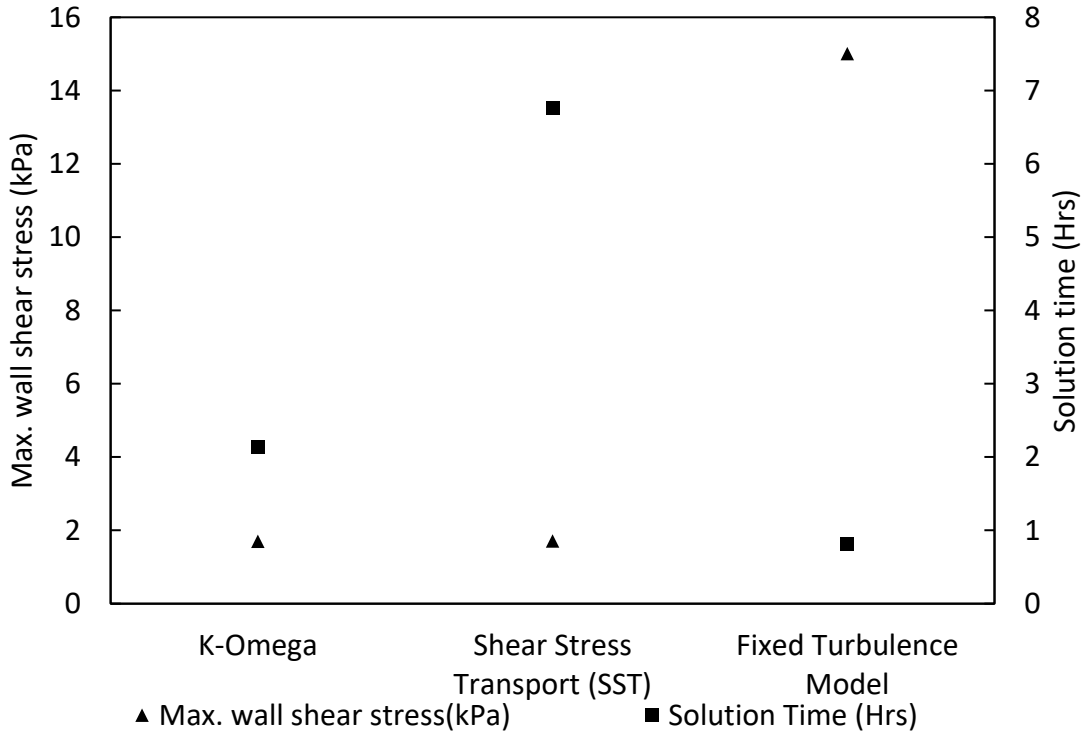

Figure 34: Variation of wall shear stress and solution time under different flow solvers

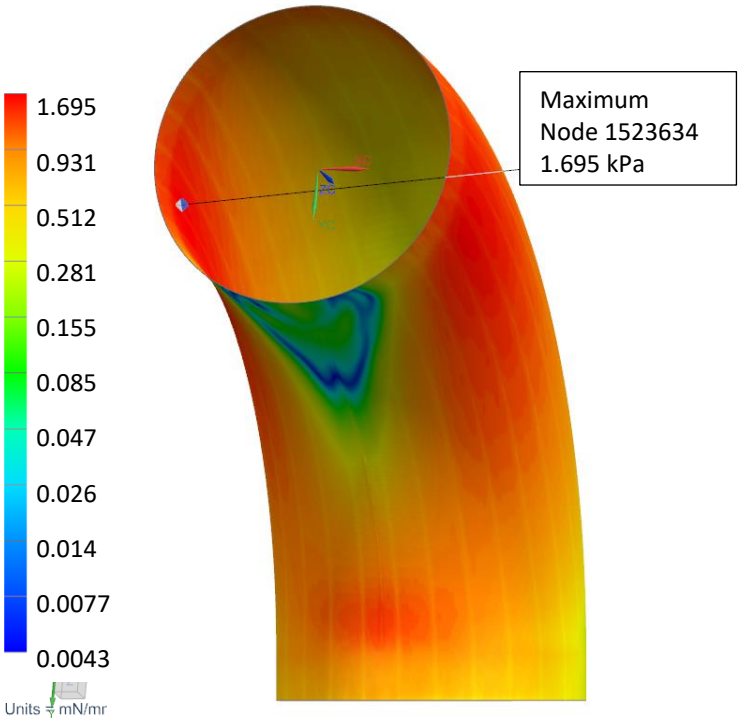

Figure 35: Wall shear stress distribution -K-Omega (0.25 mm source element size)

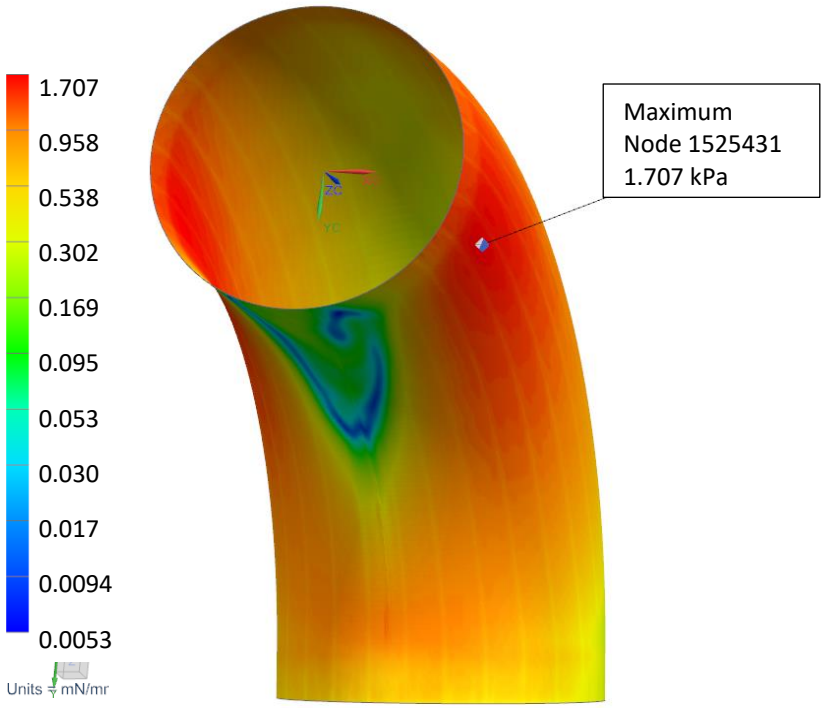

Figure 36: Wall shear stress distribution - SST (0.25 mm source element size)

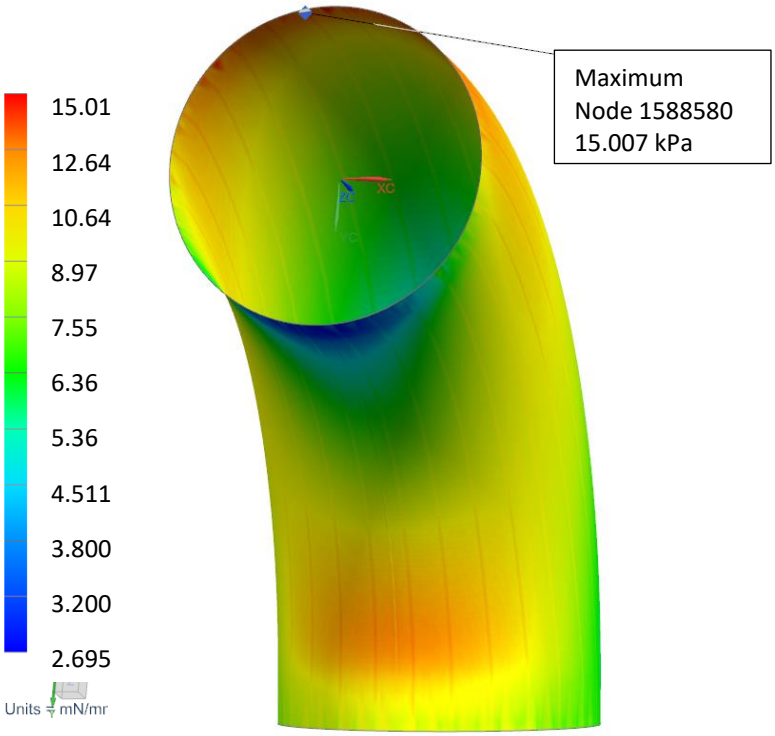

Figure 37: Wall shear stress distribution - Fixed Turbulence Model (0.25 mm source element size)

11 APPENDIX - D

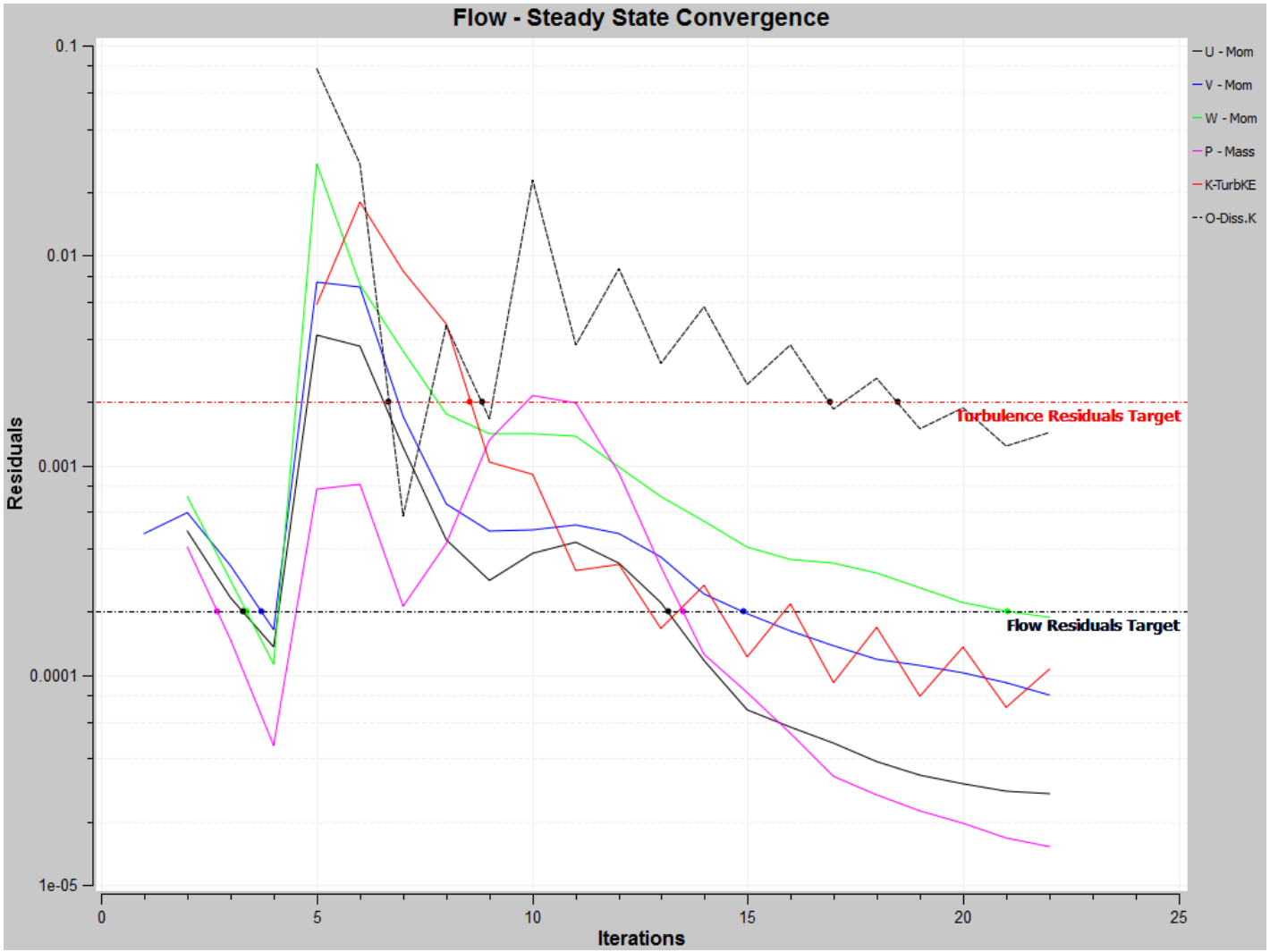

Figure 38: Steady State Convergence – Model A

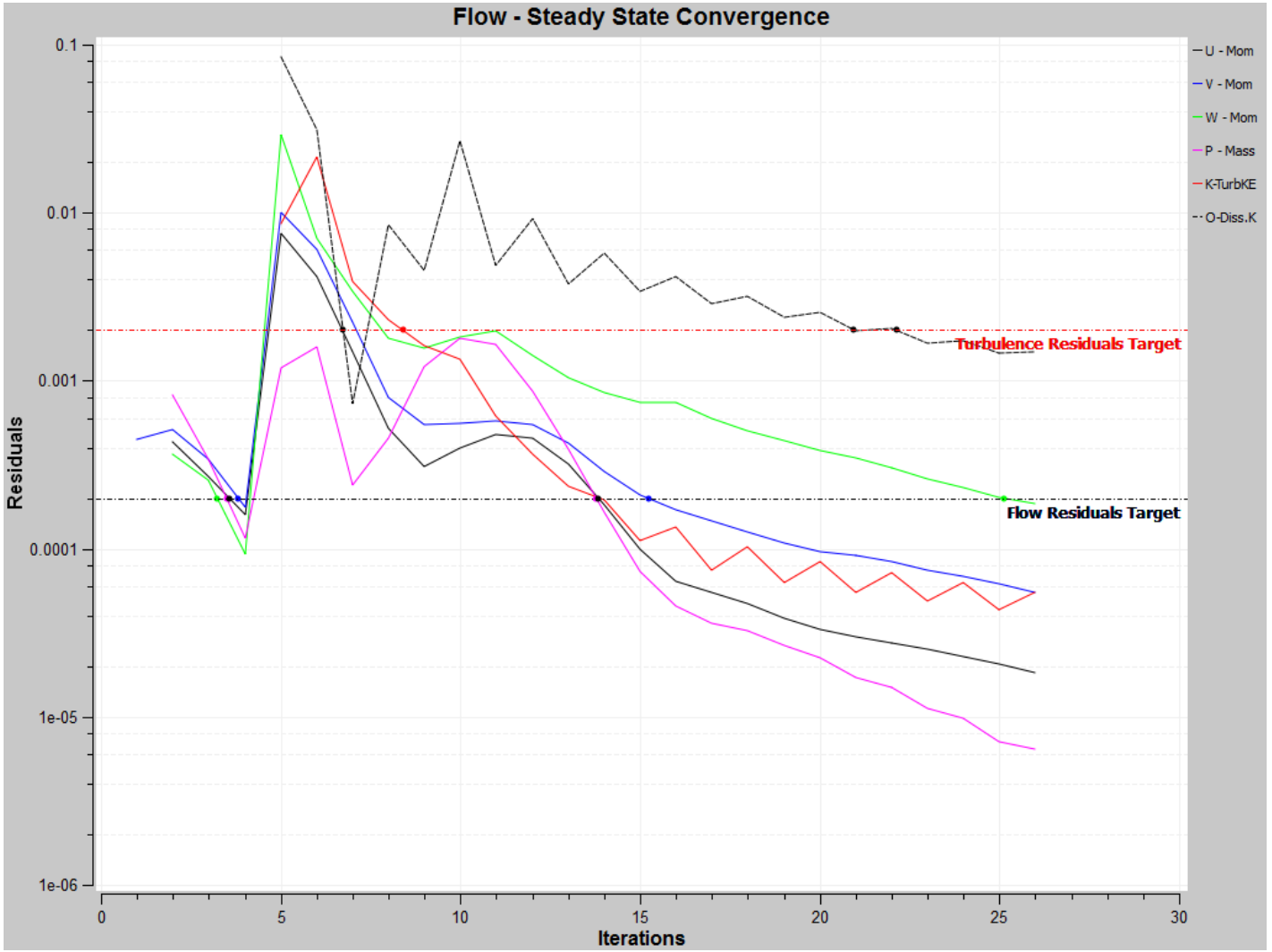

Figure 39: Steady State Convergence – Model B

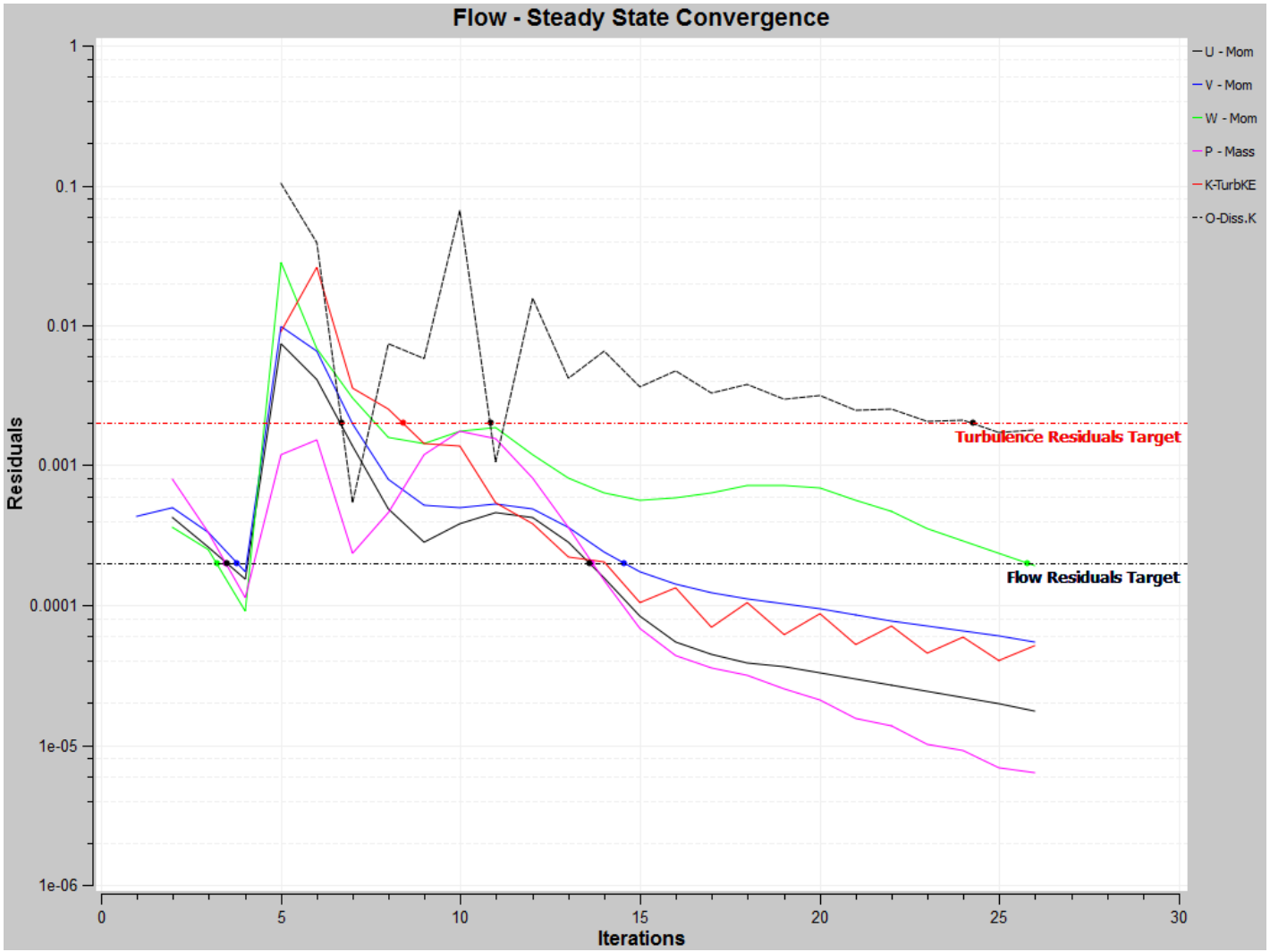

Figure 40: Steady State Convergence – Model C

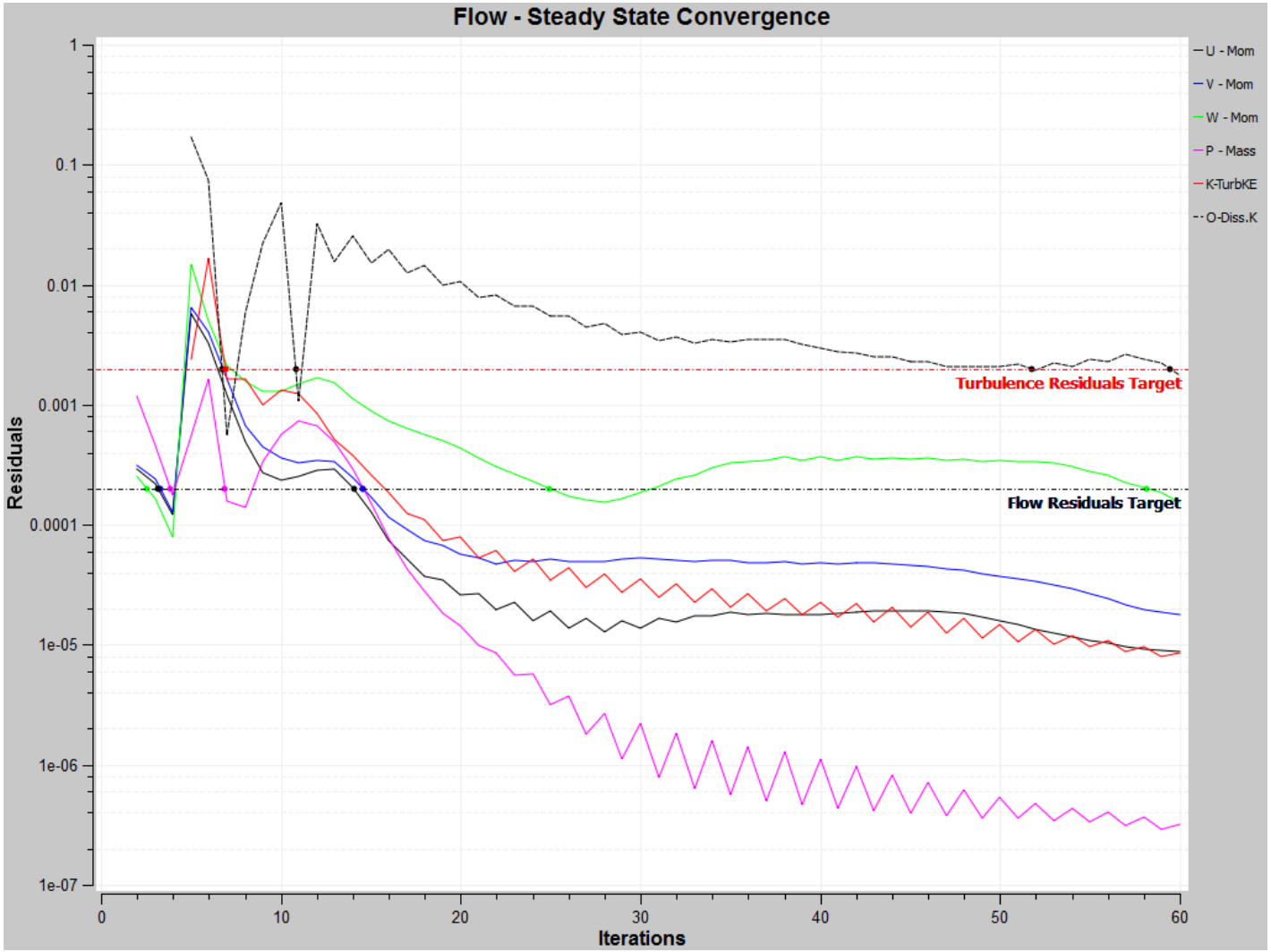

Figure 41: Steady State Convergence – Model D

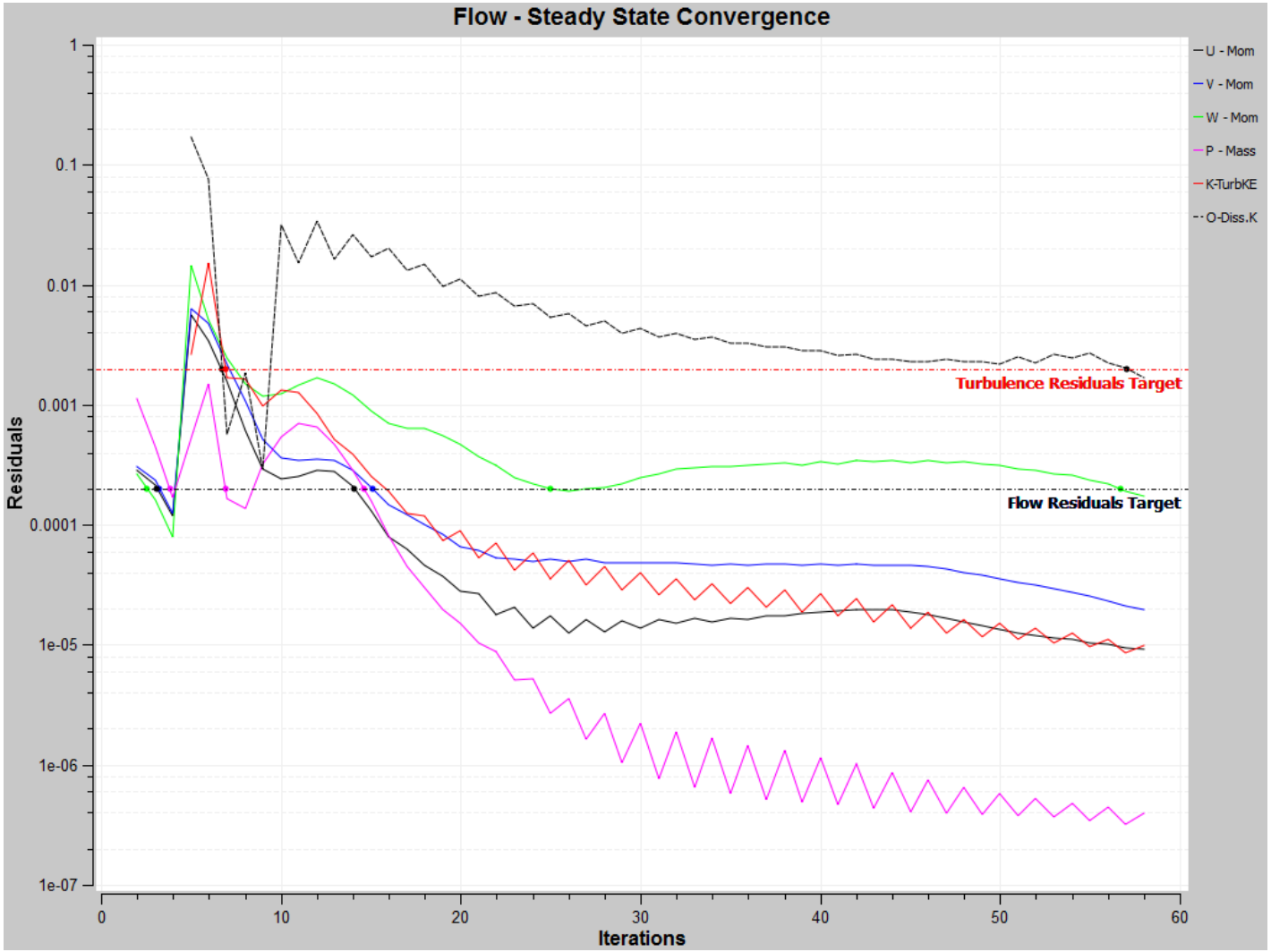

Figure 42: Steady State Convergence – Model E

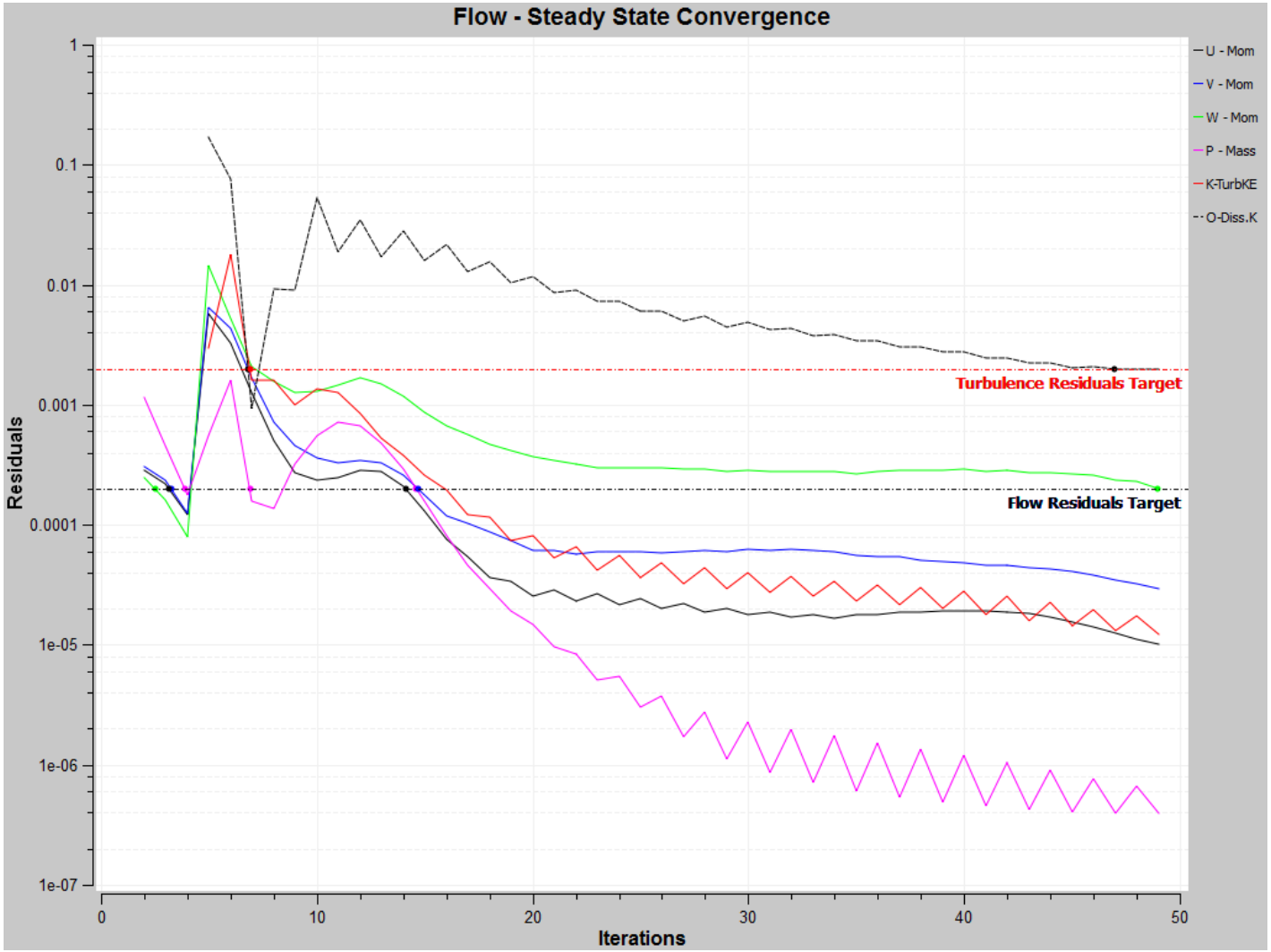

Figure 43: Steady State Convergence – Model F

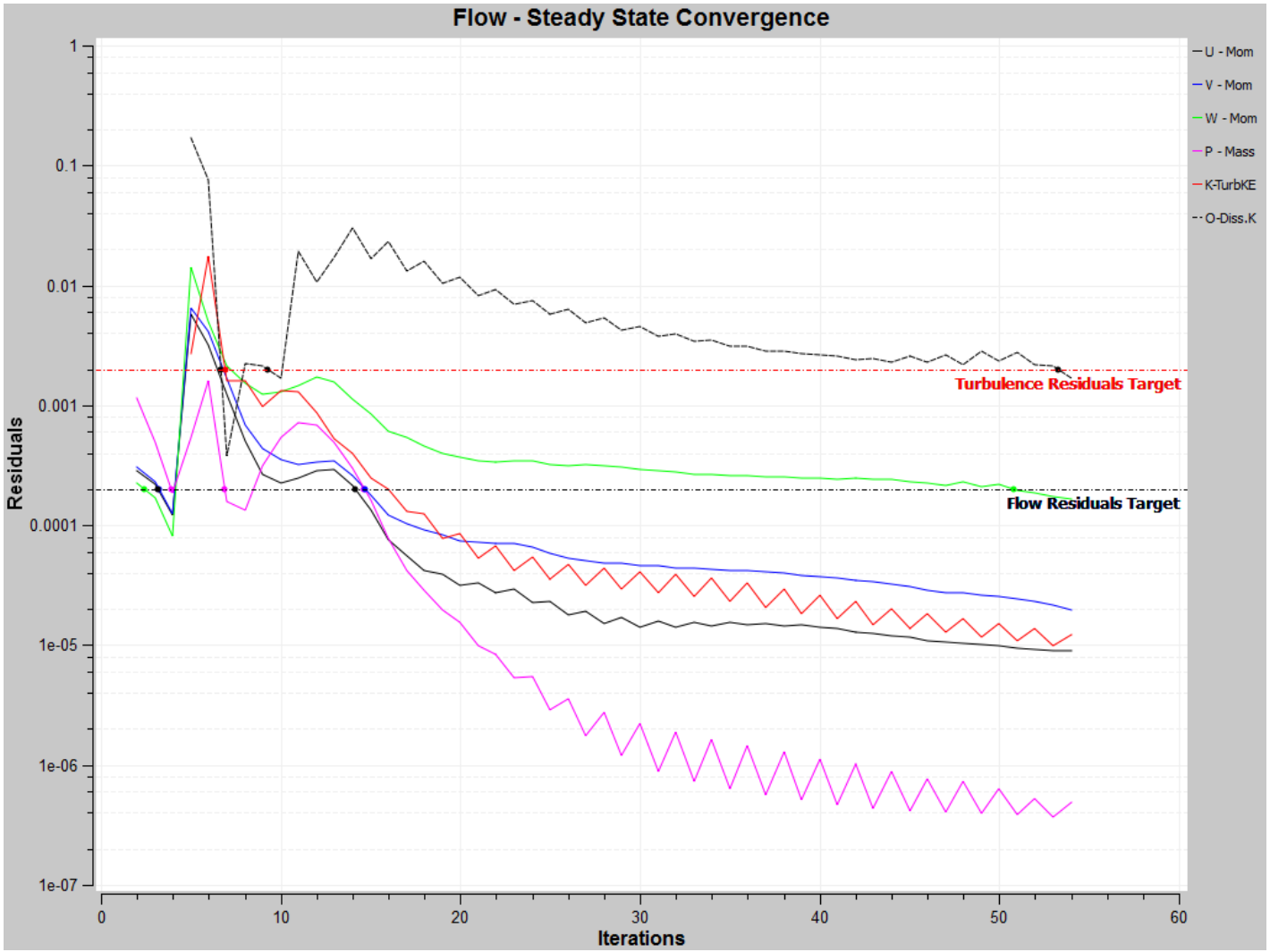

Figure 44: Steady State Convergence – Model G

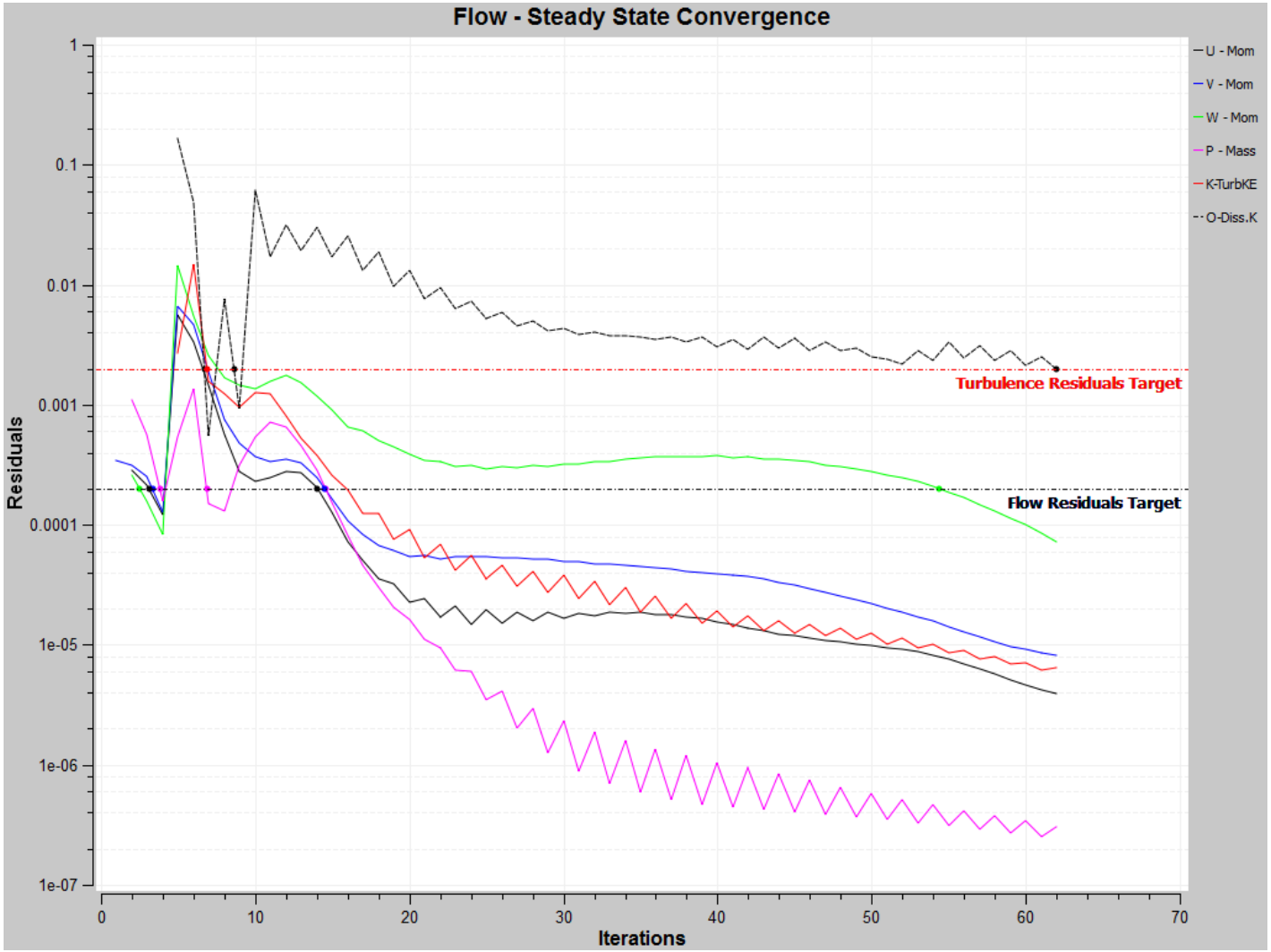

Figure 45: Steady State Convergence – Model H

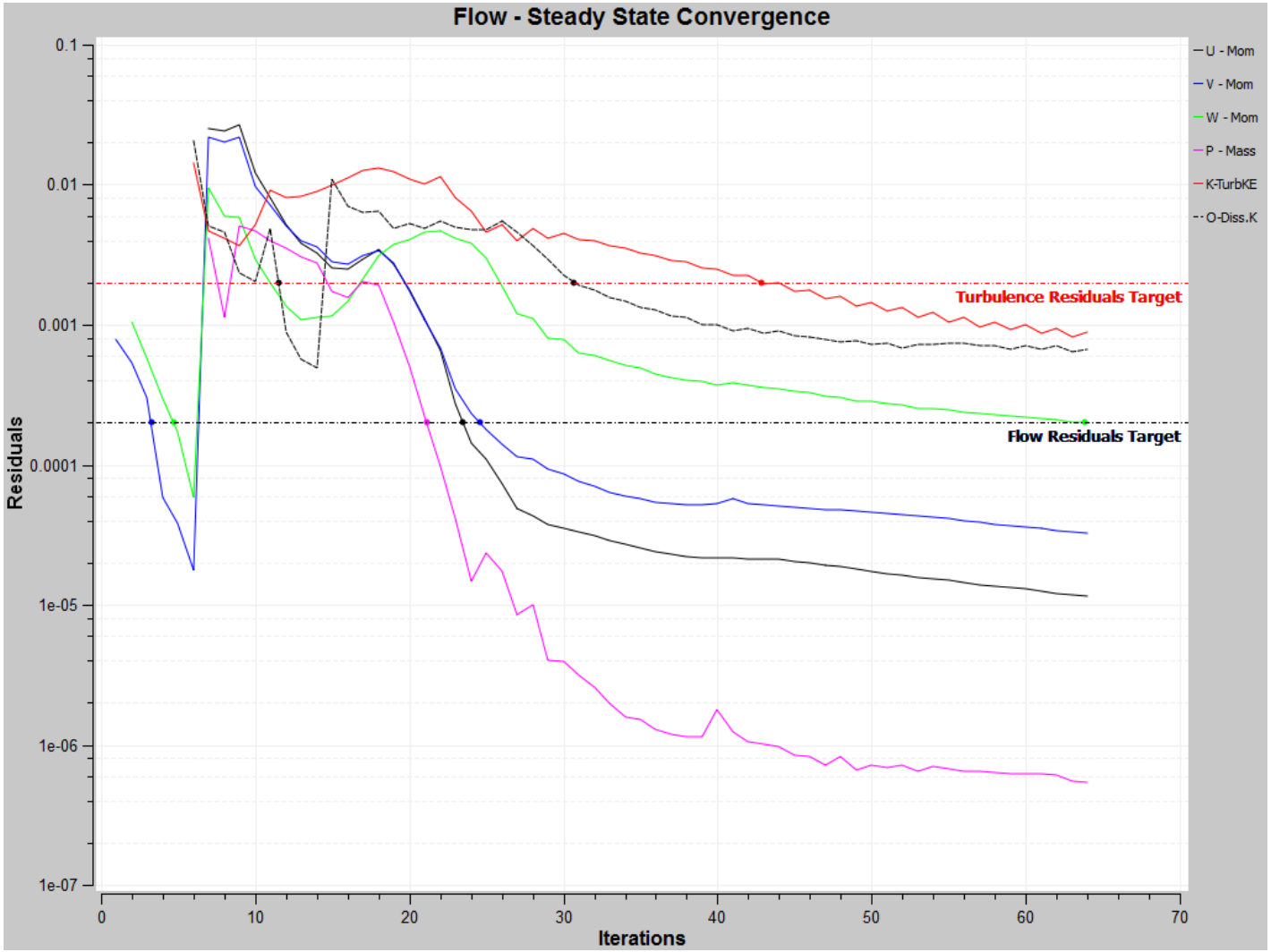

Figure 46: Steady State Convergence – Model I

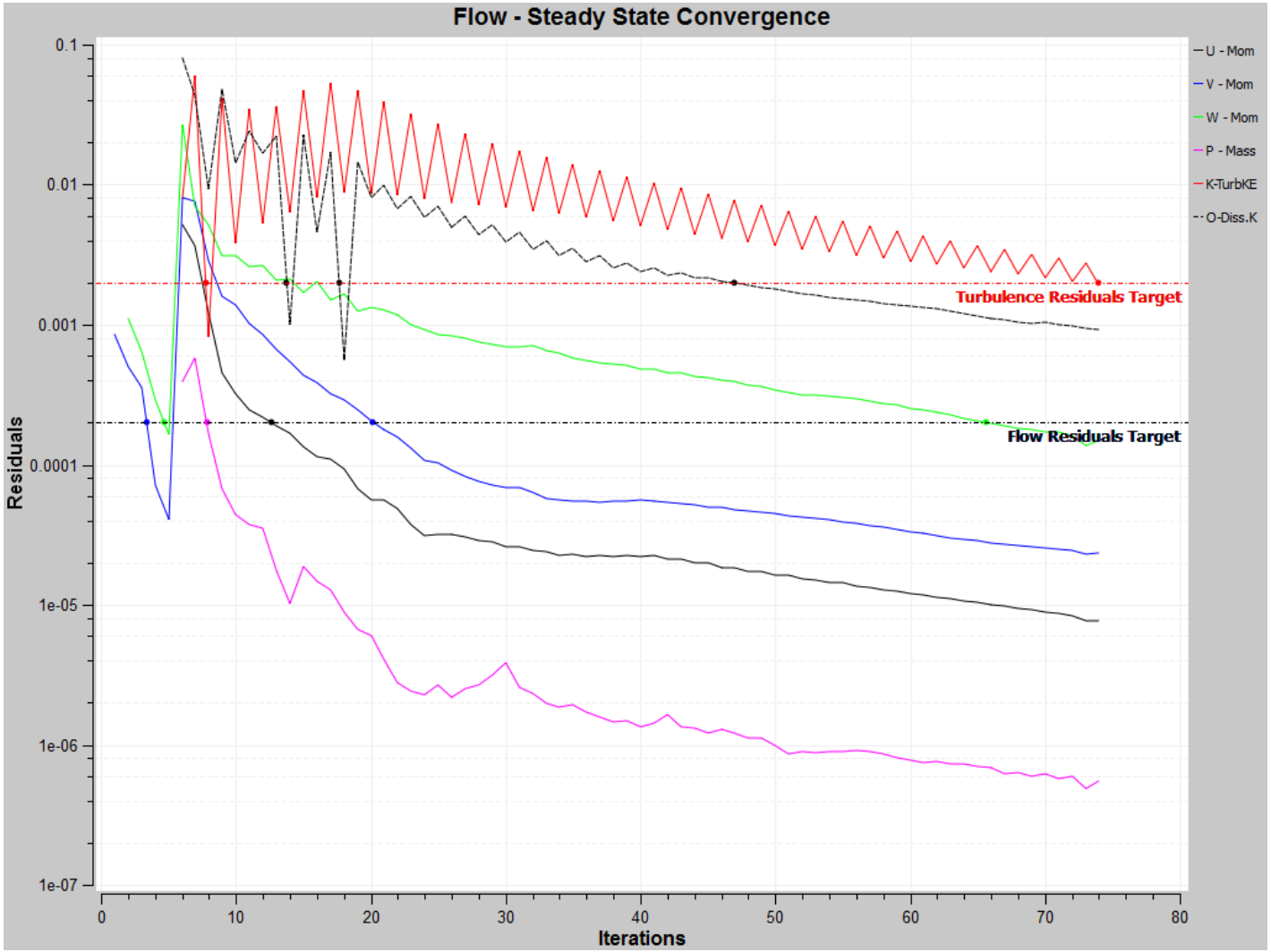

Figure 47: Steady State Convergence – Model J

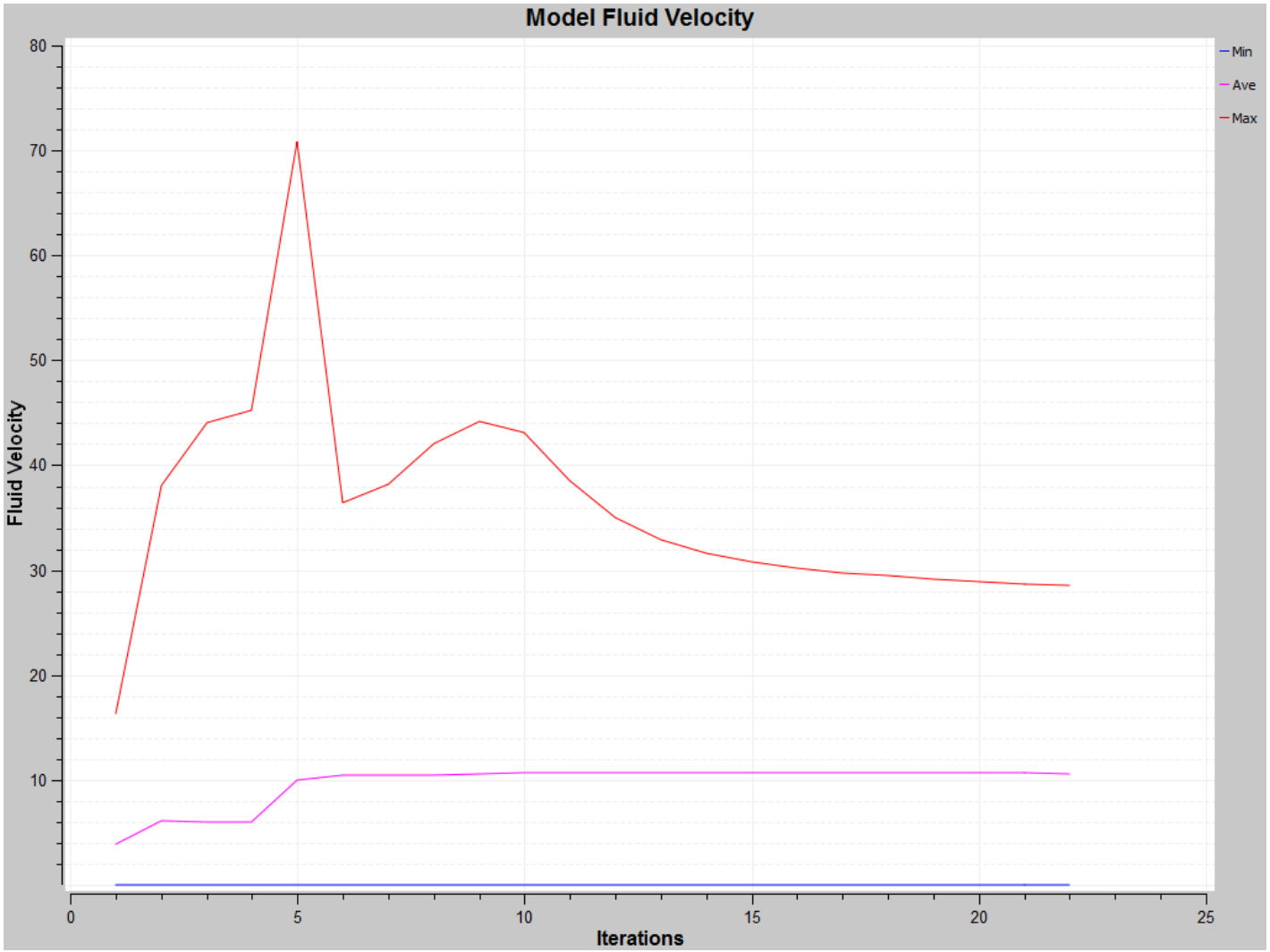

Figure 48: Steady State Solution Mesh model A

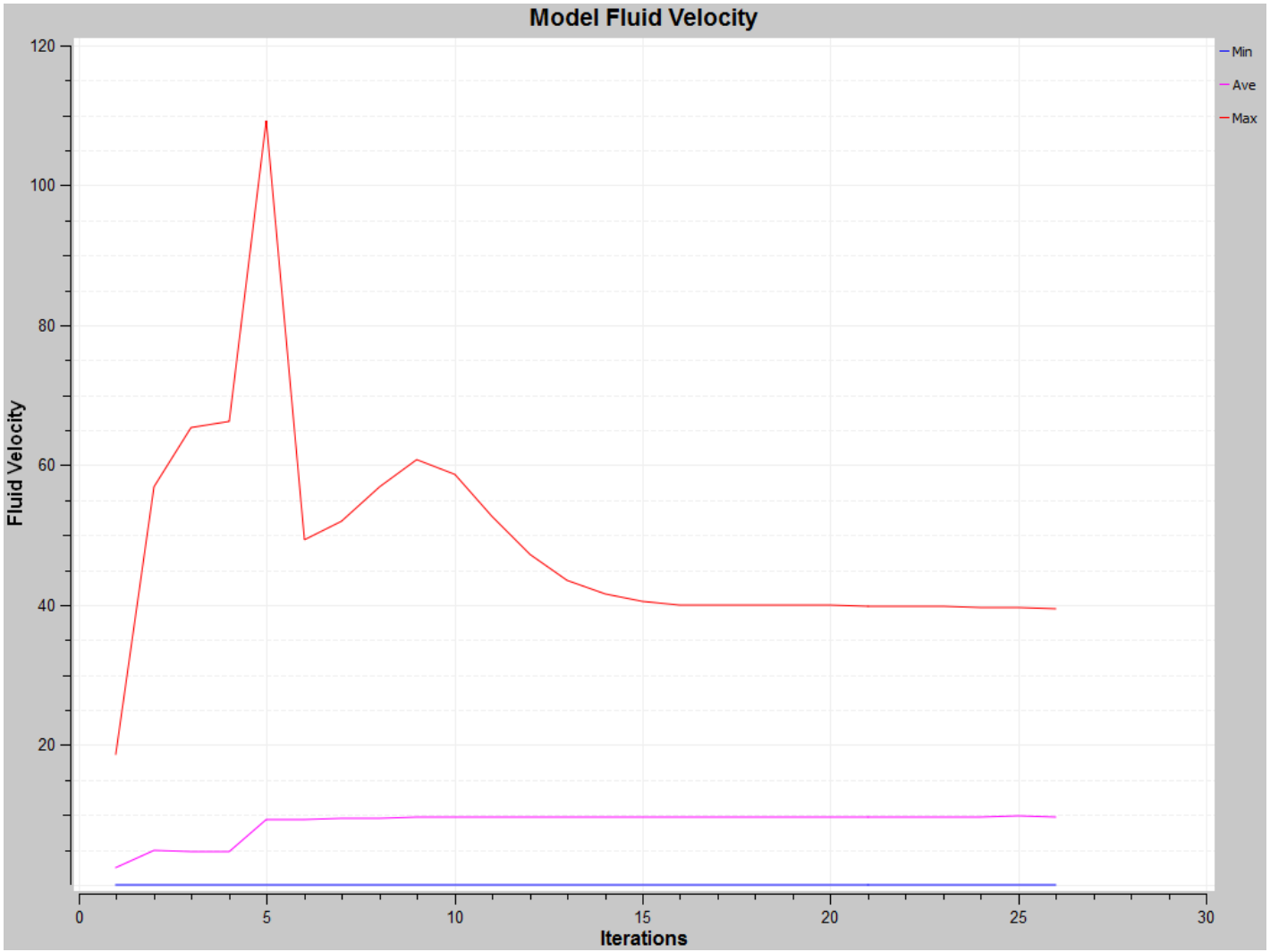

Figure 49: Steady State Solution Mesh model B

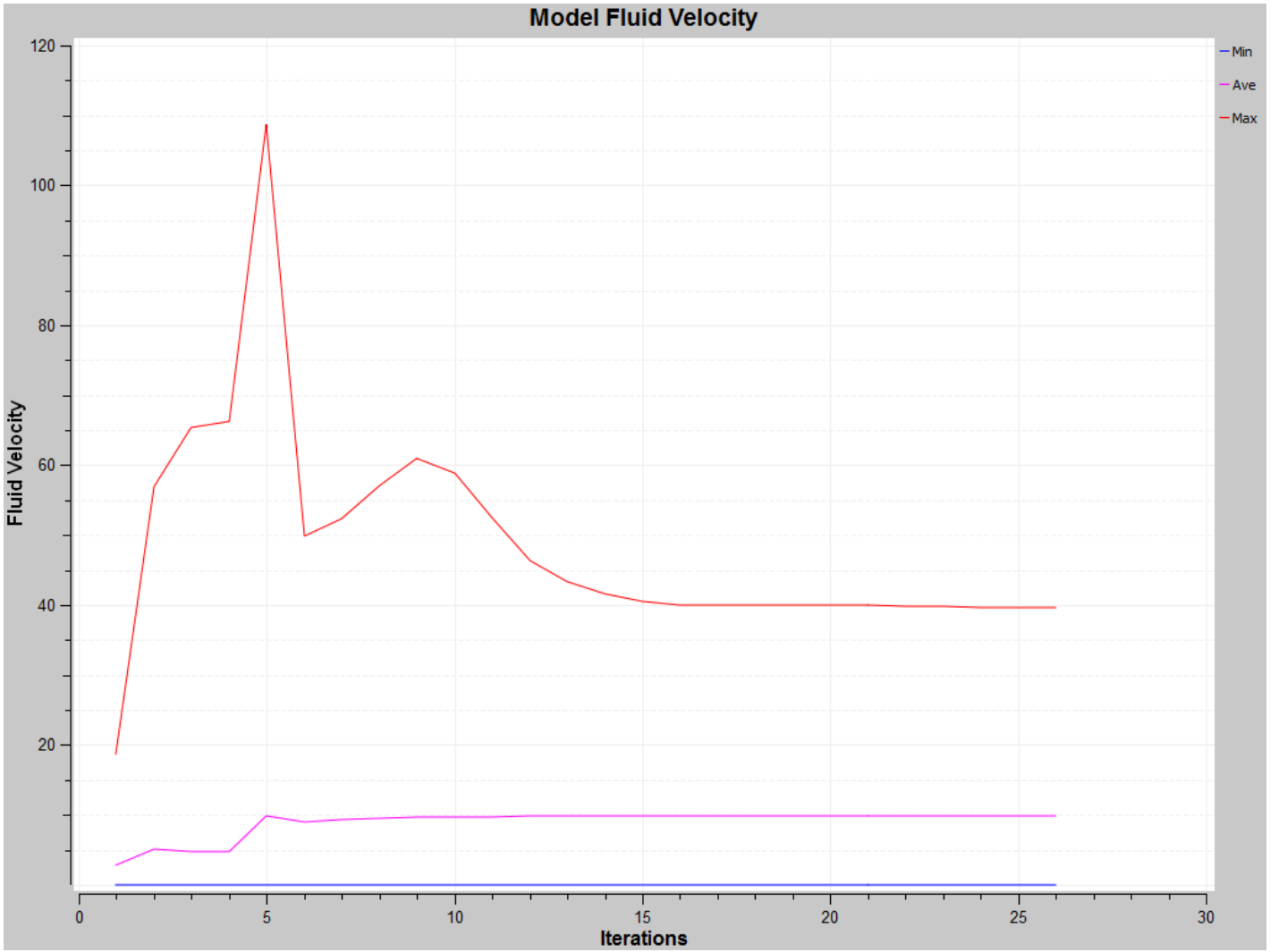

Figure 50: Steady State Solution Mesh model C

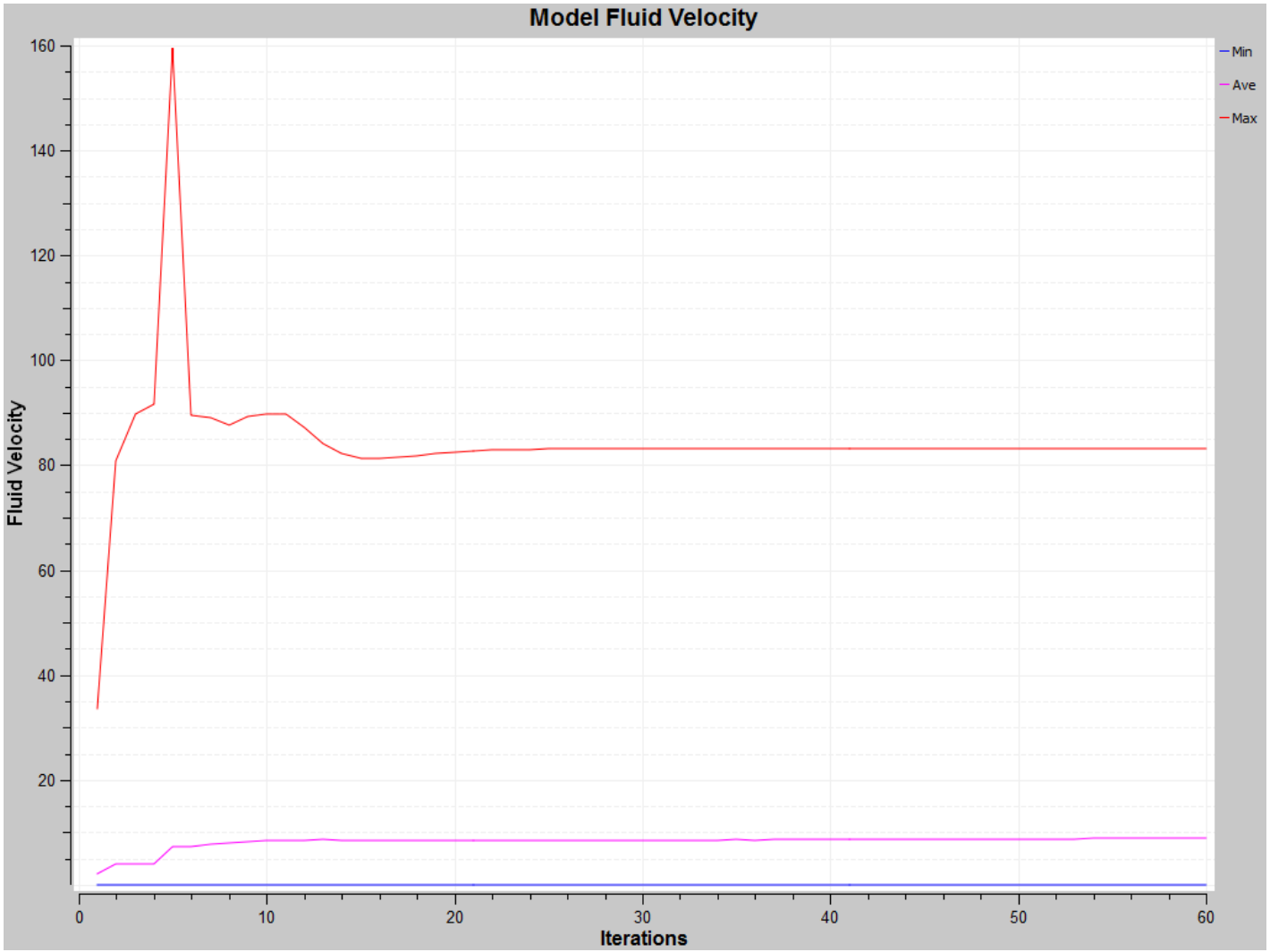

Figure 51: Steady State Solution Mesh model D

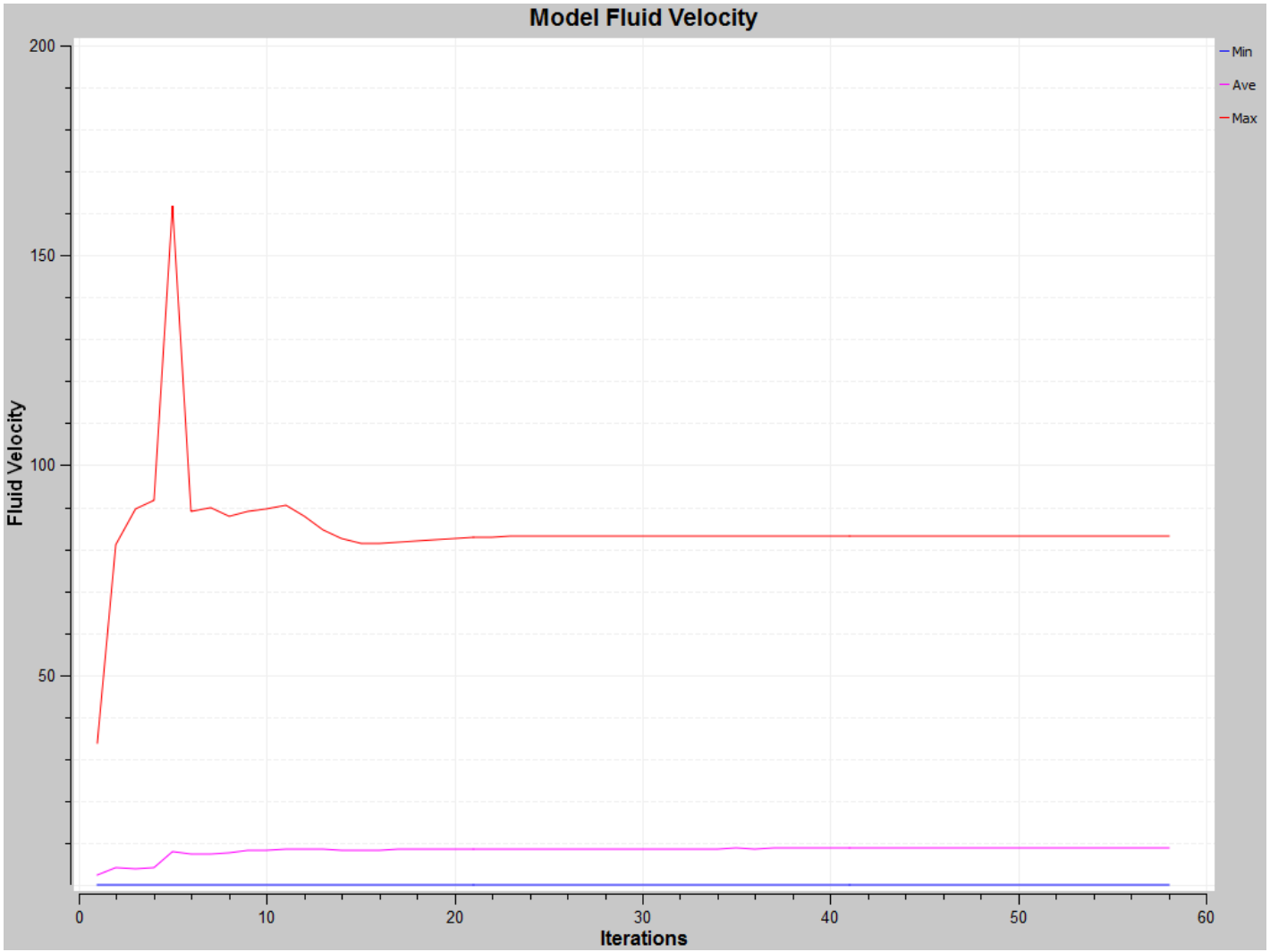

Figure 52: Steady State Solution Mesh model E

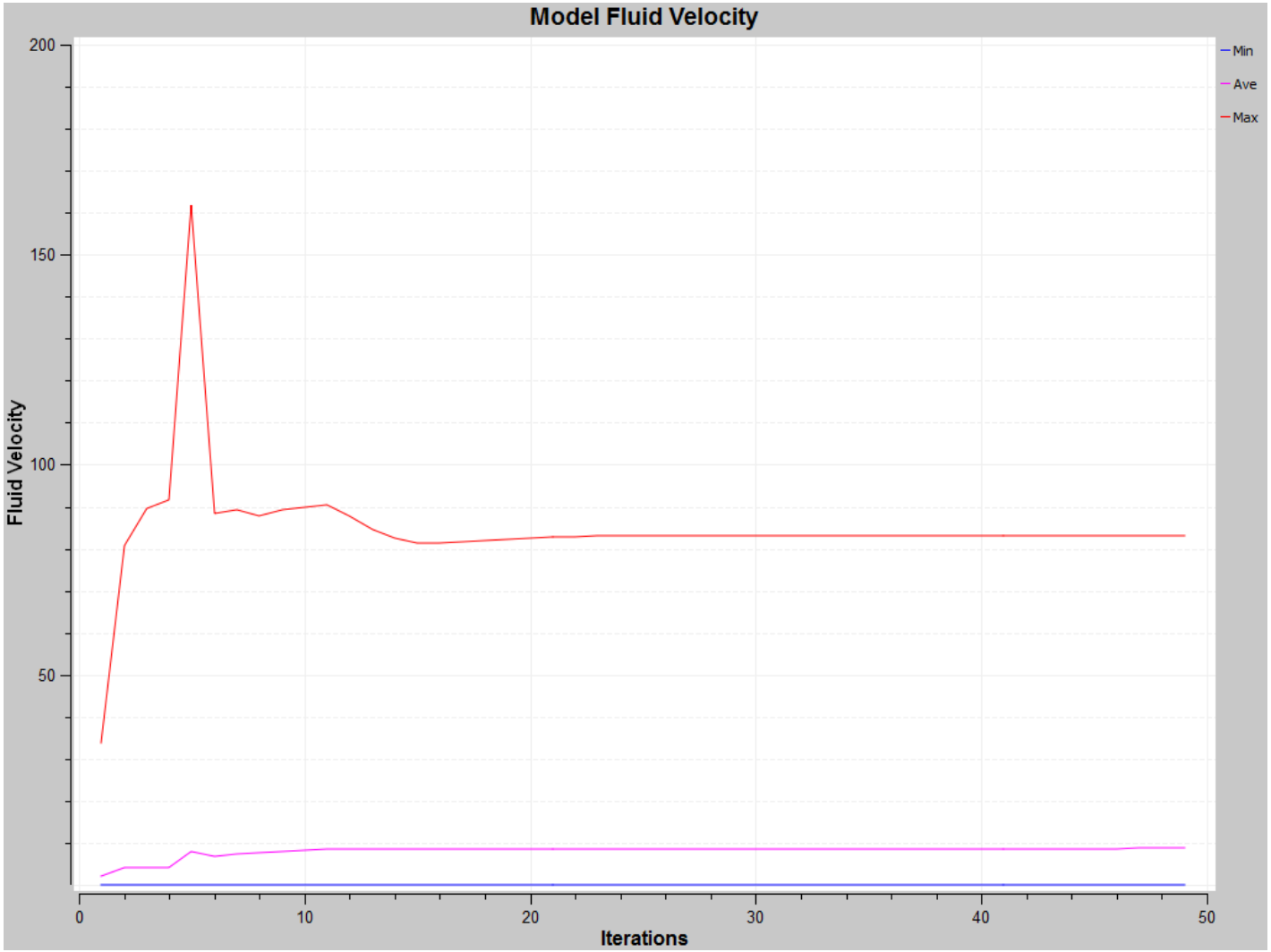

Figure 53: Steady State Solution Mesh model F

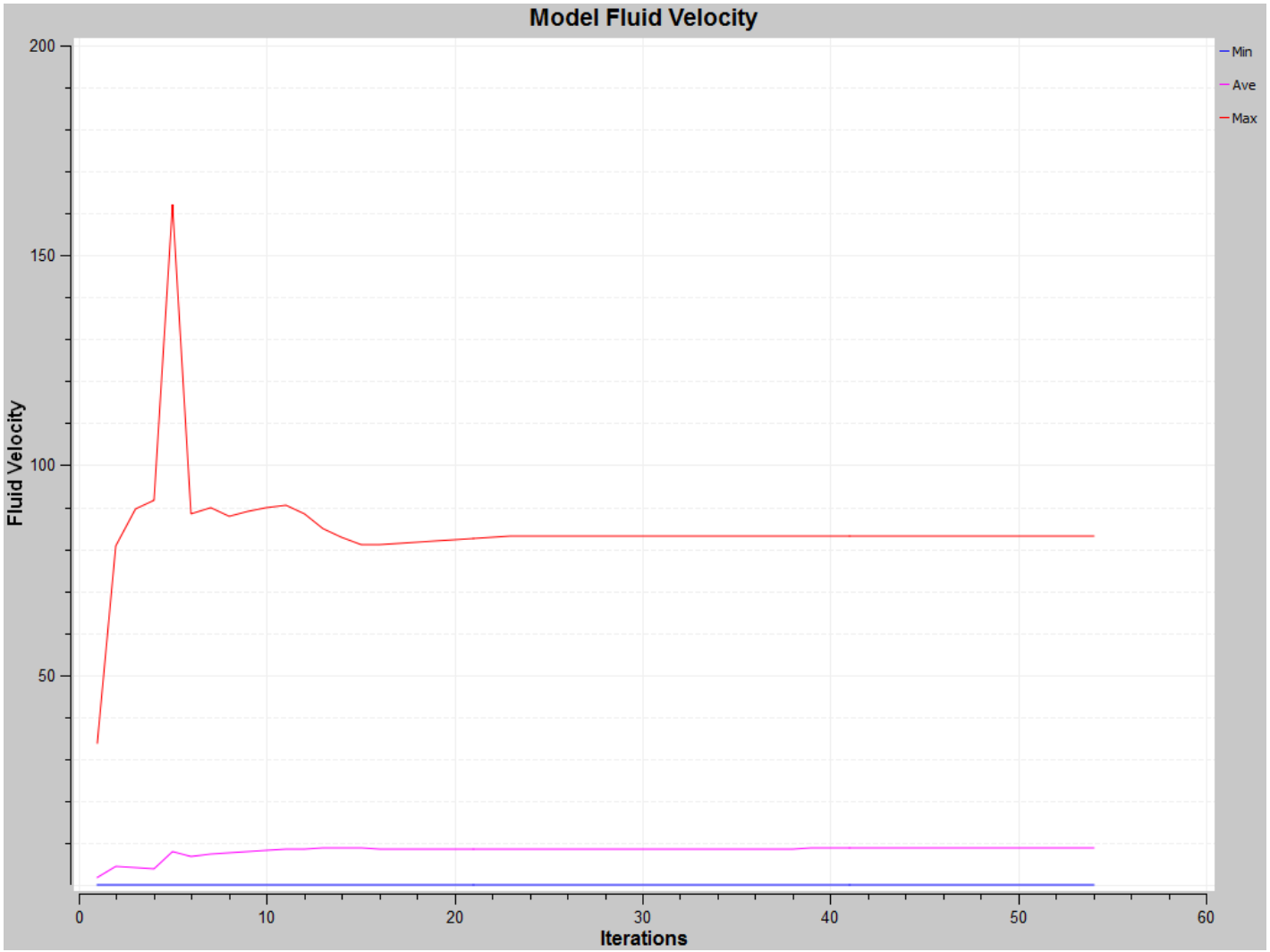

Figure 54: Steady State Solution Mesh model G

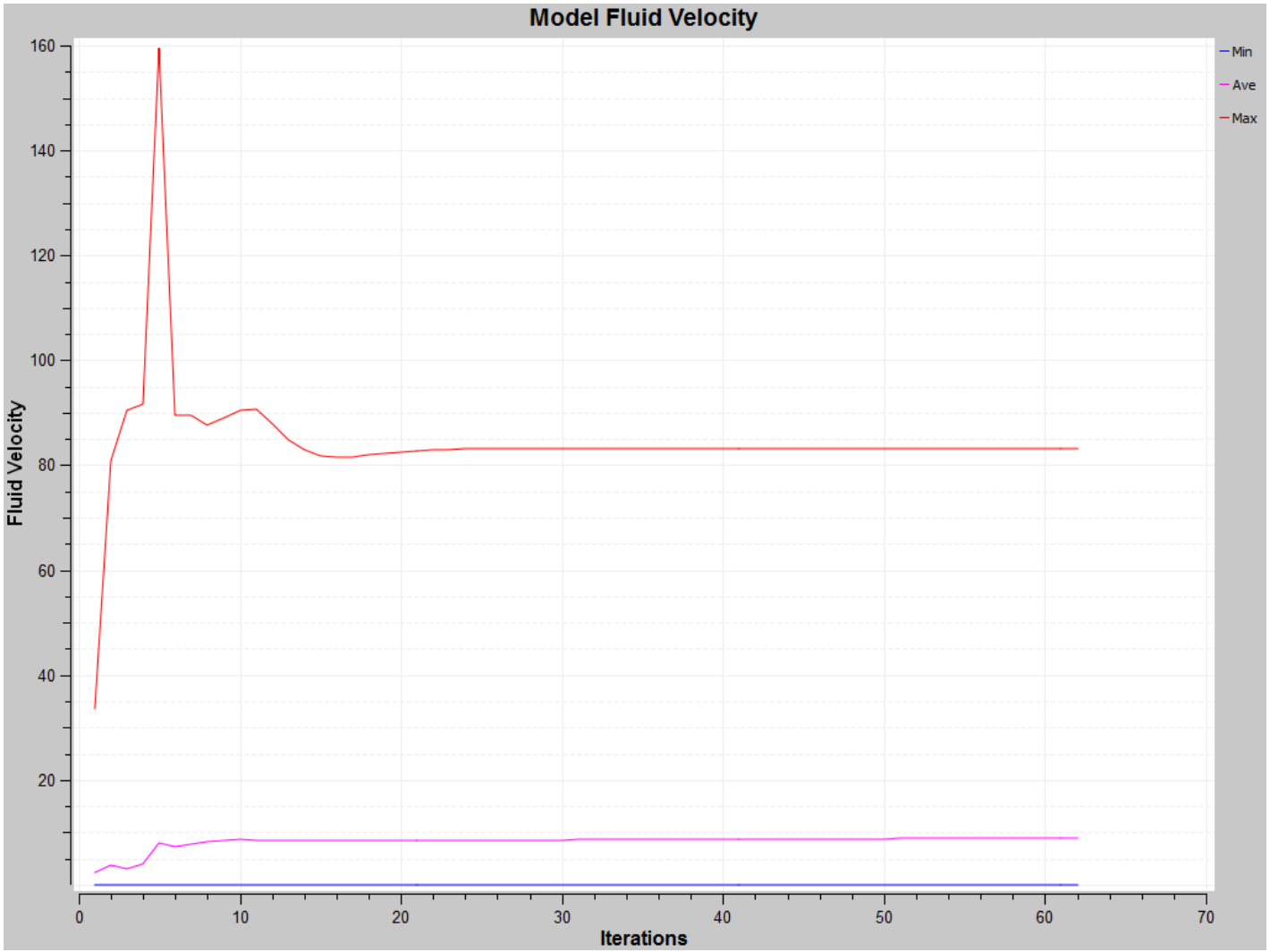

Figure 55: Steady State Solution Mesh model H

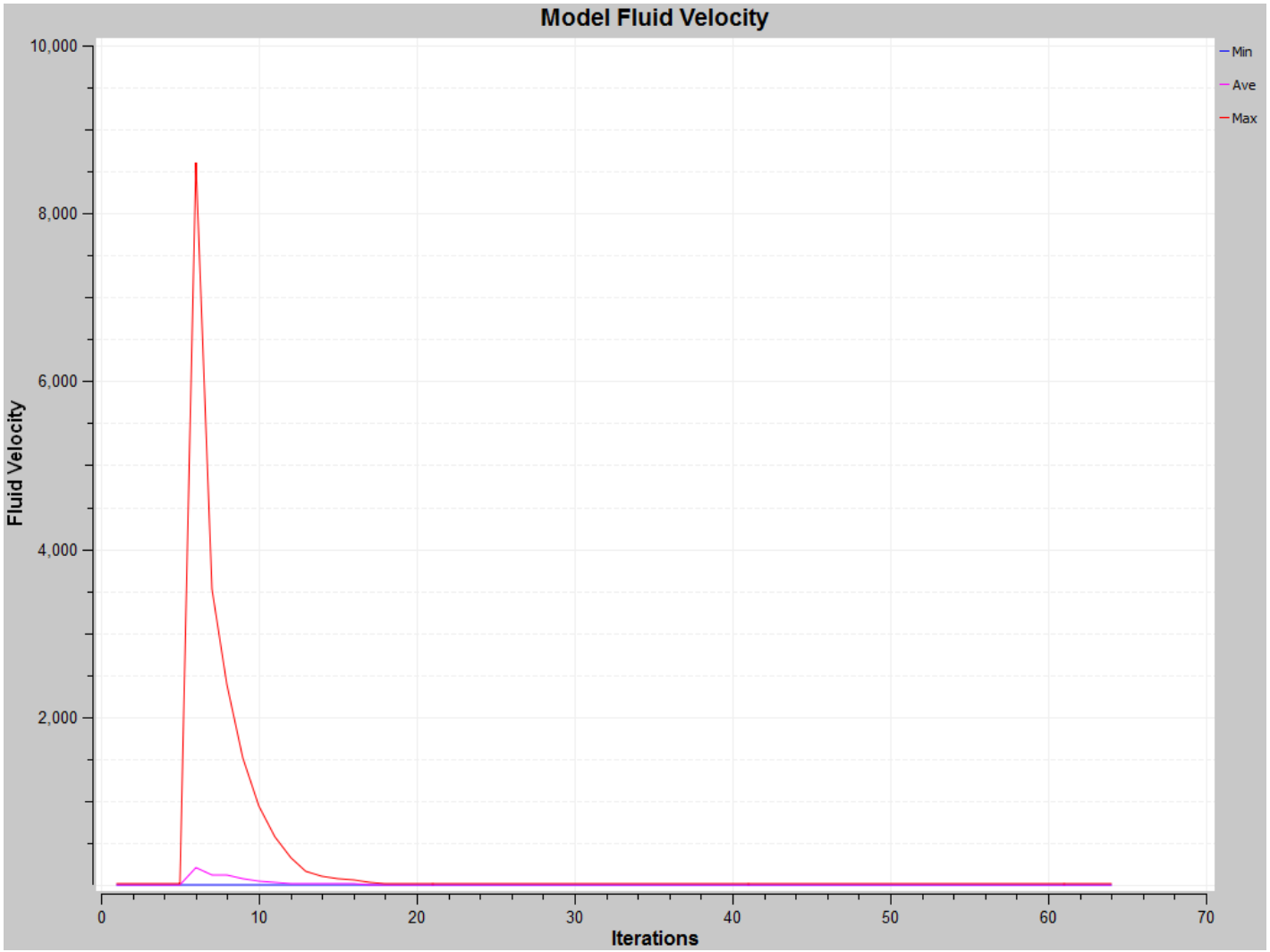

Figure 56: Steady State Solution Mesh model I

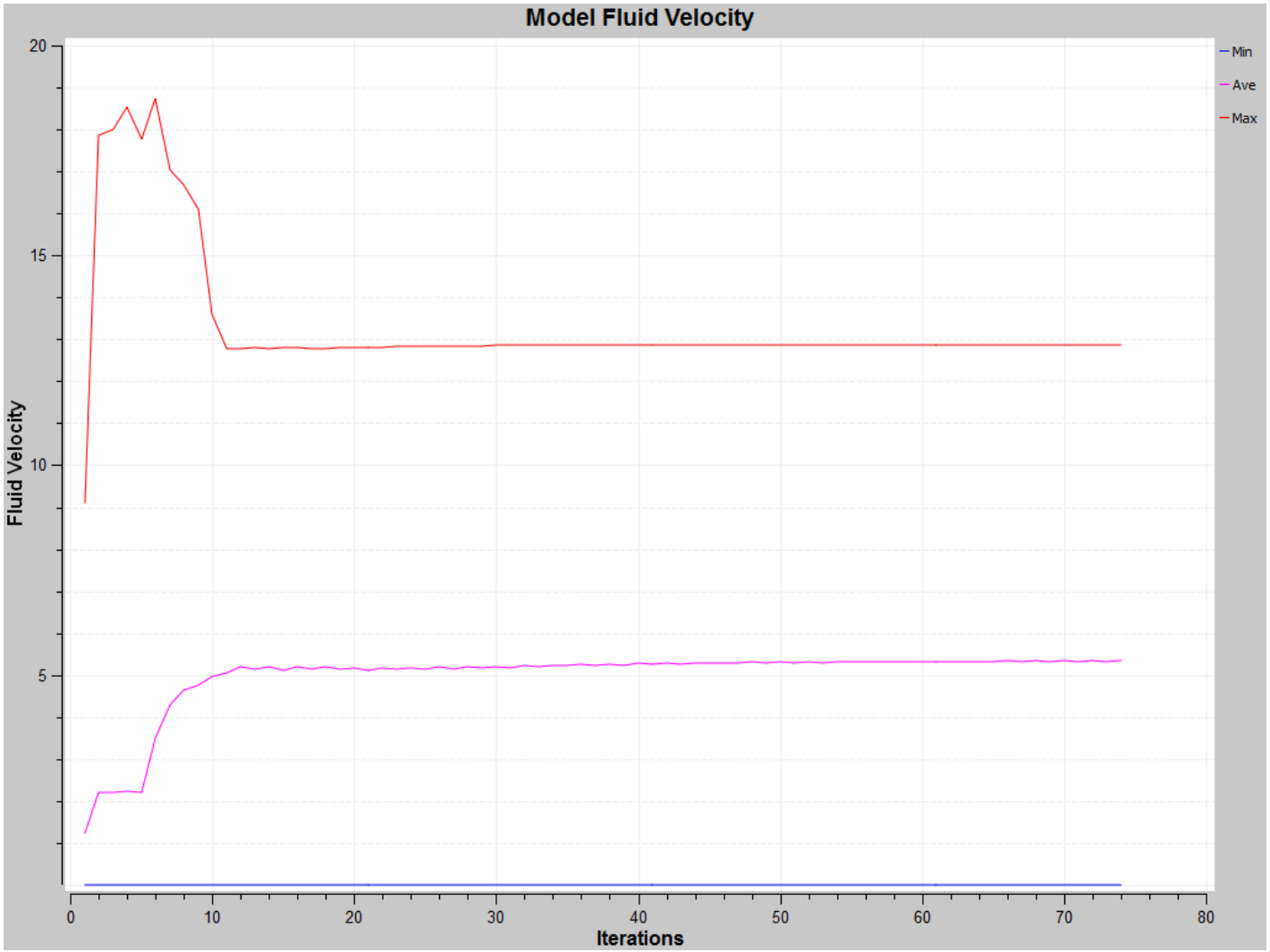

Figure 57: Steady State Solution Mesh model J